Fraunhofer ICT

Fraunhofer Institute for Chemical Technology ICT

Wissenschaftliche Schriftenreihe des Fraunhofer ICT

Thermal design optimization of traction battery modules using meta-model-based simulations

Johannes Liebertseder

Fraunhofer Verlag

Fraunhofer Institute
for Chemical Technology ICT

Johannes Liebertseder

Thermal design optimization of traction battery modules using meta-model-based simulations

Wissenschaftliche Schriftenreihe
des Fraunhofer ICT
Vol. 99

Fraunhofer Verlag

Contact:
Fraunhofer Institute
for Chemical Technology ICT
Joseph-von-Fraunhofer-Strasse 7
76327 Pfinztal (Berghausen)
Germany
Phone +49 (0)721 4640-0
www.ict.fraunhofer.de

Bibliographic information of the German National Library:
The German National Library has listed this publication in its Deutsche Nationalbibliografie; detailed bibliographic data is available on the internet at www.dnb.de.

ISSN: 0933-0062
ISBN (print edition): 978-3-8396-2025-0
DOI (free Open Access version): https://doi.org/10.24406/publica-3308

DE-90

Zugl.: Karlsruhe, KIT, Diss., 2024

Print and finishing: Fraunhofer-Druckerei, Stuttgart

The book was printed with chlorine- and acid-free paper.

Nobelstrasse 12
70569 Stuttgart
Germany
verlag@fraunhofer.de
www.verlag.fraunhofer.de

is a constituent entity of the Fraunhofer-Gesellschaft, and as such has no separate legal status.

Fraunhofer-Gesellschaft zur Förderung
der angewandten Forschung e.V.
Hansastrasse 27 c
80686 München
Germany
www.fraunhofer.de

Thermal design optimization of traction battery modules using meta-model-based simulations

Zur Erlangung des akademischen Grades eines

DOKTORS DER INGENIEURWISSENSCHAFTEN (Dr.-Ing.)

von der KIT-Fakultät für Chemieingenieurwesen und Verfahrenstechnik des

Karlsruher Instituts für Technologie (KIT)

genehmigte

DISSERTATION

von

Johannes Liebertseder, M.Sc.

aus Landau in der Pfalz

Tag der mündlichen Prüfung: 29.04.2024

Erstgutachter: Prof. Dr. Jens Tübke

Zweitgutachter: Prof. Dr. Martin Doppelbauer

Acknowledgements

This dissertation was written during my time as a research associate and group leader in the department New Drive Systems at the Fraunhofer Institute for Chemical Technology ICT. Here, I want to express my appreciation to various individuals who have supported me on this dissertation journey.

For enabling, supervising and reviewing my doctoral thesis I would like to express my sincere gratitude to Prof. Dr. Jens Tübke. I am also grateful to Prof. Dr. Martin Doppelbauer for his support and interest in my work and for taking over the co-review. Additionally, I would like to thank Dr. Hans-Peter Kollmeier for the encouragement in pursuing a doctorate at the Fraunhofer ICT.

A special thank goes to Dr. Lars Fredrik Berg for his continuous support, guidance and motivation during the course of my work. The many regular discussions and valuable inputs have contributed greatly to the success of this project.

Furthermore, I would like to thank all of my current and former colleagues at the Fraunhofer ICT who supported me and contributed directly or indirectly to this dissertation. This applies in particular to Andreas Dollinger, Fabian Kirchenbauer, Jan Bökelmann, Martin Miller, Mathias Pinnel and Thomas Sorg who have supported with the design of the battery module demonstrator and various measurements. Many thanks also go to Stefan Heß and Steffen Reuter for sharing their experiences of the same journey.

I am also thankful for the assistance of all the students, especially Adèle Ardaillou, Aurélien Royet, Christine Sonner, Trung Hieu Cao, Julian Ulrich, Lars Sollik and Susann Wunsch. Their preliminary works and investigations formed a sound basis towards my doctoral topic.

To my dear friends Martin and Markus: Thank you for being there during the ups and downs! The many consulting meetings with Markus ultimately pushed me to finish the thesis.

Finally, I would like to thank my wife and my family for their support, understanding and encouragement. Mareike, you have been my anchor throughout this challenging journey and I am lucky to have you by my side. Thank you!

Abstract

The thermal design of battery systems for electric vehicles aims to solve a conflict of objectives between a high energy density, fast charging capability and a long lifetime. The solution to this conflict is strongly influenced by the approach used for the cooling of the battery cells. Currently, the predominant cooling approach for pouch cells is bottom cooling, but tab cooling has shown potential as an alternative. It could potentially extend the battery lifetime due to small temperature differences within the cell. However, the cooling performance of tab cooling has not yet been investigated on module level and strongly depends on the geometric design of the cells. Also, the prediction of the temperature difference within a single cell with simulations is computationally expensive. Fast simulation models that predict the temperature difference depending on the geometric cell design are missing. Yet, they are needed for the evaluation, comparison and holistic optimization of battery modules with tab cooling and other cooling approaches with respect to the conflict of objectives.

Here, a tab-cooled battery module prototype using thermally conductive plastic materials is developed and analyzed. The prototype's cooling performance is evaluated on a test bench and with simulations, showing that the cooling performance is limited by the thermal resistance of the cell tabs. Furthermore, a new simulation model based on a neural network is proposed which rapidly predicts the maximum temperature difference in a single battery pouch cell after a charging process. The model considers all relevant geometric and thermal parameters and with it, a charging process of a battery module can be computed in less than 18 s. This enables the thermal optimization of pouch cell designs and the comparison of different cooling approaches on module level, which is demonstrated on two exemplary test cases. They show that even with an optimized cell design, tab cooling is not the optimal solution for cell cooling in automotive applications. With tab cooling, the lowest temperature differences within a cell are achieved, but this advantage with respect to the cell lifetime is weakened as the average temperature of the cells is significantly higher compared to bottom cooling approaches.

Overall, the novel meta-model-based simulation model is an excellent tool for the thermal design optimization of battery systems. It enables a fast and quantified solution of the conflict of objectives leading to improved electric vehicle designs.

Kurzfassung

Beim thermischen Design von Batteriesystemen für Elektrofahrzeuge muss ein Zielkonflikt zwischen hoher Energiedichte, Schnelladefähigkeit und langer Lebensdauer gelöst werden. Die Lösung dieses Zielkonflikts wird maßgeblich von der gewählten Methode zur Kühlung der Batteriezellen beeinflusst. Derzeit ist die vorherrschende Kühlmethode für Pouch-Zellen die Bodenkühlung, jedoch hat die Ableiter-Kühlung Potenzial als Alternative gezeigt. Sie könnte die Lebensdauer der Batterie aufgrund geringer Temperaturdifferenzen innerhalb der Zelle verlängern. Die Kühlleistung der Ableiter-Kühlung ist jedoch noch nicht auf Modulebene untersucht worden und zudem hängt sie stark von den geometrischen Abmessungen der Zellen ab. Des Weiteren ist die Vorhersage der Temperaturdifferenz innerhalb einer einzelnen Zelle mittels Simulationen sehr rechenintensiv. Schnelle Simulationsmodelle, die den Temperaturunterschied in Abhängigkeit vom geometrischen Design der Zelle vorhersagen, fehlen bisher. Sie werden jedoch für die Bewertung, den Vergleich und die ganzheitliche Optimierung von Batteriemodulen mit Ableiter-Kühlung und anderen Kühlansätzen benötigt.
In dieser Arbeit wird ein Prototyp eines Ableiter-gekühlten Batteriemoduls mit thermisch leitfähigen Kunststoffmaterialien entwickelt und analysiert. Die Kühlleistung des Prototyps wird am Prüfstand und mittels Simulationen untersucht. Es zeigt sich, dass die Kühlleistung durch den thermischen Widerstand der Zell-Ableiter begrenzt wird. Darüber hinaus wird ein neues Simulationsmodell auf Basis eines neuronalen Netzes entwickelt, das die maximale Temperaturdifferenz in einer Pouch-Zelle nach einem Ladevorgang schnell vorhersagt. Das Modell berücksichtigt alle relevanten geometrischen und thermischen Parameter und ermöglicht die Berechnung eines Ladevorgangs eines Batteriemoduls in weniger als 18 s. Dadurch wird die thermische Optimierung von Pouch-Zell-Designs und der Vergleich verschiedener Kühlansätze auf Modulniveau ermöglicht, was anhand von zwei exemplarischen Testfällen demonstriert wird. Diese zeigen, dass auch bei optimiertem Zelldesign die Ableiter-Kühlung nicht die optimale Lösung für die Zellkühlung in Automobilanwendungen ist. Mit der Ableiter-Kühlung werden zwar die geringsten Temperaturdifferenzen innerhalb einer Zelle erreicht, dieser Vorteil wird jedoch hinsichtlich der Zelllebensdauer durch die höhere Durchschnittstemperatur der Zellen im Vergleich zu Ansätzen mit Bodenkühlung geschwächt. Insgesamt ist das neuartige, metamodelbasierte Simulationsmodell ein hervorragendes Werkzeug für die thermische Designoptimierung von Batteriesystemen. Es ermöglicht eine schnelle und quantifizierte Lösung des Zielkonflikts, was zu verbesserten Designs von Elektrofahrzeugen führt.

Contents

1 Introduction

1.1 Motivation

Battery electric vehicles (BEVs) become more and more accepted in transportation and their market presence will continue to expand in the coming years [1]. This trend applies for all vehicle types ranging from small vehicles such as e-bikes to passenger cars and large electric trucks. Yet, challenges remain on the path towards electrification: Range anxiety and long charging times are still an obstacle for some users and prevents them from using electric vehicles [2]. Both of these aspects are mainly determined by the technical limitations of the vehicle's battery system. Thus, vehicle manufacturers focus their developments on higher energy densities and the fast charging capability of the battery in order to increase the user acceptance and gain market advantages [3].

In battery systems, lithium-ion based battery cell chemistries will stay dominant in the near future [3, 4]. Consequently, the thermal management of the cells plays a crucial role in the development and improvement of BEVs as these cell chemistries require an accurate control of the cell temperature [5]. However, designing a thermal management system (TMS) that satisfies the aforementioned user requirements leads to a conflict of interest: High charge rates require a powerful cooling system to dissipate the generated heat during the charging process. At the same time, they lead to an increased mass and thus, reduce the energy density of the system. Furthermore, charging batteries with high charge rates decreases the lifetime of the cells. Consequently, the design of the battery thermal management system is a challenging task where the conflict of objectives between fast charging capability, energy density and a long lifetime needs to be solved.

In thermal management systems of state of the art BEVs there are two predominant approaches to cool the battery cells: either by directly cooling the cell surface or by integrating the cells into a battery module that is cooled from below [6]. Recently in literature, tab cooling has emerged as an alternative, where the cells are directly cooled on their electrical tabs [7–10]. Hunt et al. [9] have shown that using tab cooling can increase the lifetime of a lithium-ion pouch cell three times compared to surface cooling due to the more homogeneous temperature distribution within the cell. However, it is not recommended to use standard pouch cells for a tab cooling: Zhao et al. [7] found out that it is more effective if the geometry of the tabs and the battery cell is specifically adjusted to the tab cooling system. Nonetheless, the potential of a TMS with tab cooling is fairly unknown. Until now, the majority of the tab

cooling studies focus their research on cell level and do neither provide an implementation for tab cooling on module level nor apply holistic optimization to adjust the cell geometry to the cooling approach or compare its performance on module level to other cooling methods.

Closing this knowledge gap with experimental investigations is not feasible, as many different battery cells with varying geometries but an identical cell chemistry would be needed. Cell manufacturers do not offer such a great variety of cell geometries. Hence, simulation models must be used instead.

Performing the needed investigations and holistic optimization of battery thermal management systems via simulation is associated with major challenges as well. To analyze the spatial temperature distribution within a cell and thus, analyze the potentially biggest advantage of tab cooling approaches, 3D simulation models are needed. However, the computation times of 3D models on module or system level are high and in the range of several hours for the simulation of one charge or discharge cycle [11–14]. Consequently, making multiple simulations with different, varying parameters to optimize the cell design for a tab cooling or other cooling methods would be an extremely time consuming process. On the contrary, 1D simulation models, that are significantly faster and usually used to model the battery thermal management on system level, are not capable to model temperature differences within a cell. First approaches that try to overcome that shortcoming of 1D system models and integrate a prediction of the temperature difference within a cell have been proposed [15–17], but do not provide the flexibility to quickly change the dimensions of the battery cell. In a review article, Tomaszewska et al. [18] explicitly pointed out that there is a lack of such fast and flexible simulation models and state that this is a field of research which should be covered so that the cell geometry can be holistically optimized for the cooling system. Thereby, the conflict of objectives between fast charging capability, energy density and a long lifetime could be solved and different cooling approaches could be comprehensively evaluated.

1.2 Objective

This dissertation aims to close the knowledge gap regarding tab cooling on module level and missing, efficient simulation models for the comparison, evaluation and optimization of different cooling approaches.

As current studies on tab cooling mainly focus on cell level, an engineering solution for a tab cooling on module level will be developed in this thesis. The main challenge is the realization of the thermal connection between the tabs and the cooling system, as an electrically insulating but thermally conductive material is needed in-between the components. Thermally conductive plastics are the most promising candidate to solve that problem as they are electrically insulating and offer a high design freedom for the structural implementation. However, their thermal conductivity is still inferior compared to metals. Thus, research question 1 aims to analyze and quantify their influence on the thermal performance to evaluate the potential of their usage in tab cooling approaches.

Research question 1: *Is it possible to realize tab cooling with thermally conductive plastics in a module and how is its performance influenced by the thermal conductivity of the plastic material?*

Having analyzed the feasibility of tab cooling on module level, the question regarding the optimal thermal design of a battery cell as well as the overall evaluation of the cooling performance remains. To answer this question, tab cooling is compared to bottom cooling, which is currently the dominating, state of the art cooling approach in BEVs. Thereby, the conflict of objectives between fast charging, energy density and a long lifetime must be considered so that a clear and quantified conclusion about the thermal cell design and the ideal cooling approach is possible. Hence, the goal of research question 2 is the derivation of a clear answer to that problem.

Research question 2: *For given boundary conditions and optimization objectives, what is the optimal thermal design of a pouch cell with tab or bottom cooling and which cooling method should be preferred?*

Both of the research questions may only be answered with efficient simulation models beyond the state of research. They must provide a fast (<1 min) prediction of the temperature differences within a single battery cell of a battery module while still being able to vary all relevant parameters for the thermal design. Thus, besides answering the proposed research question, the objective of this thesis is the development of such a new model.
It focuses on pouch battery cells and evaluates the performance of the cooling method during a charging process, as this is the most demanding load case from a thermal point of view [19, 20]. Also, only battery lifetime aspects are considered that are influenced by temperature-related phenomena. Other aspects that have an influence on the battery lifetime – like mechanical stresses within the cells – are neglected.

1.3 Outline

In chapter 2, the necessary fundamentals for the understanding of the thesis are described. At first, the state of research in the design of vehicle battery systems and their thermal management – including tab cooling – is presented. Afterwards, the design and simulation of battery cells and systems is discussed, and relevant preliminary works that deal with efficient system simulation models and the prediction of temperature differences within cells are analyzed. Finally, some modeling and mathematical fundamentals are given to facilitate the understanding of the developed simulation model. In particular, this includes the basics about meta-models using artificial neural networks, as they will be applied during the modeling process.
In chapter 3 the novel battery module simulation model is developed. Starting with a description of the overall modeling approach, a simulation model for the used reference battery cell is created using state of the art simulation models. Following that, two related module simulation models are derived to answer the two research questions. At first, a novel

tab-cooled battery module prototype is presented. It is investigated with experiments as well as a simulation model that is validated with the experimental data. Secondly, a novel, generic battery module model is developed that uses an artificial neural network to rapidly predict the temperature differences within a cell after a charging process. It is integrated in an optimization procedure to answer the second research question and solve the conflict of objectives.
Chapter 4 contains the results of the developed simulation models and experiments. They are analyzed and discussed in detail and the answers to the proposed research questions are given. Furthermore, the computing performance of the developed simulation approach is evaluated.
The thesis finally concludes in chapter 5 with a summary of the work including the novel developments and findings as well as an outlook on future research topics and remaining open questions.

2 Fundamentals

2.1 Electric vehicle battery systems and cells

In battery electric vehicles, the battery system has a strong influence on the vehicle design. It is one of the most expensive components in the vehicle [21, 22], contributes heavily to the mass of the vehicle and consumes a significant amount of design space [22, 23]. Also, the requirements from a user and manufacturer perspective are high, which drives the current research and development trends towards increased safety, reduced costs, higher energy density, fast charging capability and longer lifetime [22]. The present thesis focuses on the latter three aspects.

2.1.1 Packaging and energy density

For automobiles in general, there are three common approaches for the integration of the battery system – also called battery pack – in the vehicle, which are shown in figure 2.1. Most of the current electric automobiles use the floor architecture, as it leads to a low center of gravity, an even axle load distribution and leaves sufficient design space and flexibility for the other components and the passenger cabin of the car. Other electric vehicles like trucks or buses may integrate the pack differently, however, in most of the cases the pack is the shape of a rectangular cuboid [24, 25].
The general structure of a battery pack is depicted in figure 2.2. A subset of the battery cells usually forms a module, that electrically and mechanically combines a certain number, but not all of the cells. These modules are then integrated into the pack, together with all other

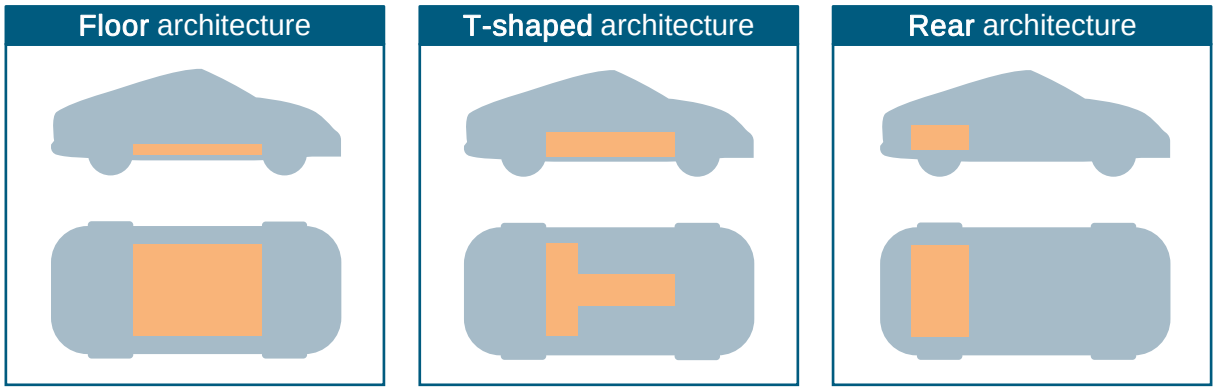

Fig. 2.1: Packaging architectures of battery packs in automobiles (based on [26] and [27])

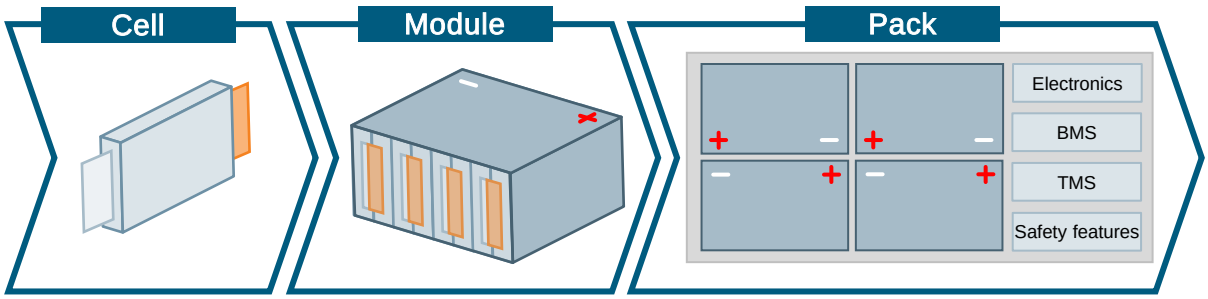

Fig. 2.2: General setup and main components of a battery system (based on [22])

components for the connection and control of the pack: The electronic components for the connection of the single modules and the pack to the rest of the vehicle, the battery management system (BMS), the thermal management system (TMS) and safety features like venting valves or additional structural parts that increase the stability of the pack. Especially the thermal management system and the structural parts of the module and the pack have a strong influence on the energy density of the system as they contribute to the mass and take up space. To increase the energy density, so-called cell-to-pack approaches are a current research topic, where the intermediate structural layer of the module is dropped and the cells are directly combined into a pack [28, 29].

Another factor that strongly influences the energy density of the pack is the energy density of the cells. Currently, in most of the automotive battery systems Li-ion batteries with lithium-nickel-manganese-cobalt-oxide (NMC) as cathode material and graphite as anode material are used [30–32]. This cell chemistry provides a higher energy density compared to other commercially available materials [28].

The cell format also has a significant impact on the pack design and the energy density of the battery system. Depending on the cell format, the structural and electrical integration of the cells within the pack as well as the packing efficiency changes. The three most common different cell formats are shown in figure 2.3. Up to this point, there is no clear decision or dominating market share for one cell format [29, 33] and all three formats are used in present automobiles [30, 31]. An ongoing research topic regarding the cell formats is the flexible adaption of manufacturing plants to produce cells with varying dimensions [34]. With the increasing variety of electrified applications, special applications with low cell unit numbers will emerge or specifically optimized cells will be needed, that do not fit any cell dimensions of a mass production cell.

2.1.2 Fast charging

There is no clearly defined time interval that defines when a charging process is considered to be a fast charging process. Usually, a state of charge (SoC) of 80 % should be reached in 10 to 20 min [36–39]. Also, fast charging is correlated with the power of the charging infrastructure and the maximum charging power the battery system can receive. Modern direct current (DC) charging infrastructure for automobiles provides charging power from 50 kW to 350 kW [18,

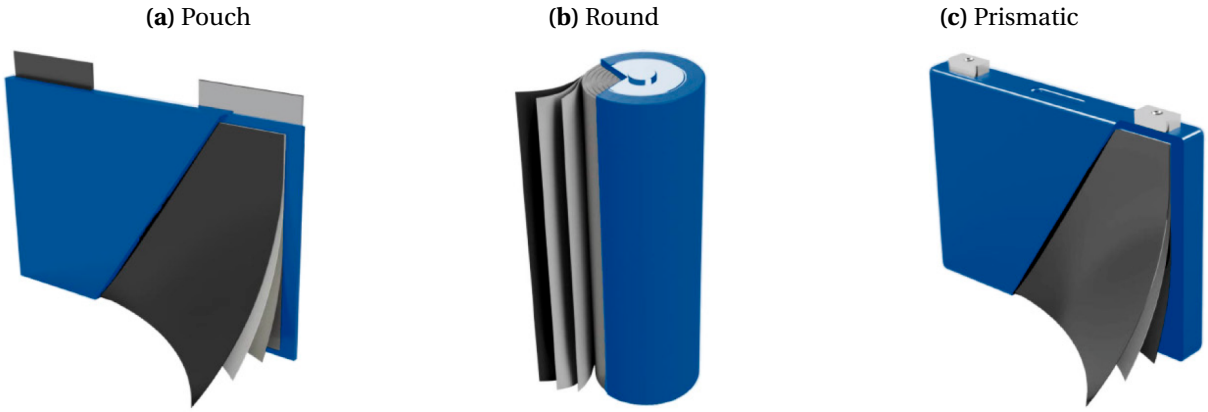

(a) Pouch **(b)** Round **(c)** Prismatic

Fig. 2.3: Illustration of different cell formats from [35]

40]. Current BEVs are with a maximum charging power of up to 270 kW not able to fully utilize the capabilities of these charging posts [41]. The current charging power leads to charge rates on the battery cells ranging from 1C to 3C whereas the rate is decreased at higher SoCs to avoid exceeding the maximum voltage of the battery cells [18, 41, 42]. Extensive research is performed to find the best load profile or charging protocol to enable a fast charging process without damaging the cell or accelerating the aging [43–45]. Despite the ongoing research, Keil et al. [45] conclude that the simple constant-current constant-voltage (CCCV) charging protocol is a good universal choice.

The limiting factors for faster charging processes are manifold. The main factors are degradation effects and low/high temperatures that lead to accelerated aging or are critical for the safety of the battery system [18, 39, 46]. Especially the maximum temperature of the battery system must be observed thoroughly during a fast charging process. Due to the high current rates, losses occur inside the cell and heat is generated, which leads to a rapid increase of the cell temperature. However, for the safety of the battery system it is crucial that the temperature of the cell stays below the allowed maximum temperature as exceeding the maximum temperature could lead to a thermal runaway of the cell. In section 2.2, the cooling of battery cells and systems will be discussed.

A detailed description of the factors influencing the lifetime and aging of the cells is given in the next paragraph.

2.1.3 Lifetime and aging

Automotive battery systems are designed for a calendrical lifetime of 8 to 12 years [22, 27] and a cyclic lifetime of 1000 to 3000 full charge/discharge cycles [21, 22, 47].

The end of life (EoL) of a battery cell is usually defined as the point in time, when its usable capacity has dropped to 80 % of its initial capacity [22, 32, 48]. An alternative definition is an increase of the internal resistance by 100 % that marks the EoL of the cell [22, 48]. Consequently, the battery system must be designed in a way, that the loads on the single cells do not lead to an EoL before the required calendrical or cyclic lifetime.

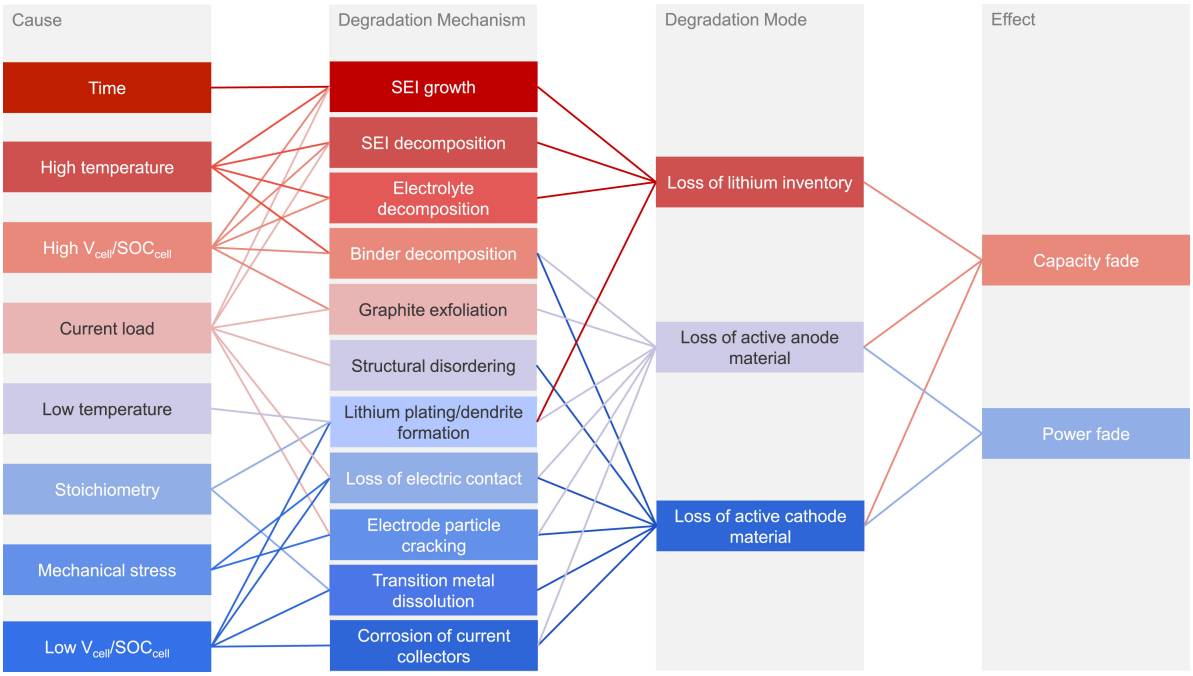

Fig. 2.4: Influencing factors and mechanisms that lead to aging of battery cells from [49]

Figure 2.4 summarizes the influencing factors, mechanisms and modes that contribute to the aging of battery cells, which is expressed in capacity and power loss respectively [49]. During a fast charging process, several of the influencing factors occur that accelerate the aging, especially high current loads and high temperatures, but also high/low cell SoCs and voltages at the beginning/end of the charging process. Depending on the initial temperature of the charging process, also low temperatures are possible.
The understanding and quantification of the influence of the single factors on the aging is currently subject to intensive research. In this work, the focus is set on the aforementioned factors that play a significant role during fast charging. Other factors, like mechanical stress due to the swelling of the cells or the pre-stressing during the assembly are not considered. Preger et al. [50] point out, that the aging behavior strongly depends on the cell chemistry. This is also confirmed by Keil et al. [45] where an LMO-NMC/graphite cell aged considerably faster than an LCO-NMC/graphite cell. They also show the significant influence of the current load: Increasing the C-rate from 0.8C to 4C reduces the number of cycles until EoL from approximately 1000 to 600 for the LMO-NMC/graphite cell. In contrast to that, the LCO-NMC/graphite cell shows a more robust behavior as increasing the C-rate from 0.91C to 4.55C only leads to a reduction of cycles until EoL from approximately 1100 to 1000. Mussa et al. [51] investigate with an LMO-NMC/graphite cell the influence of fast charging on the aging behavior and conclude, that charging with a high current until 80 % SoC leads to a lower capacity loss than charging with a low current CCCV profile until 100 % SoC. Su et al. [52] investigate NCA/graphite cells and identify the charge current as the most influencing factor on the capacity loss, followed by the cut-off voltage of the charge process and the ambient temperature.

Waldmann et al. [53] (LMO-NMC/graphite cells) and Schindler et al. [54] (NMC/silicon-graphite cells) investigate the influence of the cell temperature on the aging behavior and show, that high and low temperatures lead to an accelerated aging. Both identify an optimum cell temperature in-between the temperature extremes that leads to minimal aging. Paarmann et al. [55] and Werner et al. [56, 57] confirm that observation with NCA/graphite cells and additionally investigate the influence of temperature differences within a cell on the aging behavior. They find out, that the average cell temperature has the more significant influence on the aging behavior compared to the temperature difference within the cell but high temperature differences still show a negative impact. A similar result is derived by Fleckenstein et al. [58] with LMO-NMC/graphite cells. They quantify the influence with an approximation, stating that a cell with a high temperature delta ages like a cell without a thermal gradient at a higher mean temperature. For the cells under investigation, that equivalent aging temperature is [58]:

$$T_{\text{aging}} = T_{\text{avg}} + 10\,\% \, \Delta T_{\text{max}} \tag{2.1}$$

T_{avg} is the average cell temperature and ΔT_{max} the maximum temperature delta occurring in the cell. Hunt et al. [9] (NMC/graphite cells) also reveal a significant influence of the temperature differences and the cooling method on the capacity loss under high current loads. The capacity loss for a cell with surface cooling and a high thermal gradient in thickness direction is three times higher than for a cell with tab cooling and a low thermal gradient.
Summarizing all of these findings, an exact and general quantification of the influencing factors on the capacity and power loss is difficult as it depends on a multitude of influencing effects. However, it is clear that the current load, the cell temperature and the temperature differences within the cell are factors of great importance for the lifetime of the cell.

2.2 Thermal management in battery systems

As described previously, it is highly important for battery cells to operate at the right temperature level. In automotive battery systems, a thermal management system (TMS) is installed to heat or cool the cells and keep them at the desired temperature. For the sake of simplicity, in the following only the word "cooling" is used to describe the purpose of the TMS but heating the cells is of course also one of the central tasks of the thermal management system.

2.2.1 Classification of thermal management systems

In general, different technical approaches can be used to cool the cells in a battery system. The most common ones are air cooling and indirect liquid cooling, but also other novel cooling approaches are currently the subject of research like phase change materials or immersion cooling [59–67]. In a battery system with air cooling, a ventilation system is installed that blows air around the cells for cooling. In a battery system with indirect liquid cooling, cooling channels or plates are installed where a liquid cooling fluid – usually water-glycol – flows through. The cooling structures are connected to the battery cells or modules to remove the

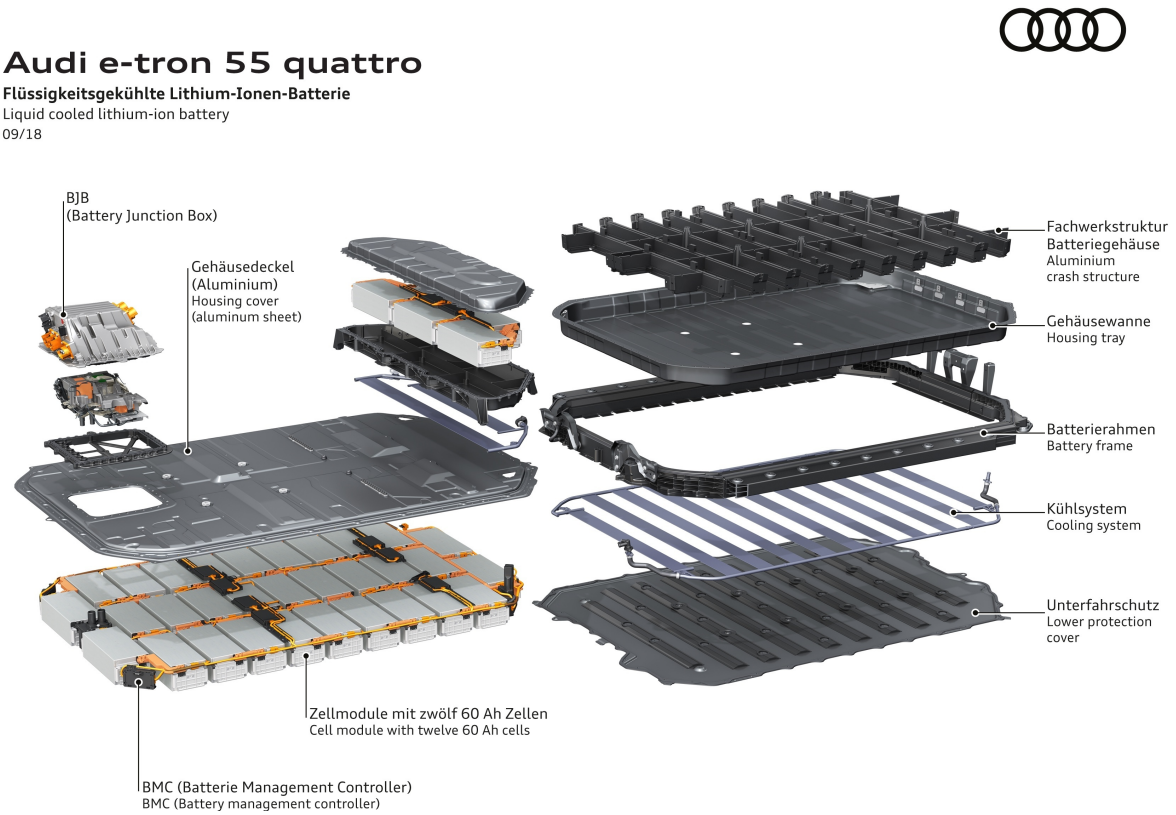

Fig. 2.5: Design of an Audi battery system, showing exemplary the integration of an indirect liquid cooling system that cools the battery modules at the bottom, taken from: [68]

heat. An example for such an indirect liquid cooling system is shown in figure 2.5, where the battery system of an Audi BEV is shown [68]. The cooling system, depicted on the right, is placed below the housing tray that contains the battery modules to cool the modules with the battery cells from the bottom. Most of today's BEVs use such an indirect liquid cooling system [6] as it offers higher cooling power compared to air cooling, is technologically further developed than other cooling approaches and may be well integrated in the rest of a BEV's thermal management system.

With respect to the battery cells, an indirect liquid cooling leads to three principle cooling locations at the cell. As presented in figure 2.6, a cell may be cooled on its large side surfaces (surface cooling), its small side surfaces (side cooling) or at the cell tabs (tab cooling). In current BEVs, the cells are usually cooled at the surface (e.g. Tesla [6]) or the side (e.g. Audi or NIO [6]).

2.2.2 Tab cooling

Tab cooling is more difficult to realize, as the cooling occurs at a current-carrying component. However, it is a present subject of research as it also offers several advantages. Due to the layered electrode stack inside the cell, the thermal conductivity is high in the direction of the tabs and thus, heat may be removed efficiently and uniform cell temperatures can be achieved [7, 8, 10]. As mentioned in section 2.1.3, Hunt et al. [9] show with pouch cells that

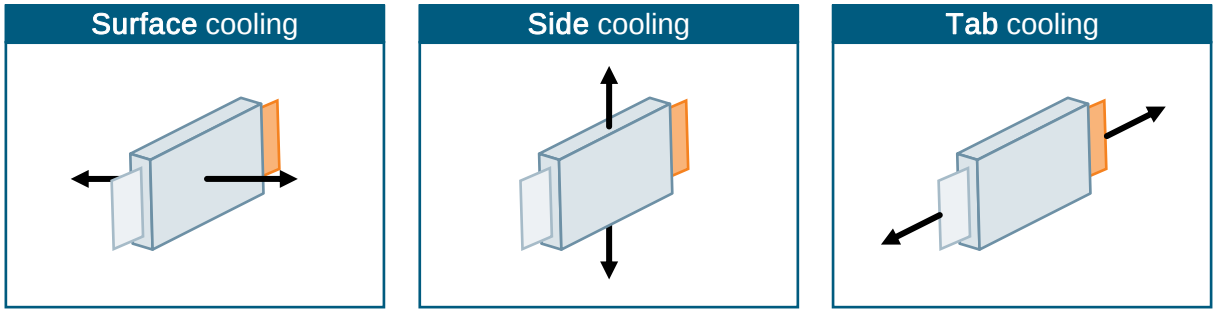

Fig. 2.6: Principal cooling locations on a battery cell

this has a positive effect on the lifetime of the cells, which is three times higher with a tab cooling compared to a surface cooling.
Most of the studies about tab cooling are focused on cell level and do not provide solutions for the realization of a tab cooling in a module. Mayer et al. [69] present a module design with a tab cooling for cylindrical cells and Heimes et al. [70] another one with pouch cells. However, both studies only analyze the module with numerical simulations and without any experimental investigation or validation.
Furthermore, studies from Li et al. [71] and Zhao et al. [7] point out, that the performance of tab cooling systems strongly depends on the tab dimensions. However, they only optimize the dimensions of the tab without considering the entire geometry of the cell and its integration in a module/pack. As described in the introduction of this thesis, this underlines the need for holistic design methods that take into account all geometric parameters of a battery cell for the thermal optimization.

2.3 Design and simulation of battery cells and systems

The fundamentals and the state of research described in this section focus on simulation aspects that are relevant to answer the proposed research questions. Thus, the electrochemical-thermal simulation of battery cells and systems as well as holistic simulation and optimization approaches are described in the following subsections.

2.3.1 Simulation of battery cells

Various different approaches exist to model the electrochemical behavior of battery cells [72–76]. Figure 2.7 shows the classification of the most common models. In general, a distinction is made between empirical/data-driven models and physics-based models. Empirical models try to describe the nonlinear relationship between current and voltage phenomenologically with simplified mathematical equations but without considering the physical processes that occur inside the cell. These models have a high computational speed but are less accurate than physics-based models [74, 76]. As the name implies, physics-based models model the electrochemical processes that take place inside the cell, namely the transport of the lithium-ions between the electrodes. They are computationally more complex than empirical models but provide a higher accuracy [74, 76].

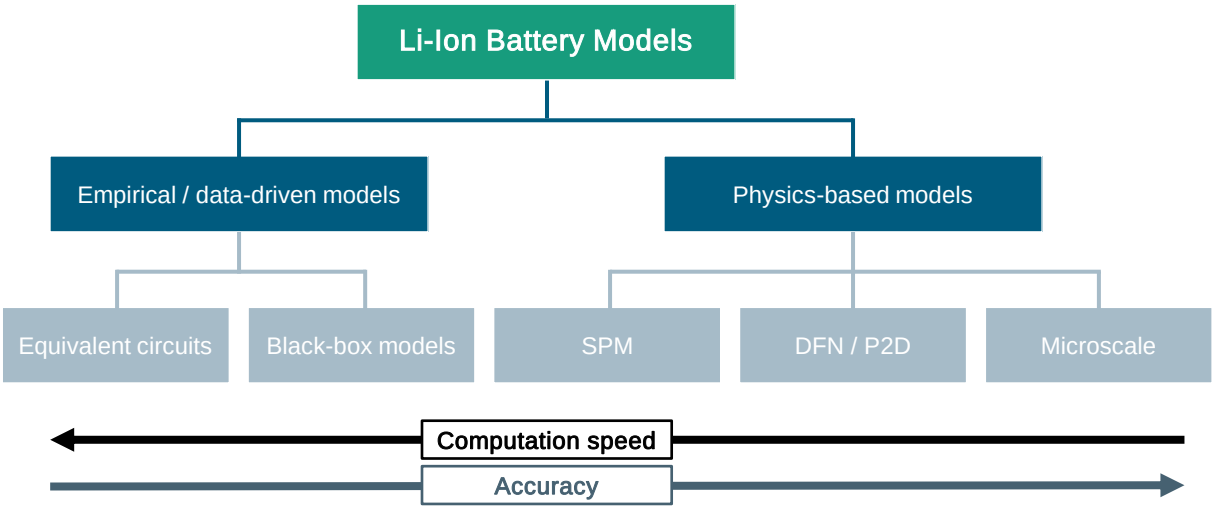

Fig. 2.7: Classification of simulation models for Li-ion battery cells (based on: [72, 74, 75])

In both modeling classes, again different modeling approaches exist. In the following, the two approaches that are used in this thesis are presented in detail: The physics-based Doyle–Fuller–Newman (DFN) model and the empirical equivalent-circuit model (ECM).

Doyle-Fuller-Newman model

The DFN model was developed by Doyle, Fuller and Newman [77] and is one of the most popular physics-based battery simulation models [72]. The idea behind the model is depicted in the middle of figure 2.8a. Anode (orange + blue), separator (light grey) and cathode (dark grey + blue) of a battery cell are represented as a one-dimensional domain. The electrodes and the separator are treated as porous materials that are filled with the electrolyte that transports the lithium ions. Within the domain of the electrodes, the electrolyte is coupled to the solid domain of the electrodes which is represented in the DFN model with spherical particles (red and green) where the lithium ions are intercalated/released. For the spherical particles, spherical symmetry is assumed so that the intercalation problem is reduced to a one-dimensional problem. Thus, the DFN model couples the one-dimensional electrolyte or electrode pair domain to multiple one-dimensional particle domains. For that reason, the DFN model is also known as Pseudo-Two-Dimensional (P2D) model.
On the described electrode pair domain, the equations for charge conservation and lithium conservation are solved to determine the electrode potentials and the lithium concentration over the domain. On the particle domain, the equations for lithium conservation are solved as well and coupled to charge and lithium conservation equations of the electrode pair domain with the Butler-Volmer equation to model the electrochemical kinetics. A detailed overview of all governing equations may be found in the original paper from Doyle, Fuller and Newman [77] or summarized in many other publications, for instance from Brosa Planella et al. [72] or Marquis et al. [78].
Due to its 1D or pseudo-2D nature, the DFN model is computationally more efficient compared to models that model the microstructure of the electrodes in detail, as depicted in

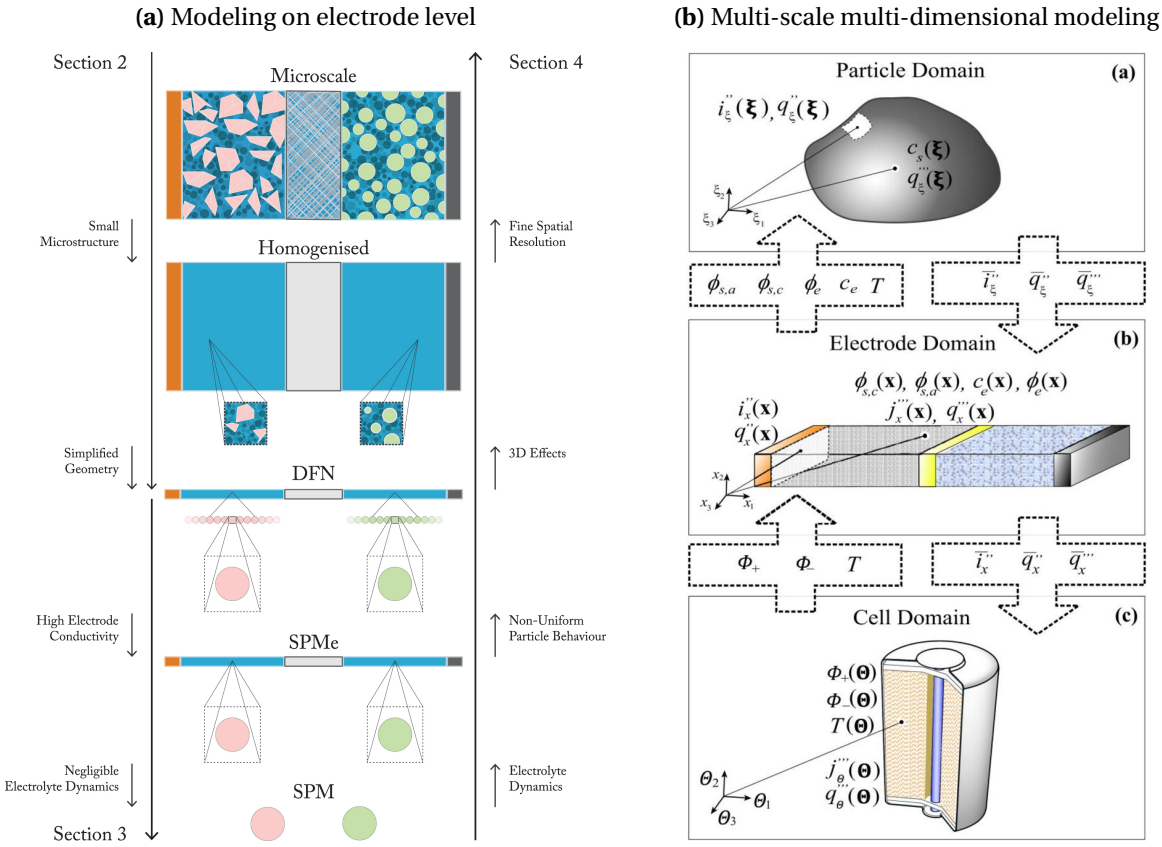

Fig. 2.8: Battery modeling approaches: (a) Physics-based battery models with a different level of detail (from [72]), (b) Multi-scale multi-dimensional nature of battery modeling (from [79])

figure 2.8a at the top [72]. Still, with its physics based basis, it is able to accurately predict the electrochemical behavior of batteries [72].
Usually, the 1D electrode pair of the DFN model is scaled in a manner, that it represents an entire battery cell. Thus, central properties like SoC, current density, potential or heat generation rate are only available as an averaged property for the entire cell and not as a three-dimensional, spatial distribution over the entire cell. This extension to model 3D problems with the DFN model is explained below.

Equivalent-circuit model

ECMs are the most popular approach to empirically model the dynamic behavior of batteries and due to their computational speed widely used in BMS [72, 74]. The idea behind the modeling approach is to describe the behavior of a battery with an electrical circuit that consists of resistors, capacitances and other electrical elements. The electrical elements are parametrized with experimental data to properly simulate the real cell behavior.
Many different configurations of ECMs are possible, depending on the combination of the electrical elements [80–84]. The most popular configuration, described by Krewer et al. as a simple ECM, consists of a voltage source connected in series with a resistor and one or multiple resistor-capacitor (RC) elements. Figure 2.9 shows such a configuration with two

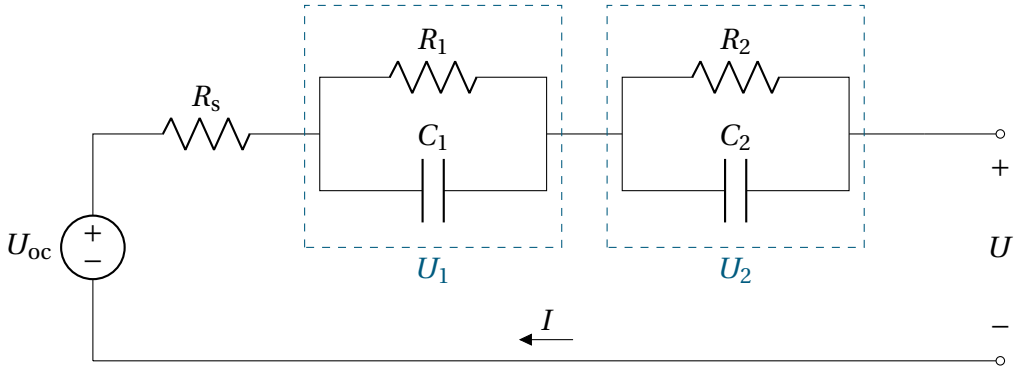

Fig. 2.9: Network representation of an equivalent circuit model with two RC elements

RC elements. The voltage source represents the open circuit voltage (OCV) of the cell, the single resistor corresponds to the internal resistance of the cell and the RC elements model the dynamic or time-dependent behavior.
Mathematically, an ECM with two RC elements is described by the following set of equations that defines the relation between the resulting voltage U of the battery cell and the current load I [85]:

$$U = U_{oc} - R_s I - U_1 - U_2 \tag{2.2a}$$

$$\frac{dU_i}{dt} = -\frac{1}{R_i C_i} U_i + \frac{1}{C_i} I \quad \text{with} \quad i = 1,2 \tag{2.2b}$$

$$\frac{dSoC}{dt} = -\frac{1}{Q_{ref}} I \tag{2.2c}$$

U_{oc} is the open circuit voltage, U_1 and U_2 are the voltage drops due to the RC elements, R_s, R_1 and R_2 are the resistances and C_1 and C_2 are the capacitances as indicated in figure 2.9. Furthermore, SoC is the state of charge, t the time and Q_{ref} the reference capacity of the cell. In practice, the OCV, the resistances and the capacitances depend on SoC and temperature, the resistances and the capacitances may also depend on the C-rate [85, 86]. That dependency may be integrated in the equations above by modeling the respective quantities as a function of C-rate, SoC or temperature. Generally, there is no distinct ECM that models the behavior of a battery cell optimally. The final setup of an ECM – so the choice of the electrical elements, integration of C-rate, SoC or temperature dependencies – depends on the problem and the battery cell that is modeled.
Like the DFN model, the ECM models the central properties of the cell like SoC, current and voltage as averaged properties for the entire cell. The extension to use the model for 3D simulations as well as the coupling to thermal models is described in the following subsection.

Thermal coupling and extension to 3D

During the charging or discharging of a battery cell, losses occur that lead to a heat generation within the cell. These losses may be divided in irreversible and reversible losses [72, 87, 88]. According to Richardson et al. [87], the irreversible losses mainly result from Ohmic losses in

the solid parts of the electrodes, the heat of mixing in the electrode particles, the polarization losses at the surface of the electrode particles as well as dissipative processes in the electrolyte. Looking at a battery cell as a black box, the irreversible losses are usually referred to as the internal resistance of the battery cell. The reversible losses stem from entropic changes in the battery cell during the intercalation/deintercalation of the Li-ions in the electrode particles [87, 89].

The total thermal losses $\dot{Q}_{\text{tot}}$, which are the sum of the irreversible losses $\dot{Q}_{\text{irv}}$ and the reversible losses $\dot{Q}_{\text{rev}}$, may be calculated as

$$\dot{Q}_{\text{tot}} = \underbrace{I\,(U_{\text{oc}} - U)}_{\dot{Q}_{\text{irv}}} \underbrace{- I\left(T\frac{\partial U}{\partial T}\right)}_{\dot{Q}_{\text{rev}}} \tag{2.3}$$

where I is the current, U_{oc} the OCV, U the voltage and T the temperature of the battery cell. Up to this point, all of the models described a lumped battery cell model where the central quantities of the cell like current, voltage, SoC and temperature were assumed to be constant over the spatial domain of the battery cell. However, this is a simplification compared to reality, as these quantities may vary in space. For instance, due to the cooling of the cell the temperatures may vary significantly and in consequence, also the current, potential and SoC distributions become spatially inhomogeneous, as these quantities depend on the temperature.

3D models of battery cells take these effects into account. With the extension to three spatial dimensions, the modeling complexity increases as various different length scales and physical domains need to be coupled withing the model [79]. This is schematically depicted in figure 2.8b. The DFN model connects the particle domain (also called microscale) and its very small length scales with the electrode domain, where the length scales are of a higher order of magnitude. By connection the DFN model with the cell domain (also called macroscale), again length scales of a higher order of magnitude are introduced. Due to this large span of length scales and dimension, these modeling approaches are called multi-scale multi-dimensional (MSMD) models [79].

The coupling of the domains occurs by exchanging the relevant physical quantities, that are of importance in each domain. The 3D physical domain of the cell is discretized with the finite volume method (FVM) [79], i.e., the continuous domain is divided in multiple small volume elements. This is a well-established approach for the simulation of thermal or fluid dynamic problems [90–92]. In every finite volume an electrochemical-thermal battery model is solved – namely the previously described DFN model or ECM – but the quantities are scaled according to the size of the volume element. As depicted in figure 2.8b, the macroscale provides the local values of the potentials Φ_+ and Φ_- and the temperature T as an input for the electrochemical-thermal model on the electrode domain. Having solved the problem on the electrode domain, the results for the volumetric current rate i and the volumetric heat generation rate $\dot{q}$ are returned to the macroscale. A detailed description of all governing

equations for a 3D MSMD model may be found in the paper of Kim et al. [79]. Here, we will focus on the 3D thermal equations as they are of importance for the later described modeling approach.

To compute the temperature field T of the battery cell on the macroscale, the heat equation is solved in the active volume of the cell. The active volume corresponds to the electrode stack of the cell where the electrochemical reactions take place. However, not the single electrodes are modeled on the macroscale but a homogenized material is assumed with averaged properties for the entire electrode stack like the density ρ, the specific heat capacity c_p and the orthotropic thermal conductivity λ. The thermal conductivity λ is orthotropic as the conductivity is higher in the in-plane direction of the stack compared to the cross-plane direction perpendicular to the electrode foils. The heat equation then reads [79]:

$$\rho c_\mathrm{p} \frac{\partial T}{\partial t} - \nabla \cdot (\lambda \nabla T) = \dot{q}_\mathrm{tot} \tag{2.4}$$

Therein, t is the time and $\dot{q}_\mathrm{tot}$ the total volumetric heat generation rate which is derived from equation 2.3 and given as a function of volumetric current rate i, open circuit voltage U_OC, voltage U and temperature T:

$$\dot{q}_\mathrm{tot} = i\,(U_\mathrm{oc} - U) - i\left(T\frac{\partial U}{\partial T}\right) \tag{2.5}$$

For the integration of boundary conditions in the heat equation, like conductive or convective heat transfer on the outer surfaces of the investigated volume, the reader is referred to literature [79, 90–92].

Depending on the electrochemical-thermal battery model that is solved on the electrode domain, the computation time of a 3D model varies significantly. Using a DFN model leads to higher computation times compared to an ECM as more equations – especially due to the considered particle domain – need to be solved. The computation time for a charge cylce of a single battery cell with the DFN model is in the range of several hours, with the ECM it is in the range of several minutes to a few hours.

2.3.2 Simulation and optimization of battery systems

With the previously described 3D modeling approaches it is not only possible to simulate a single cell, but also entire battery modules or packs including the thermal management system. As the modeling approaches are based on well-established 3D simulation techniques (finite volume or finite element method), a combination with any thermal or fluid dynamic problem is seamlessly possible. However, the computing times are high and in design optimization, usually only a very limited number of variants can be calculated [93, 94].

Consequently, for the design and optimization of battery systems including a thermal management system, 1D simulation approaches are used. The battery cells are then modeled as lumped thermal masses with a 1D electrochemical-thermal battery model and connected via

thermal boundary conditions like 1D pipe structures or convection boundary conditions for the cooling [95–101].

However, information is lost through this reduction of dimensions, for instance about temperature differences within a single cell or geometrical details of the cooling system. A solution for this problem is the development of so-called meta-models or surrogate models. These models reduce the complex model to a simplified model that only contains certain input and output variables of interest [102]. The meta-model is usually build upon a limited number of results of the more complex model [102].

In recent years, the usage of meta-models for the design and optimization of battery systems increased strongly, as the review papers of Ebbs-Picken et al. [103] and Fayaz et al. [104] show. However, with respect to a thermally optimal cell design, these meta-models focus almost exclusively on the temperature difference between different cells and not on the prediction of the maximum temperature difference within an individual cell and the consequences for the battery lifetime (e.g. [105] or [106]). Lin et al.[15], Kerler [16] and Kerler et al. [17] describe a meta-model that is able to predict the temperature delta within a single cell which is integrated in a battery pack model to perform analyses on system level. However, the geometrical parameters of the cell are not an input variable of the meta-model so that for each cell geometry a novel meta-model needs to be derived.

Within the literature review, there was no model of a battery system or module found that predicts the maximum temperature difference within a single cell while still being able to vary all relevant parameters for the geometric and thermal design of the cell. This shows the lack of flexible modeling approaches and analyses that connect the thermal behavior a battery cell with the system level to find optimized battery cell geometries.

2.4 Meta-modeling using artificial neural networks

Various different meta-modeling techniques exist, ranging from polynomial approximations over Gaussian process regression to artificial neural networks (ANN) [102, 107]. For the sake of simplicity, artificial neural networks will simply be called neural networks (NN) in the following. With the generally increasing interest in machine learning approaches over the past years, neural networks became more attractive for the solution of battery modeling problems. Having sufficient training data, with NNs complex and highly nonlinear problems can be accurately modeled without any previous knowledge of the underlying processes or system.

In literature, NNs have for example successfully been used for the prediction of the state of charge [108–113], state of health [114–118] or heat generation [119] of a battery cell. Also the calculation of the average, core or surface temperature of battery cells using NNs has successfully been demonstrated [11, 120–126]. The meta-model mentioned at the end of the previous section that predicts the temperature difference within the cell, does not use a NN but Gaussian process regression. To the authors knowledge, besides that approach there is no meta-model that predicts the temperature difference within a single cell.

The literature analysis shows that due to its high capabilities, the usage of NNs for meta-modeling is very attractive. As the meta-model that is developed in the present thesis is also based on a neural network, in the following section the fundamentals of neural networks are briefly explained. For more detailed and extensive information about neural networks, the reader is referred to literature: [127–135]

2.4.1 Multilayer feedforward neural networks

ANNs try to mimic the functionality of biological brains [127]. Their key feature is the ability to learn the relationship between variables independently and purely on the basis of training examples. Consequently, with the trained model, unknown output values may be predicted. Thereby, it is possible to predict discrete outputs (classification) or continuous outputs (regression) [129], whereas in the following the focus is on continuous outputs.
The principal structure of a NN is displayed in figure 2.10 [134]. It consists of neurons (the colored circles in figure 2.10) that are connected with each other for the exchange and processing of the data. The neurons are grouped in so-called layers: The input layer accepts and processes the input values, the output layer contains the predicted output values. The layers in-between are called hidden layers. If multiple hidden layers exist, the network is referred to as a multilayer neural network [131]. While the structure of the input and output layer is predetermined by the problem, the network architecture of the hidden layers is variable and can be optimized for the specific problem by adjusting the number of hidden layers and the number of neurons in each layer.
The NN in figure 2.10 illustrates a feedforward network. This type of network is characterized by the fact that the neurons are only connected to neurons in the next layer and the flow of information is in forward direction [128]. This is indicated by the grey arrows connecting the single neurons in figure 2.10.
The data processing within a single neuron is depicted in figure 2.11 [127]. The grey arrows symbolize the same grey arrows as in figure 2.10 connecting the single neurons. The basic tasks of the neuron are the aggregation of the information that comes as an input from the previous layer and its neurons and the processing of that information, called activation, to generate the new output.

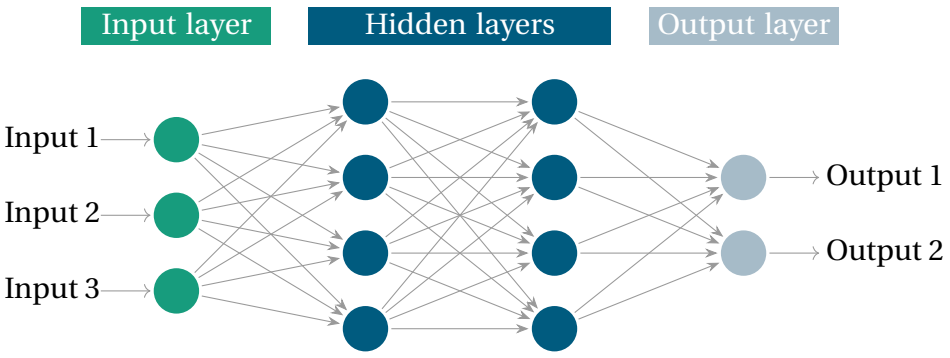

Fig. 2.10: General structure of a multilayer feedforward neural network (based on: [134])

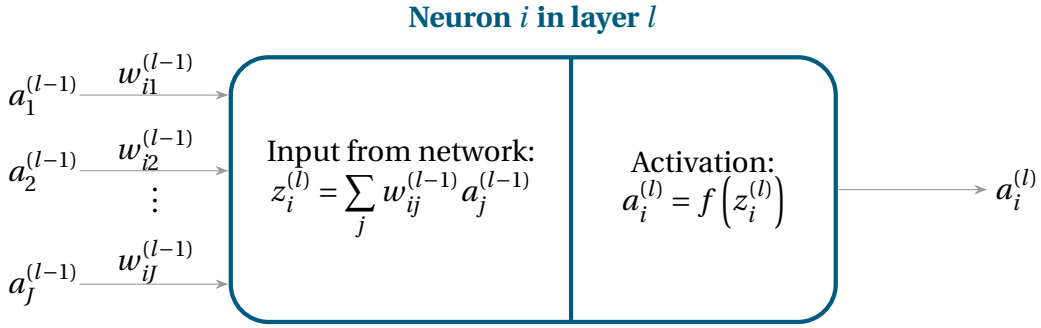

Fig. 2.11: General structure and functionality of a single neuron i in a hidden layer l (based on: [127])

The input information consists of the outputs $a_j^{(l-1)}$ from the previous layer $l-1$ and the so-called weights $w_{ij}^{(l-1)}$ that connect a neuron j from the previous layer with the current neuron i of the current layer l. The weights determine the strength of the connection between two neurons and in how far the current neuron is influenced by the previous neuron. The neuron computes the weighted average $z_i^{(l)}$ of all inputs with the given weights and calculates its own output value – also called activity – with a defined activation function $f(z)$. The activation function is usually identical for all neurons of a layer. Simple activation functions like the sigmoid or the ReLU function are preferred as the potential of a neural network does not arise from the single activation functions but of the combination of many neurons with simple activation functions. Still the activation function is a parameter that needs to be optimized for the specific problem.

2.4.2 Learning process

During the learning or training process of the NN, the aforementioned weights within the network are optimized so that the error between the true output value and the predicted output value of the NN is minimized. This is done with an iterative optimization process [131]. The training examples are fed to the neural network and the predicted output values are calculated. They are consequently compared to the true value and the error (also called cost function) is calculated with a predefined error measure. The error value is propagated backwards through the network and the weights are gradually adjusted to minimize the error. This second step, where the weights are optimized, is called backpropagation. For a detailed description of that process the reader is referred to literature: [128, 131, 132, 134]. Presenting all training values to the neural network and performing the forward phase and the backpropagation once is referred to as one training epoch. Multiple training epochs are repeated iteratively until the error is minimized. This marks the end of the training process.

Influencing numerical parameters

The training process is influenced by numerical parameters, two of them are briefly discussed here. During backpropagation, a gradient descent is applied to adjust the weights and minimize the error. Like in every gradient descent process, there is a predefined step size that determines the size of the step towards the minimum [131]. Choosing a large step size leads

to a faster convergence of the algorithm but the minimum value might not be reached. On the contrary, a small step size increases the chance to find the minimum value but slows down the convergence. Thus, the step size – in the backpropagation algorithm called learning rate – needs to be chosen appropriately.

The second influencing parameter is the so-called batch size. During one training epoch, the weights of the network can be adjusted after every training sample (batch size = 1) or after the network has seen a fixed size of n training samples (batch size = n). Adjusting the weights after it has seen all of the training samples does theoretically lead to a more accurate gradient descent vector which improves the convergence [131]. However, the probability is higher that the optimization leads to a local minimum. In contrast to that, a small batch size makes the gradient descent more stochastic in nature and thus, the probability is higher that local minima are avoided and a global minimum is found [131].

Furthermore, it is also noted that the data for the training of the NN is usually scaled to avoid numerical problems with different orders of magnitudes in the input and output values. Typically, the values are scaled so that they are in the range between 0 and 1.

Overfitting and underfitting

The property of NNs that they are solely adjusted and fitted by learning from the training data leads to the problem of overfitting or underfitting [131]. A model that is overfit, performs exceptionally well on the training data and has a very low training error. However, as soon as data is presented to the NN that it has never seen before, the predicted output is far away from the true value and thus, the actual output error is high. A model that is underfit, performs both on the training data and also on foreign data badly which results in high error values.

For both overfitting and underfitting there are two central causes: the network architecture and the number of training epochs.

If the network architecture is too detailed and complex (i. e. a high number of hidden layers and/or a high number of neurons per layer), the neural network is able to learn details that are specific for the training data but not for the general modeling problem. This might lead to overfitting. If the network architecture is too less detailed and simple (i. e. a very low number of hidden layers and/or a low number of neurons per layer), the network is not able to model the complex relations between the input and the output parameters and thus, performs badly. This leads to underfitting.

The second cause for overfitting and underfitting – the number of training epochs – is illustrated in figure 2.12. If the number of training epochs is low, the optimization process may not yet have reached the minimum error (underfitting). If the number of training epochs is too high, the training error is minimized but applying the NN on new data – called validation/test data in figure 2.12 – leads to increased error values (overfitting).

To avoid the problem of overfitting or underfitting and to create a model that generalizes well, the architecture of the NN should be as simple as possible but as complex as necessary. Also the training process should be observed thoroughly to end the training when the valida-

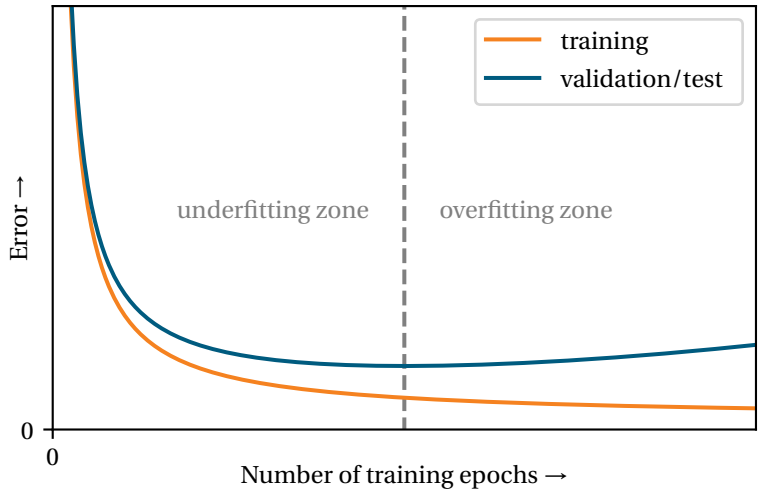

Fig. 2.12: Typical relationship between the training and the validation/test error over the number of training cycles (based on: [128])

tion/test error has reached its minimum (in figure 2.12 this is around the vertical, dashed grey line in-between the underfitting and overfitting zone).

2.4.3 Hyperparameter optimization

All settings of a neural network that control the algorithms behavior and may be chosen by the user are summarized under the term hyperparameters. In the sections above, several of these hyperparameters have been introduced:

- Number of hidden layers
- Number of neurons
- Activation function in hidden layers
- Batch size
- Learning rate

To develop an optimized neural network that leads to accurate predictions and generalizes well, these hyperparameters need to be optimized. To do so, the following procedure is usually applied. The available data is split in three data sets [128]:

1. *Training set*: The training set contains the majority of the data and is used for the training of the NN.
2. *Test set*: The test set is used at the end of the training process to evaluate its performance and generalization capabilities.
3. *Validation set*: The validation set is used during the hyperparameter optimization process to evaluate the performance of the neural network.

Consequently, the training and the validation set are used to optimize the hyperparameters by training different neural network configurations and evaluating their performance with the validation set. The test set is then applied at the end to judge the performance of the final and optimized trained network.

The distinction between test and validation set is important. As the validation set influences the design of the neural network by testing its performance during the hyperparameter optimization, it has a direct influence on the model. Thus, the validation set is not "new" to the neural network at the end of the training process and must not be taken to evaluate the generalization capabilities and accuracy of the neural network. This should only be done with the test set, which is entirely new to the trained NN.

To make the hyperparameter optimization process less dependent on the arbitrarily chosen training and validation set and to reduce statistical errors, a methodology called k-fold cross validation is used [128, 132]. During the hyperparameter optimization, the training and the validation set are combined and split into k different data sets. Of these k sets, one is used as a validation set and the others are used for the training. This is repeated k times so that every set acted once as a validation set. Afterwards, the averages of the training and validation errors are formed to evaluate the performance of the NN. Repeating the k-fold cross validation multiple times reduces possible statistical errors even further and thus, improves the choice of the right hyperparameters. This is called repeated k-fold cross validation.

2.5 Mathematical fundamentals

In the following, some general mathematical fundamentals used in this thesis are explained.

2.5.1 Latin hypercube sampling

If an experiment or a simulation is to be carried out with different, varying parameters, the number of experiments can quickly become very high. To avoid such a high number of experiments, the parameters must be chosen appropriately to ensure, that the entire parameter space is covered but the number of experiments is as low as possible. This issue is also referred to as deign of experiments. Simply choosing random parameters within the parameter space does not lead to a good coverage of the parameters space.

Latin hypercube sampling is a statistical method that solves that issue [136]. Random samples are created within the parameter space, but the sampling method ensures that the entire parameter space is covered. The parameter space is divided in a prescribed number of samples and the samples are subsequently drawn so that one sample lies in every division of the space. This is depicted in figure 2.13b, where five samples are shown in a two-dimensional parameter space. The division of the parameter space is represented by the black grid. In comparison to that, figure 2.13a shows a random sampling in the same parameter space where the five samples are clearly less equally distributed in the parameter space.

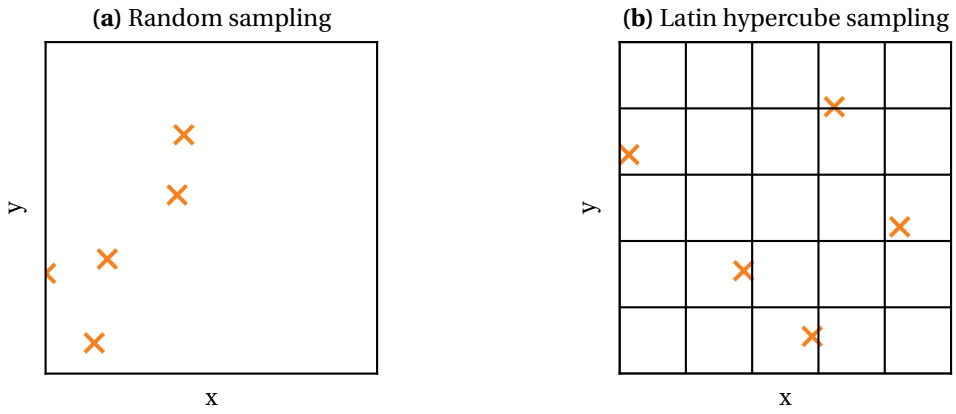

Fig. 2.13: Visual comparison of random sampling (a) and Latin hypercube sampling (b) with two parameters and five samples

2.5.2 Pearson correlation coefficient

To identify and analyze relationships between parameters in large data sets, correlation coefficients can be used. One of the most commonly used correlation coefficients is the Pearson correlation coefficient r_{xy} [137]. It is defined as the covariance of two variable sets $\boldsymbol{x}$ and $\boldsymbol{y}$ divided by the product of the standard deviations of $\boldsymbol{x}$ and $\boldsymbol{y}$ [138]:

$$r_{xy} = \frac{\mathrm{cov}(\boldsymbol{x}, \boldsymbol{y})}{\sigma_x \sigma_y} = \frac{\sum_{i=1}^{n}(x_i - \bar{x})(y_i - \bar{y})}{\sqrt{\sum_{i=1}^{n}(x_i - \bar{x})^2}\sqrt{\sum_{i=1}^{n}(y_i - \bar{y})^2}} \tag{2.6}$$

The coefficient ranges from -1 to $+1$ and describes whether there is a linear relationship between two variables. Positive values indicate a positive relationship between the variables, negative values a negative relationship. If the value is 0, there is no linear relationship between the variables (but a nonlinear relationship would still be possible). In figure 2.14 four exemplary correlations and the corresponding Pearson correlation coefficient r_{xy} are given to clarify the understanding of the coefficient.

2.5.3 Error measures

The following error measures are used in this thesis to compare results or as a loss function during the training of the neural network.

Mean absolute error

The mean absolute error (MAE) between the true values $\mathbf{y}_{\mathrm{true}}$ and the predicted values $\mathbf{y}_{\mathrm{pred}}$ is defined as the arithmetic mean of the absolute error over n samples:

$$MAE(\mathbf{y}_{\mathrm{true}}, \mathbf{y}_{\mathrm{pred}}) = \frac{1}{n}\sum_{i=1}^{n}\left|y_{\mathrm{true},i} - y_{\mathrm{pred},i}\right| \tag{2.7}$$

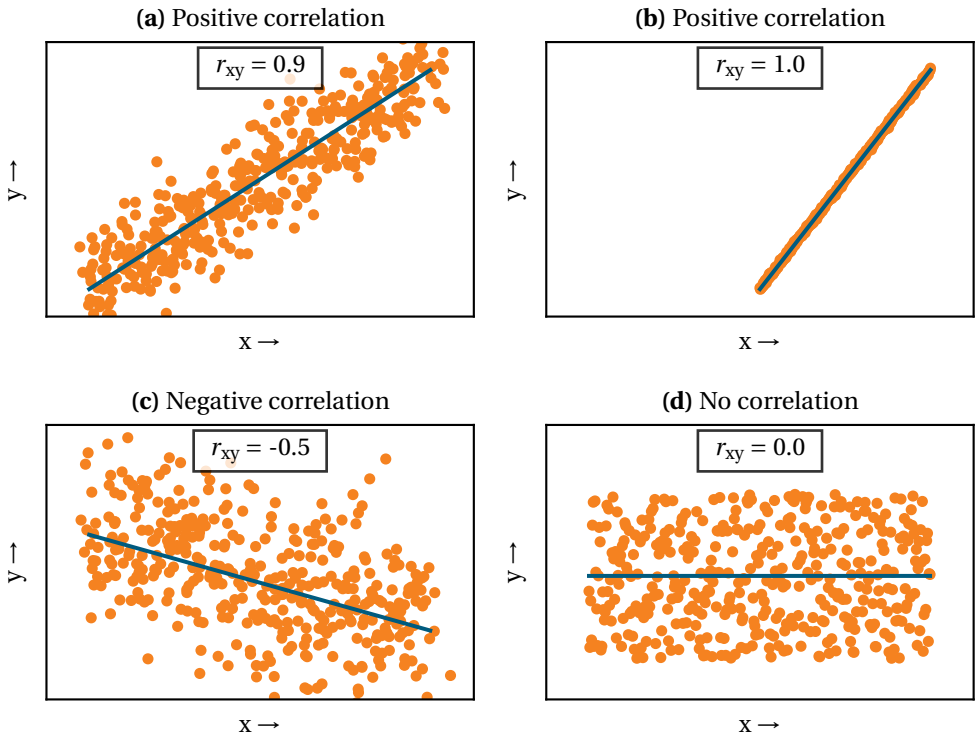

Fig. 2.14: Exemplary scatter plots with the corresponding Pearson correlation coefficient r_{xy}. The blue line shows the mean value of the scattered points.

Mean squared error

The mean squared error (MSE) between the true values $\mathbf{y}_{\text{true}}$ and the predicted values $\mathbf{y}_{\text{pred}}$ is defined as the squared error between the values over n samples:

$$MSE(\mathbf{y}_{\text{true}}, \mathbf{y}_{\text{pred}}) = \frac{1}{n} \sum_{i=1}^{n} \left(y_{\text{true},i} - y_{\text{pred},i}\right)^2 \tag{2.8}$$

Compared to the MAE, the MSE weights high error values stronger as the error between the true and the predicted value is squared.

Root mean squared error

The root mean squared error (RMSE) is defined as the square root of the MSE:

$$RMSE(\mathbf{y}_{\text{true}}, \mathbf{y}_{\text{pred}}) = \sqrt{MSE(\mathbf{y}_{\text{true}}, \mathbf{y}_{\text{pred}})} \tag{2.9}$$

Compared to the MSE, the RMSE has the same unit like the values under investigation.

3 Simulation models and experimental setup

3.1 Overall modeling approach

As mentioned in section 1.2, the goal of the simulation model is a fast (<1 min) prediction of the temperature differences within a single battery cell of a battery module during a charging process, while still being able to vary all relevant parameters for the thermal design. To achieve this goal, the modeling procedure was divided in three steps, that are depicted in figure 3.1.

At first, a 1D physics-based electrochemical-thermal model (ETM) of a battery cell is set up (section 3.2). A physics-based model is chosen, as it is able to accurately predict the electrochemical-thermal behavior of the cell (see also section 2.3). A central output of the model that is needed for the further modeling process is the volumetric heat generation rate. It quantifies the heat that is generated during the operation of the cell and is thus crucial for the modeling of the thermal behavior of the cell. Due to its 1D-nature, the ETM is computationally efficient but not able to predict a spatially resolved thermal behavior. It only outputs volume averaged values.

As a second step of the modeling procedure, the ETM is used to calibrate and parametrize an equivalent-circuit model (ECM) of the battery cell (section 3.3). The ECM is used in two different ways: On the one hand, it serves as a 1D battery cell model for the later modeling of the modules as it has an even higher computational efficiency than the ETM. On the other hand, it is used to create a 3D model of the battery cell. The 3D model is able to accurately predict the spatial temperature distribution occurring in the battery cell and considers the spatial influence of the electrochemistry (e.g. current distribution, locally different SoC, etc.). It is based on the finite volume method and couples via the MSMD approach a spatially resolved thermal model with a spatially resolved electrochemical model, whereas the electrochemical model is represented by the ECM. This results in a model with computation times in the range of minutes to hours, which is still significantly faster than coupling the computationally more expensive physics-based models in a 3D simulation. It also enables the application of different thermal boundary conditions or interfaces to model the heat exchange with the environment, for example the external cooling/heating of the cells with different cooling methods. Consequently, all aspects for the electrical and thermal integration of the cell into a module or pack are considered in this model.

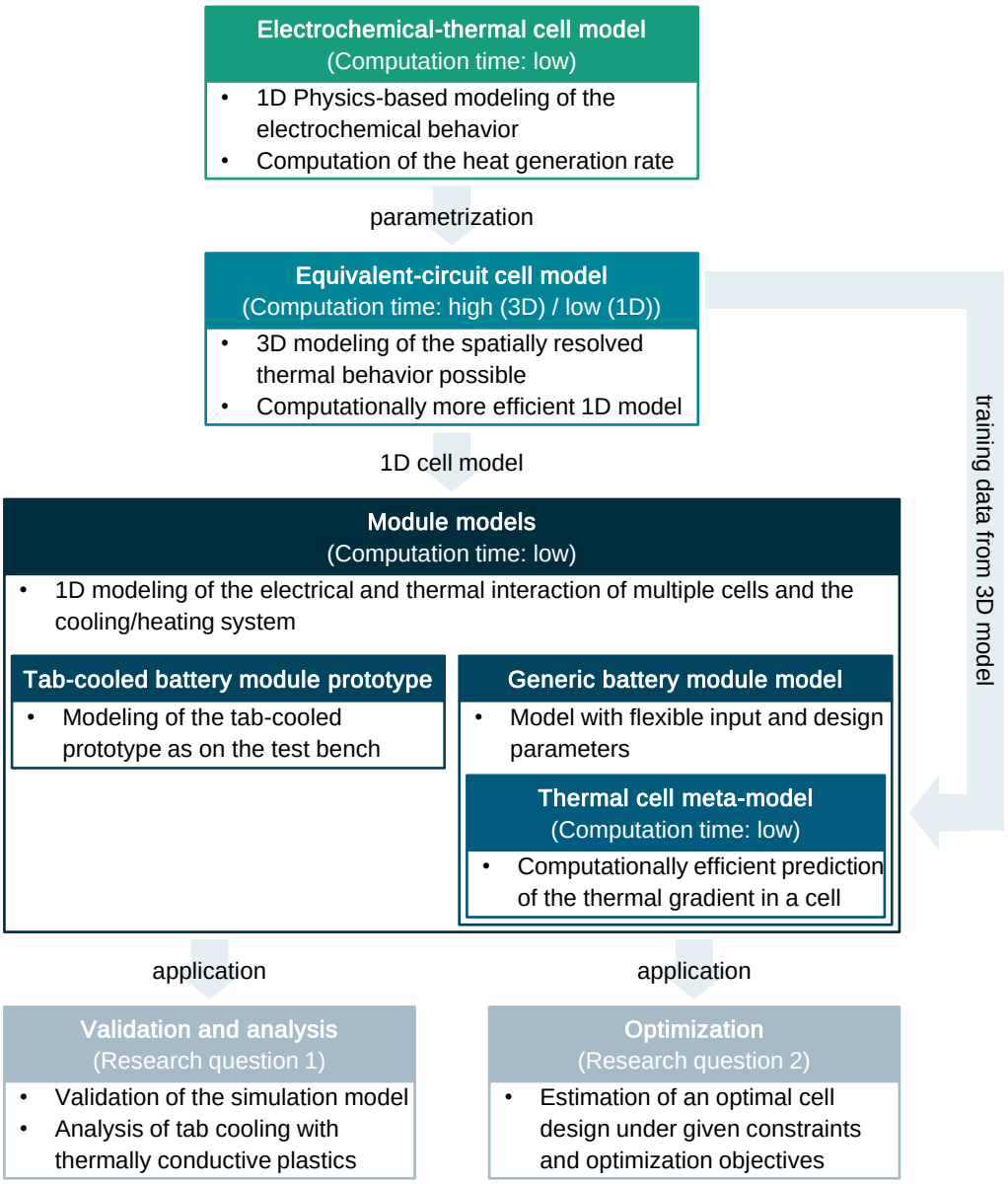

Fig. 3.1: Overall modeling approach

However, the computation times of the 3D model are still too high to be used in an efficient optimization procedure. This issue will be addressed in the third modeling step, where the 1D module models are created. Two different models are set up to address the two proposed research questions (see section 1.2).
In section 3.4 the model of the tab-cooled battery module prototype is described. The model is based on a new battery module prototype with a tab cooling system using thermally conductive plastics. Experiments on a test bench are performed to investigate the thermal behavior of the tab cooling system and to generate measurement data for the validation of the simulation model. With the combination of the experimental investigations and the simulation model, the first research question will be answered and the validity of the basic 1D module modeling approach will be reviewed. However, neither the experimental investigations nor the proposed model do include information about the temperature differences within the single cells.
Therefore, in section 3.5 a second, generic battery module model is developed. The basic modeling approach is identical to the validated 1D model of the module prototype but it is extended with a novel thermal cell meta-model (CMM) that is able to rapidly predict the maximum temperature delta in a single battery cell after a charging process. The CMM is a data-driven, numerical simplification of a 3D model which uses all relevant cell design, thermal and electrical parameters of a charging process as an input and outputs the maximum and minimum temperature occurring within a cell. It consists of a neural network that is trained with data generated by the 3D ECM. After the simulation of a charging process with the generic 1D module model, the CMM is evaluated in a post-processing step and the temperature difference within the single cells is predicted.
Providing very low computation times, the generic battery module model is used to answer the second research question as it enables the analysis and optimization of the conflict of objectives between fast charging, lifetime and energy density which was described in chapter 1.

Reference cell KIT20

The physics-based model that is used as a basis of the previously described modeling approach is adjusted so that it fits to the reference cell that is used in the battery module prototype. This enables the experimental validation of the proposed model. As a reference cell a 20 Ah pouch cell is used, called KIT20 cell, which was manufactured at the Battery Technology Center (BaTec), Institute for Applied Materials - Energy Storage Systems of the Karlsruhe Institute of Technology [139]. Table 3.1 summarizes the relevant data of the cell and indicates the data sources. Most of the properties are given in the data sheet [139], but some information about the internals of the cell were received directly from the manufacturer. The thermal conductivity and the specific heat capacity were measured by M. Miller at the Fraunhofer ICT and are in good agreement with values from literature [140, 141]. Also the weight and the dimensions of the cell were measured, central dimensions of the cell are given in figure 3.2.

Tab. 3.1: Properties of the KIT20 cell

Property	Value	Source
Nominal capacity	20 A h	[139]
Weight	543 g	Fraunhofer ICT
Anode material	Graphite	[139]
Cathode material	NMC111	[139]
Max. operating voltage	4.2 V	[139]
Nominal voltage	3.7 V	[139]
Min. operating voltage	3.0 V	[139]
Max. continuous charge current	60 A (3C)	[139]
Max. continuous discharge current	100 A (5C)	[139]
Operating temperature charge	0 °C to 40 °C	[139]
Operating temperature discharge	−30 °C to 60 °C	[139]
Thermal conductivity in-plane	$\lambda_{\mathrm{av},\parallel} = 47.5\,\mathrm{W\,m^{-1}\,K^{-1}}$	Fraunhofer ICT
Thermal conductivity cross-plane	$\lambda_{\mathrm{av},\perp} = 1.16\,\mathrm{W\,m^{-1}\,K^{-1}}$	Fraunhofer ICT
Specific heat capacity	$c_{\mathrm{p,av}} = 920\,\mathrm{J\,kg^{-1}\,K^{-1}}$	Fraunhofer ICT
Number of anodes	22	BaTec, IAM-ESS
Number of cathodes	21	BaTec, IAM-ESS
Number of separators	44	BaTec, IAM-ESS
Dimension anodes	$w = 212\,\mathrm{mm} \times h = 139\,\mathrm{mm}$	BaTec, IAM-ESS
Dimension cathodes	$w = 208\,\mathrm{mm} \times h = 135\,\mathrm{mm}$	BaTec, IAM-ESS

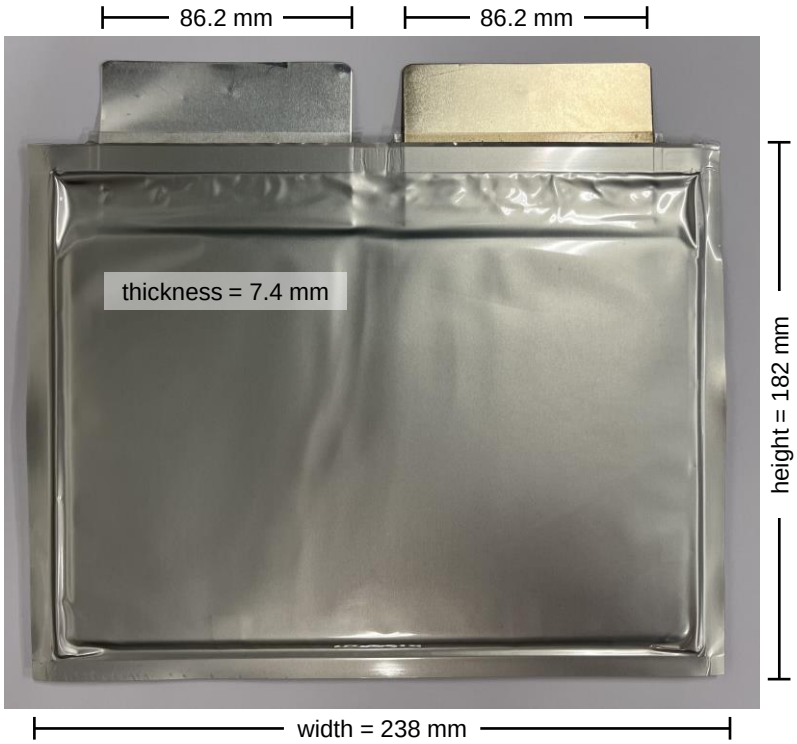

Fig. 3.2: KIT20 cell including the central dimensions

3.2 Electrochemical-thermal cell model

Several different physics-based approaches exist to model the electrochemical-thermal behavior of battery cells, as described in section 2.3. Here, the Doyle–Fuller–Newman (DFN) model is chosen [77]. For a 1D model, it offers the highest accuracy and is applicable for a wide range of operating conditions while still providing acceptable computation times [72]. Other popular 1D models, like the Single Particle Model (SPM), are less computational expensive but also less accurate at high C-rates [72], which is unsuitable for the present use case. For a detailed description of the DFN model, the reader is referred to section 2.3.
Several implementations of the DFN model exist in commercial [142–144] or open-source software codes [145–148]. In the present work, the implementation of the open-source software tool PyBaMM, Version 22.9, is used [78, 149, 150]. PyBaMM is a battery simulation tool written in the programming language Python. For the following reasons it is the preferred choice for the modeling:

- Being an open-source software, it offers a greater flexibility for own model developments compared to commercial software and an easier accessibility of the own work for other researchers and future developments.
- As it builds on the popular programming language Python, it is easy to extend and link the models to other, existing Python models.
- There are multiple, documented data sets for the parametrization of the physical model parameters available. The parametrization of physics-based battery models is difficult and crucial for their accuracy [151]. So having well parametrized data sets for different cell chemistry available, is a great advantage compared to other tools.

Parametrization

The DFN model is parametrized so that is fits well to the KIT20 reference cell. From the existing parameter sets in PyBaMM, the data set from Mohtat [152] was chosen as it is based on a pouch cell with a graphite anode and an NMC cathode, which agrees with the electrode materials of the KIT20 cell. Compared to the default data set, the PyBaMM parameters shown in table 3.2 were changed in order to adjust the data to the KIT20 cell and improve the fit.
As there is only one width and height for both electrodes in PyBaMM, the average width and height from the KIT20 cell (see table 3.1) was applied. The thicknesses of the separator, electrodes and current collectors were adjusted so that the overall thickness of the cell and the capacity are in good agreement with the KIT20 cell. The same applies for the specific heat capacity of the electrodes. The entropic change of the electrodes was changed as later results showed, that the parameters from the Mohtat data set did not fit well with the KIT20 cell experimental data. Consequently, the entropic change from the PyBaMM data set from O'Regan [153] was used as this significantly improved the fit.

Tab. 3.2: Changed parameters of the PyBaMM DFN model compared to the default parameter set from Mohtat [152]

Parameter	Value
Nominal capacity	20 A h
Lower voltage cut-off	3 V
Number of electrodes connected in parallel to make a cell	42
Electrode width	210 mm
Electrode height	137 mm
Negative current collector thickness	5 µm
Negative electrode thickness	44 µm
Positive current collector thickness	10 µm
Positive electrode thickness	51 µm
Separator thickness	56.5 µm
Negative electrode specific heat capacity	1050 $J kg^{-1} K^{-1}$
Positive electrode specific heat capacity	1050 $J kg^{-1} K^{-1}$
Negative electrode OCP entropic change	from [153]
Positive electrode OCP entropic change	from [153]

Validation

In the data sheet of the KIT20 cell [139] experimental data is available which is used to validate the parametrization of the 1D cell model. The charge and discharge behavior for different C-rates at room temperature is given, as well as the open circuit voltage (OCV). For these load cases, simulations with the parametrized DFN model were performed under identical conditions. The ambient temperature is set to 20 °C and a sufficiently high heat transfer coefficient of 1000 $W m^{-2} K^{-1}$ is applied to keep the battery temperature constant.

Figure 3.3 shows the voltage results for a discharging process with 1C to 5C over the capacity. For low C-rates (1C, 2C), the DFN model overestimates the overall discharge capacity, for high C-rates (4C, 5C) the overall discharge capacity is underestimated. Also the voltage drop predicted by the DFN model at the beginning of the discharge process is always slightly higher compared to the reference. Still, with a root mean squared error (RMSE) below 0.08 V and a mean absolute error (MAE) below 0.06 V the model agrees well with the reference data.

Figure 3.4 shows the voltage results for a charging process with 1C, 2C and 3C over time. The time point where the DFN model reaches the upper cut-off voltage agrees for a 2C charging very well with the reference data. During a 1C charging it is slightly overestimated and during a 3C charging slightly underestimated. Also, the higher the C-rate the greater the deviations between the model and the reference become. With a RMSE below 0.1 V and a MAE below 0.08 V, the model fits well to the reference data.

In figure 3.5, the result for the OCV over SoC is presented. The DFN model is not able to make a difference between the charge and discharge OCV, thus, there is only one graph for the simulation model. With an RMSE of 0.09 V and an MAE of 0.07 V, the simulation is in good agreement with the reference during discharge. An even better agreement is observed for the

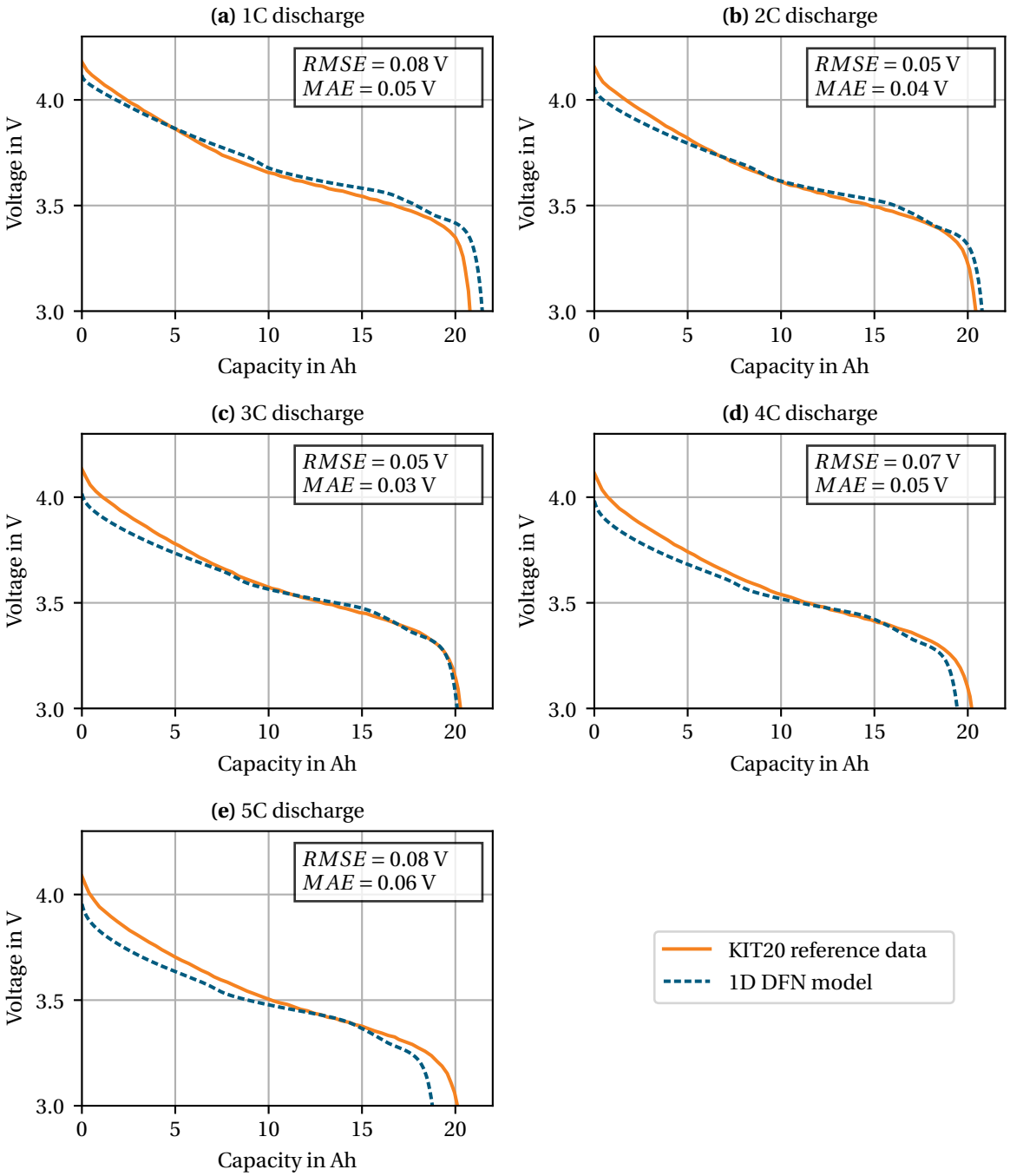

Fig. 3.3: Comparison of the discharge behavior between the measurements of the KIT20 reference cell [139] and the 1D electrochemical-thermal simulation with the DFN model

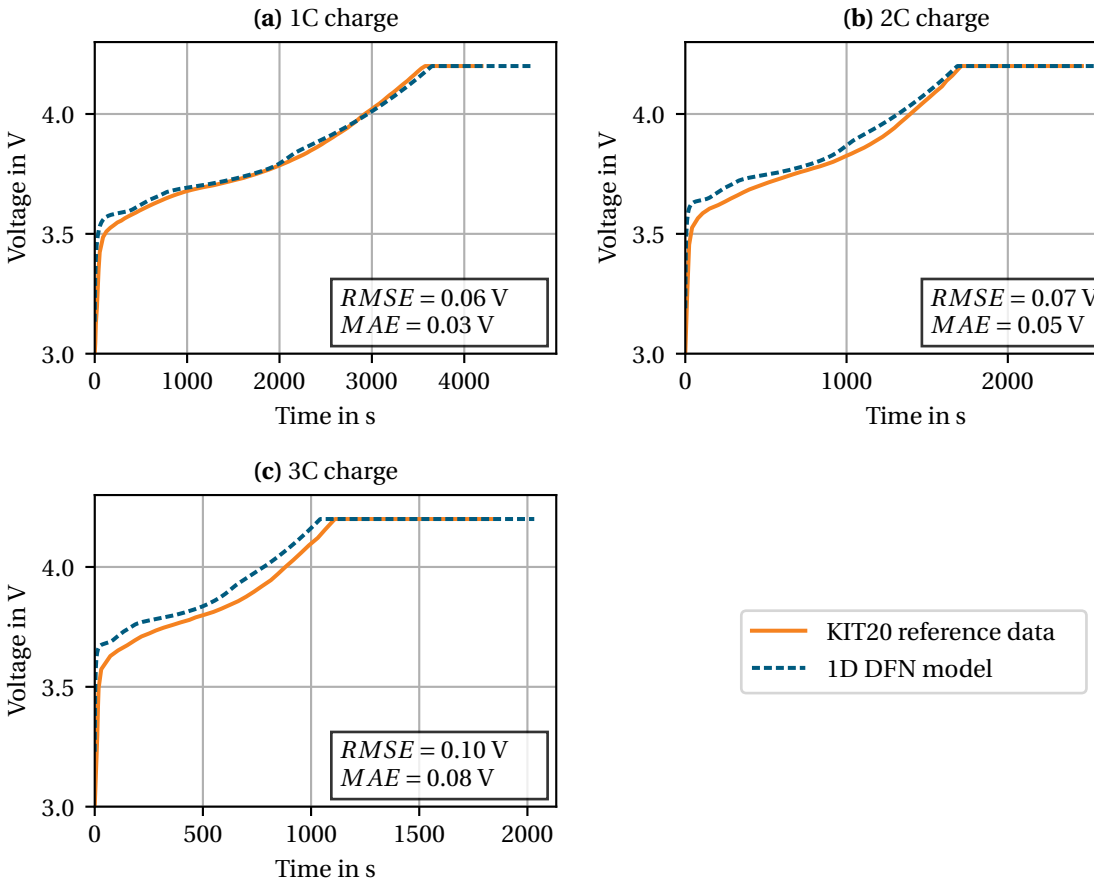

Fig. 3.4: Comparison of the charge behavior between the measurements of the KIT20 reference cell [139] and the 1D electrochemical-thermal simulation with the DFN model

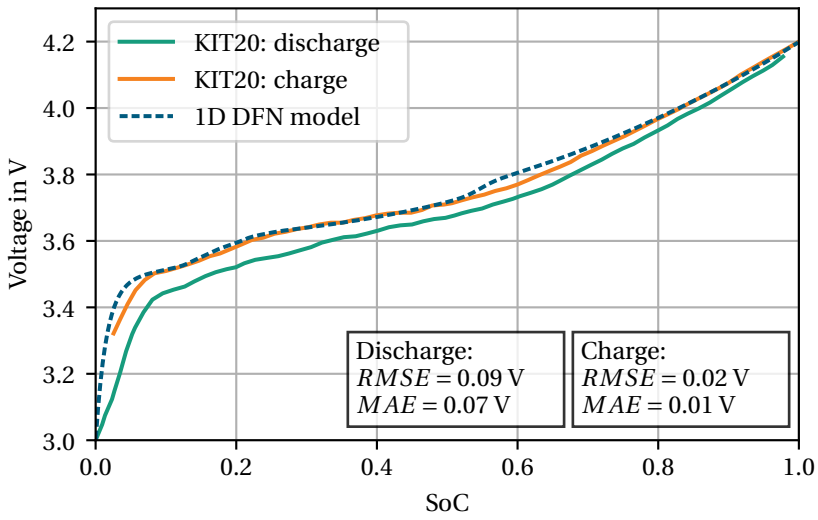

Fig. 3.5: Open circuit voltage of the KIT20 reference cell [139] compared to the 1D electrochemical-thermal simulation with the DFN model

charging process with an RMSE of 0.02 V and an MAE of 0.01 V. As charging is the load case of interest in this work, a good agreement during the charging is more important than during discharging.
Overall, the electrochemical parametrization of the DFN model is considered valid as all of the simulated results fit well with the reference data of the KIT20 cell.

3.3 Equivalent circuit cell model

In the following section, the second step of the modeling procedure – the setup of the equivalent-circuit model (ECM) – is described. Hereinafter, the 3D ECM is presented in detail as the 1D model may easily be derived from the 3D model: The 3D thermal domain becomes a lumped point mass and the parametrization of the ECM model parameters (U_{oc} and the RC elements) are identical, but only one system of equations is solved for the entire battery cell.
The 3D model is based on the MSMD approach [79] (see also section 2.3.1). To keep the 3D simulation as simple as possible, no other components of the battery cell – like the tabs or the pouch foil – are modeled but only the active material, so the electrode stack where the electrochemical reactions take place. All other components will be modeled later in the module model in a simplified manner and connected to the boundary surfaces of the 3D model. Figure 3.6 shows the cell domain of the 3D model. It is simply a rectangular cuboid as no other, more complex pouch cell formats are considered here. Two different tab configurations are modeled: A pouch cell, which has both tabs on one side (figure 3.6a) and a pouch cell, where the tabs are on opposite sides of the cell, which is called butterfly design (figure 3.6b). The one-sided tab design is used to compare the 3D ECM to the 1D DFN model, the butterfly tab design is used for the data generation for the CMM of the generic battery module model.

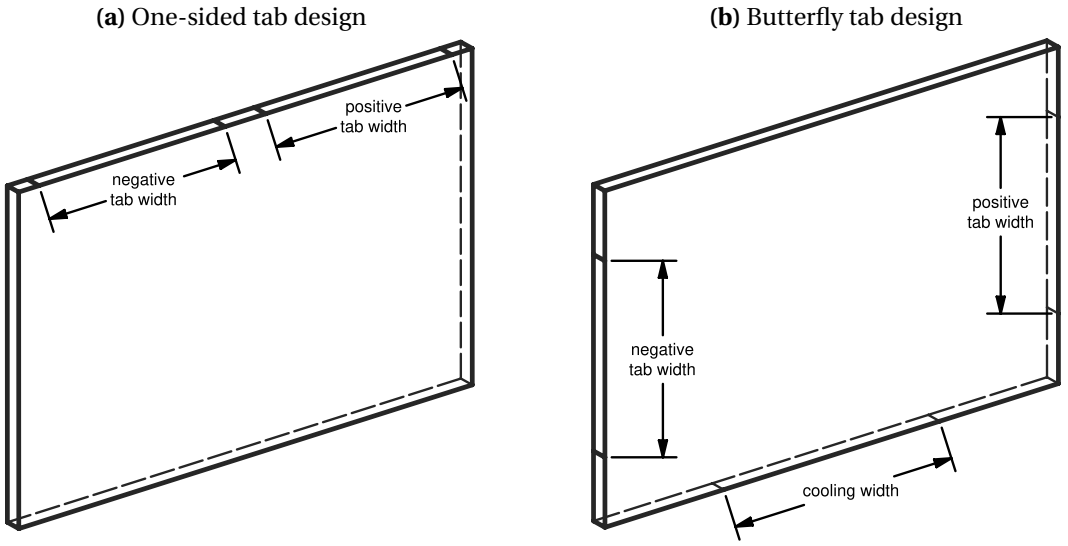

Fig. 3.6: Geometries of the 3D cell models

For the sake of simplicity, heat transfer to the environment is only considered on five surfaces:

- On the two large side surfaces to model the heat transfer between adjacent cells.
- On the tab surfaces to model heat transfer through the tabs.
- On the bottom of the cells, a cooling/heating surface is modeled to account for the typical bottom cooling/heating which is present in many BEVs.

The model is setup so that the dimensions of the cell (width, height, thickness), the width of tabs and the width of the bottom cooling surface may be varied flexibly (see figure 3.6). The electrical boundary conditions are applied on the tab surfaces.
The ECM is chosen to model the battery behavior on the electrode domain because of its higher computational speed compared to physics-based models [72]. This leads to computation times between 0.5 and 2 hours for one charging process with the 3D model. For the one-time data generation for the cell meta-model, this is considered to be an acceptable time range, but it would be unsuitable for the direct use in an optimization process of a module.
The 3D simulations are performed with the commercial CFD software package Ansys Fluent, Version 2023 R1 [143]. It provides an implementation of the MSMD model as well as the possibility to define user-specific ECMs.

ECM and parametrization

As outlined in section 2.3.1, there are numerous different ECM approaches that differ depending on the electrical elements which are used to model the behavior of the battery [74, 80, 82–84]. Here, the simplest possible model is used to decrease the computation time. As only charging scenarios with a constant current are investigated, the terms to model the dynamic cell behavior in equation 2.2 are neglected:

$$U = U_{\mathrm{oc}} - R_{\mathrm{s}} I - \underbrace{U_1 - U_2}_{=0} \tag{3.1}$$

Of the remaining model parameters, the open circuit voltage U_{oc} depends on the state of charge SoC and the temperature T. The resistance R_{s} depends on the state of charge SoC, the temperature T and the C-rate Cr. To account for that, U_{oc} and R_{s} are modeled as a map that is derived from the 1D DFN model. Even though the open circuit voltage U_{oc} does not depend on the C-rate Cr, it is still modeled with a map that depends on it. This enables the usage of identically mapping routines in the underlying simulation software:

$$U = U_{\mathrm{oc}}(|Cr|, T, SoC) - R_{\mathrm{s}}(|Cr|, T, SoC)\, I \tag{3.2}$$

The grid of the maps contains reference points at the following values for Cr, T and SoC, in-between these points a trilinear interpolation is performed:

$$|Cr| = \{1,\ 2,\ 3\} \text{ in } \mathrm{h}^{-1} \tag{3.3a}$$

$$T = \{-10,\ 0,\ 10,\ 20,\ 30,\ 40,\ 50\} \text{ in } ^\circ\mathrm{C} \tag{3.3b}$$

$$\begin{aligned} SoC = \{&0,\ 0.001,\ 0.002,\ 0.004,\ 0.006,\ 0.008,\ 0.01,\\ &0.015,\ 0.02,\ 0.03,\ 0.04,\ 0.05,\ 0.075,\ 0.1,\ ...,\ 1.0\} \end{aligned} \tag{3.3c}$$

The SoC grid is not spaced linearly, as for low SoC values U_{oc} and R_{s} change strongly and thus, a finer spacing is necessary. The same approach is used to determine the heat generation rate. Besides the open circuit voltage U_{oc}, also the entropic heating $\frac{\partial U}{\partial T}$ is modeled as a map depending on Cr, T and SoC with the same grid as in equation 3.3:

$$\dot{q} = i\left(U_{\mathrm{oc}}(|Cr|, T, SoC) - U - T\frac{\partial U}{\partial T}(|Cr|, T, SoC)\right) \tag{3.4}$$

All values of the maps for $U_{\mathrm{oc}}(|Cr|, T, SoC)$, $R_{\mathrm{s}}(|Cr|, T, SoC)$ and $\frac{\partial U}{\partial T}(|Cr|, T, SoC)$ can be found in the appendix in section A.1.

Validation

The validation of the 3D ECM compared to the 1D DFN model is performed with an exemplary charging simulation of the KIT20 cell. The geometry of the active material as shown in figure 3.6a is used. The cell dimensions are identical to the dimensions of the DFN model described in table 3.2 which results in an overall thickness of the active material of 7 mm. The width of both tabs is 86.2 mm. Adiabatic thermal boundary conditions are applied on all surfaces. The initial temperature is set to 25 °C and the C-rate to 2.5C. Intentionally, these values are chosen in-between the grid points of the maps to consider the influence of the interpolation.

The most relevant results of the simulations are shown in figure 3.7. Figure 3.7a compares the voltage over time for both models. With an RMSE and an MAE of 0.01 V, the results are in excellent agreement. The curve of the 3D ECM is slightly shifted towards smaller time values. An analysis of the time step size that was used for the time integration in the transient 3D simulation showed, that with smaller time steps, the deviation becomes also smaller. However, as the error measures are extremely low, the initially chosen time step size was kept to avoid increasing simulation times due to smaller time steps.

Also for the temperature, a good agreement between both models is observed with an RMSE and an MAE of 0.05 K, as depicted in 3.7b. In the remaining subfigures of figure 3.7, the volumetric heat generation rates are compared. Overall, the reversible (3.7c), the irreversible (3.7d) as well as the sum of both, the total heat generation rate (3.7e), agree well between both models. Noticeable deviations are mainly observed in the "peak" at the beginning of the charging process in the reversible and the total heat generation rate. These deviations originate from

the mapping approach and the linear interpolation between the grid points. However, the small deviations in the temperature development confirm, that the observed errors in the heat generation rates do not have a significant negative impact on the simulation results. Consequently, both modeling approaches fit well and the approximation of the DFN model with the mapping based ECM is considered valid for charging processes.

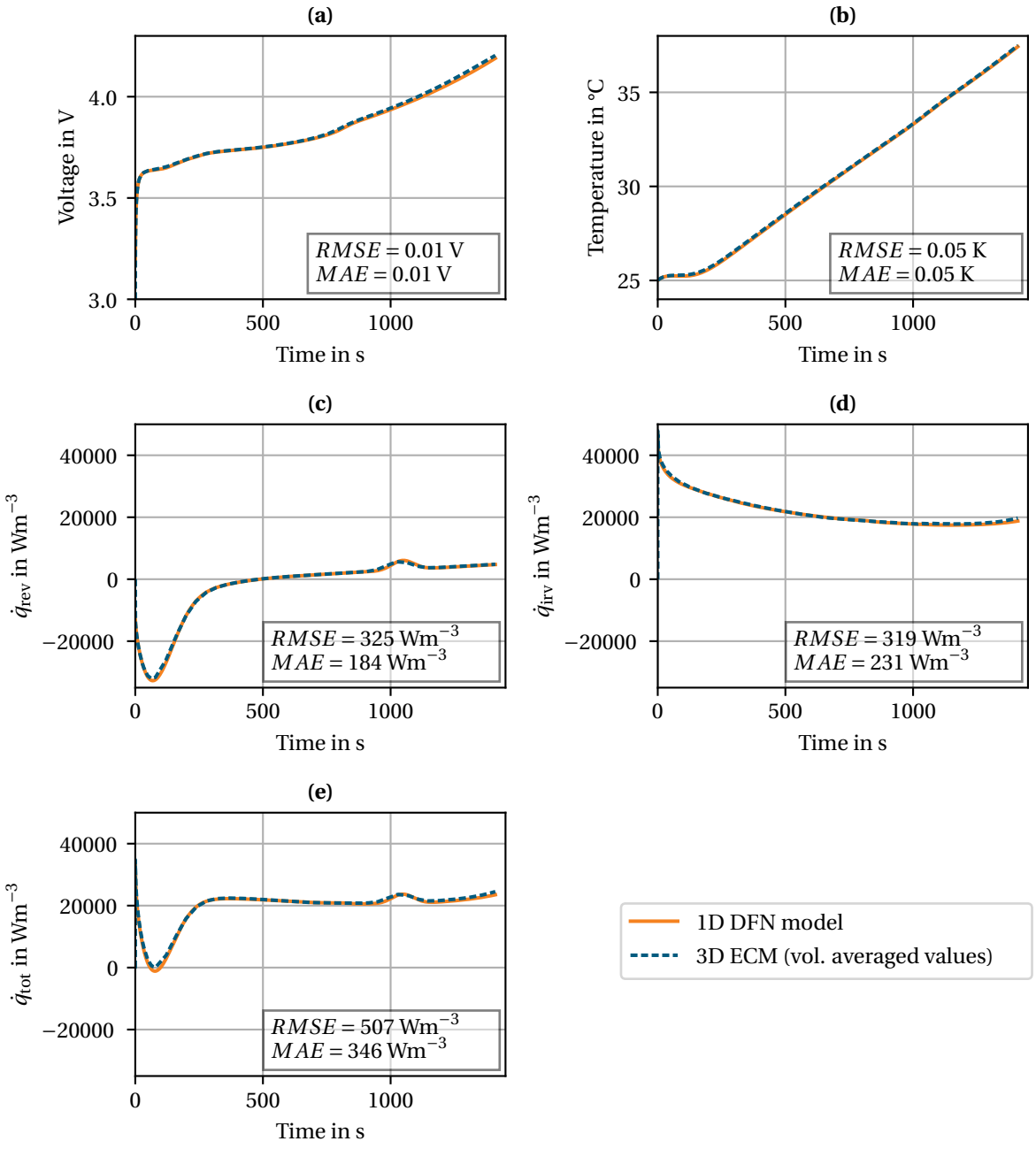

Fig. 3.7: Exemplary comparison of the 1D DFN model with the 3D ECM for a charging process with 2.5C starting at 25 °C. The voltage (a), the temperature (b), the reversible volumetric heat generation rate $\dot{q}_{rev}$ (c), the irreversible volumetric heat generation rate $\dot{q}_{irv}$ (d) and the total volumetric heat generation rate $\dot{q}_{tot}$ (e) are displayed over time. All shown quantities for the 3D ECM are volume averaged values.

3.4 Tab-cooled battery module prototype

3.4.1 Design of the module with tab cooling

A prototype module with a tab cooling was developed to experimentally investigate the tab cooling on module level and to validate the corresponding simulation model of the battery module. The experimental investigations as well as the design of the module have already been published in an own paper: [154]. The following three paragraphs are based on this paper.

Figure 3.8 shows the module design. It consists of twelve KIT20 cells that are connected in series (12s1p), which results in a module with the electrical properties given in table 3.3. As shown in figure 3.8a, the cells are held in place by plastic cell frames that are connected and compressed via four tension rods to the module end-plates.

The tab cooling is realized with thirteen cylindrical channels and three 3D-printed compression parts that hold the channels in place, guide the tabs for the correct electrical connection and compress the tabs for the electrical contacting. The cooling channels are made of aluminum. In the area, where they are in contact with the tabs for the cooling, they are coated with a 78 µm thick polyimide adhesive tape [154–156], visible as the orange material in figure 3.8b next to the tabs. Having a thermal conductivity of 0.46 $\mathrm{W\,m^{-1}\,K^{-1}}$, the polyimide tape

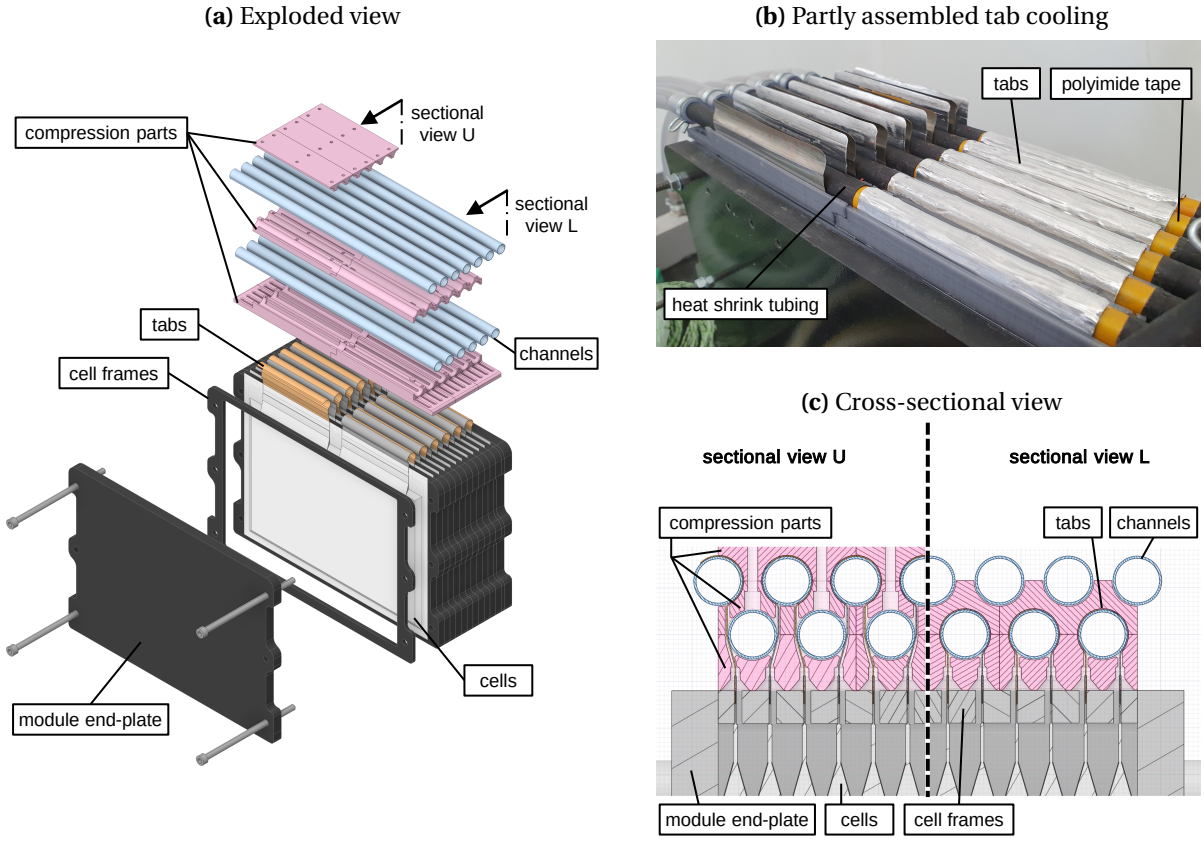

Fig. 3.8: Design of the module prototype (the pictures in (a) and (c) are taken from [154])

offers approximately twice the thermal conductivity of similar plastic materials [157]. The dielectric strength is 89.7 $kV mm^{-1}$, which leads to a sufficient electrical insulation for the application in a battery module. A thicker heat-shrink tubing, the black material visible in figure 3.8b, covers the rest of the aluminum channels for electrical insulation.
The cross-sectional view in figure 3.8c depicts the bending of the tabs around the cooling channels. From each cell, one tab is cooled by the upper cooling channels (figure 3.8c left, "sectional view U") and one tab is cooled by the lower ones (figure 3.8c right, "sectional view L"). This design was chosen to increase the safety during the tests. With it, each tab is only connected to one cooling channel and thus, the tabs of one cell cannot be short-circuited directly with one aluminum channel. In case of a damage to the electrically insulating coating, which could occur for example during the assembly by hand, the risk of a short circuit and consequently a thermal runaway is minimized.

Tab. 3.3: Electrical properties of the prototype module [154]

Parameter	Value
Nominal capacity	20 A h
Cells in series	12
Cells in parallel	1
Max. operating voltage	50.4 V
Nominal voltage	44.4 V
Min. operating voltage	36.0 V

3.4.2 Experimental setup of the tab cooling tests

The following description of the experimental setup of the tab cooling tests is again based on the own publication: [154].
Figure 3.9a shows the assembled prototype module installed on the test bench. On the left and the right side of the picture, the cooling hoses attached to the channels are visible. The thick orange cables in the front and the back of the module are for the electrical connection. The various smaller cables stem form sensors measuring the voltages between every cell as well as from thermocouples (TCs) to measure the temperature at different locations. Five TCs each are placed between cells 1 and 2, 6 and 7 (the middle of the module) and 11 and 12. In figure 3.9b, the locations of these TCs on a cell are depicted: One TC is placed in the middle of the cell surface and the other four TCs are close to the corners of the surface. Furthermore, at the same cells, TCs are mounted at the top of the tabs to measure the tab temperature close to the cooling channels.
Two different types of cooling tests are performed:

1. *Heat-up-cool-down test*: Without an electrical load, the module is heated up and cooled down with the tab cooling only. Both the modules and the cooling fluids initial temperature is 12 °C. Then, the fluid temperature is increased to 45 °C and the module is

(a) Prototype module on the test bench

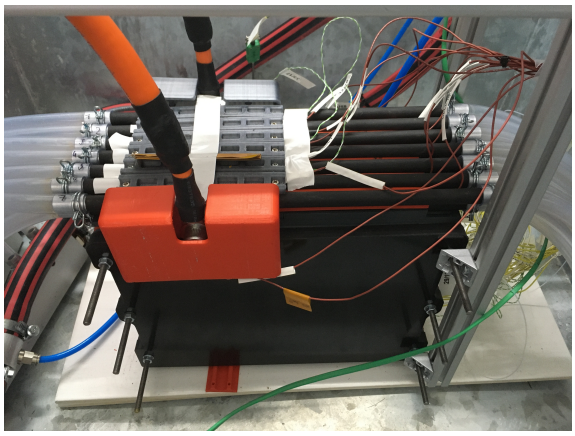

(b) Thermocouple locations

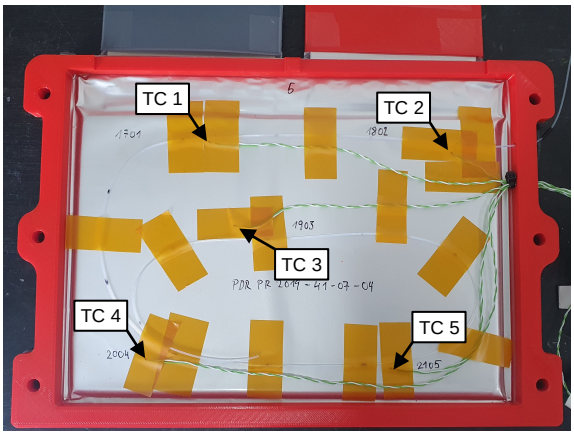

Fig. 3.9: Experimental setup of the prototype module (picture (a) is taken from [154])

heated up for approximately 2 h. Afterwards, the fluid temperature is decreased to 15 °C and the module is cooled down for approximately 2 h.

2. *2C charging test*: Starting from an initial SoC of approximately 2.5 %, the module is charged with a constant C-rate of 2C until the first cell reaches a voltage of 4.1 V. This test is carried out with an activated and a deactivated tab cooling. In case the cooling is active, it operates with a fluid temperature of 17 °C. The initial module temperature is equal to the ambient temperature (with cooling 18 °C, without cooling 19 °C).

3.4.3 Simulation model

The corresponding simulation model to the previously described battery module prototype is shown in figures 3.10 and 3.11. Figure 3.10 describes the entire module model and figure 3.11 the modeling of a single battery cell of the module. The simulation model consists of a 1D thermal network that is coupled to a 1D electrical and a 1D fluid network. As the module prototype is symmetric, only half of the module – six battery cells – is modeled and a symmetry boundary condition is applied. The entire model was built up and simulated in the commercial simulation software GT SUITE, Version 2023 [158].

Thermal and fluid network

The red lines and elements in both figures symbolize the thermal network which consists of thermal resistances (red boxes) and thermal point masses (red dots) to model the single components.
As figure 3.10 shows, the battery cells of the module are thermally connected to each other with a thermal resistance R_{airgap} that represents the influence of the pouch bag foil and the air gap in-between the cells:

$$R_{\mathrm{airgap}} = \frac{2\,t_{\mathrm{bag}}}{\lambda_{\mathrm{bag}}\,w_{\mathrm{av}}\,h_{\mathrm{av}}} + \frac{t_{\mathrm{air}}}{\lambda_{\mathrm{air}}\,w_{\mathrm{av}}\,h_{\mathrm{av}}} \tag{3.5}$$

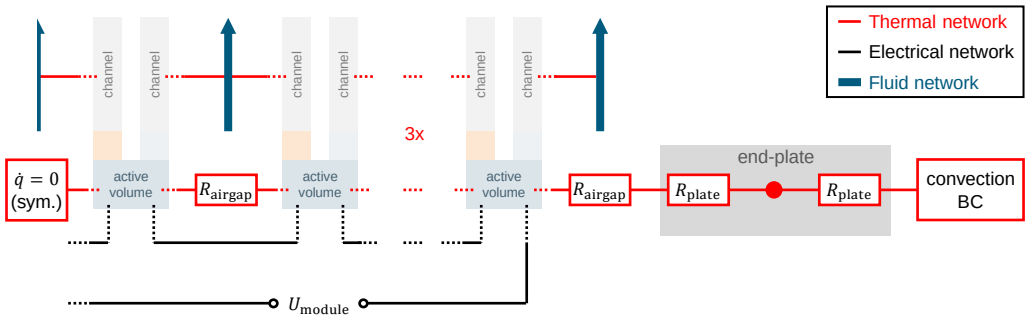

Fig. 3.10: Simulation model of the tab-cooled battery module prototype. The modeling of the single battery cells is depicted in detail in figure 3.11.

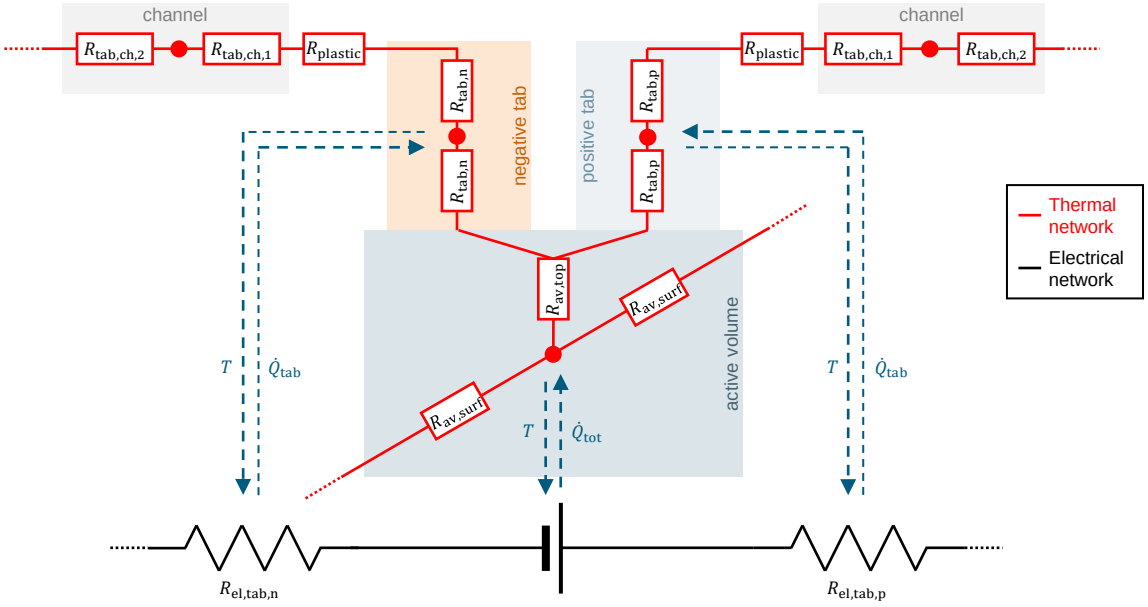

Fig. 3.11: Simulation model of a single battery cell in the battery module prototype including the tab cooling channels

The left hand side of figure 3.10 represents the middle of the module where a symmetry boundary condition $\dot{q} = 0$ is applied. On the right hand side, the end-plate is modeled consisting of a thermal mass C_{plate} and two thermal resistances R_{plate}:

$$C_{\text{plate}} = c_{\text{p,plate}} \rho_{\text{plate}} \left(w_{\text{av}} h_{\text{av}} t_{\text{plate}} \right) \tag{3.6a}$$

$$R_{\text{plate}} = \frac{0.5\, t_{\text{plate}}}{\lambda_{\text{plate}} w_{\text{av}} h_{\text{av}}} \tag{3.6b}$$

To the outer side of the end-plate, a convection boundary condition to the environment is applied:

$$\dot{q} = \alpha_{\text{env}} \left(T_{\text{plate,o}} - T_{\text{env}} \right) \quad \text{with} \quad \alpha_{\text{env}} = 10\,\text{W}\,\text{m}^{-2}\,\text{K}^{-1} \tag{3.7}$$

The channels of the cooling system are thermally connected to a fluid network, where each fluid volume is modeled as a 1D finite volume, discretized with 10 elements. The volume flow of the cooling fluid is distributed equally between all of the channels. The thermal coupling occurs via a heat transfer coefficient α_{fluid} that is based on the Nusselt number [157, 158]:

$$\alpha_{\text{fluid}} = \frac{Nu \lambda_{\text{fluid}}}{d_{\text{i}}} \quad \text{with} \quad Nu = 3.66 \quad \text{(laminar flow)} \tag{3.8}$$

As can be seen from figure 3.11, the channels are modeled with a thermal mass $C_{\text{tab,ch}}$ and two thermal resistances $R_{\text{tab,ch,1}}$ and $R_{\text{tab,ch,2}}$:

$$C_{\text{tab,ch}} = c_{\text{p,ch}} \rho_{\text{ch}} \left(0.25 (d_{\text{o}} - d_{\text{i}})^2 w_{\text{av}} \right) \tag{3.9a}$$

$$R_{\text{tab,ch,1}} = \frac{0.25 (d_{\text{o}} - d_{\text{i}})}{0.25 \pi d_{\text{o}} w_{\text{tab,n/p}} \lambda_{\text{ch}}} \tag{3.9b}$$

$$R_{\text{tab,ch,2}} = \frac{0.25 (d_{\text{o}} - d_{\text{i}})}{0.5 \pi d_{\text{i}} w_{\text{tab,n/p}} \lambda_{\text{ch}}} \tag{3.9c}$$

The plastic tape between the channels and the tab is solely modeled as a thermal resistance R_{plastic} and its thermal mass is neglected:

$$R_{\text{plastic}} = \frac{t_{\text{plastic}}}{0.25 \pi d_{\text{o}} w_{\text{tab,n/p}} \lambda_{\text{plastic}}} \tag{3.10}$$

The tabs are again modeled with a thermal mass $C_{\text{tab,n/p}}$ and two thermal resistances $R_{\text{tab,n/p}}$

$$C_{\text{tab,n}} = c_{\text{p,tab,n}} \rho_{\text{tab,n}} \left(w_{\text{tab,n}} h_{\text{tab,n}} t_{\text{tab,n}} \right) \tag{3.11a}$$

$$C_{\text{tab,p}} = c_{\text{p,tab,p}} \rho_{\text{tab,p}} \left(w_{\text{tab,p}} h_{\text{tab,p}} t_{\text{tab,p}} \right) \tag{3.11b}$$

$$R_{\text{tab,n}} = \frac{0.5 h_{\text{tab,n}}}{\lambda_{\text{tab,n}} w_{\text{tab,n}} t_{\text{tab,n}}} \tag{3.11c}$$

$$R_{\text{tab,p}} = \frac{0.5 h_{\text{tab,p}}}{\lambda_{\text{tab,p}} w_{\text{tab,p}} t_{\text{tab,p}}} \tag{3.11d}$$

The active volume of the cells is modeled with a thermal mass C_{av} and three thermal resistances, two modeling the side surfaces of the active volume ($R_{\mathrm{av,surf}}$) and one modeling the thermal resistance to the tabs ($R_{\mathrm{av,top}}$):

$$C_{\mathrm{av}} = c_{\mathrm{p,av}} \rho_{\mathrm{av}} \left(w_{\mathrm{av}} h_{\mathrm{av}} t_{\mathrm{av}} \right) \tag{3.12a}$$

$$R_{\mathrm{av,surf}} = \frac{0.5 t_{\mathrm{av}}}{\lambda_{\mathrm{av},\perp} w_{\mathrm{av}} h_{\mathrm{av}}} \tag{3.12b}$$

$$R_{\mathrm{av,top}} = \frac{0.5 h_{\mathrm{av}}}{\lambda_{\mathrm{av},\parallel} w_{\mathrm{av}} t_{\mathrm{av}}} \tag{3.12c}$$

The thermal network is coupled to the electrical network as indicated by the dashed blue lines in figure 3.11. The losses due to Ohmic heating in the tabs are applied to the tab thermal masses and the heat generation in the active volume – modeled by the ECM – is applied to the active volume thermal mass. In return, the temperatures of the the components are returned to the electrical network to consider the temperature dependence of the electrical properties.

Electrical network

The electrical network is symbolized by the black lines and electronic symbols in figures 3.10 and 3.11. All of the battery cells are connected in series, which results in the overall module voltage of U_{module}, displayed in figure 3.10. The voltage of the single battery cells and the heat generation within the active volume is calculated according to the 1D ECM described in section 3.3, equations 3.2 and 3.4. An ideal electrical connection between the single cells is assumed and the electrical resistances $R_{\mathrm{el,tab,n}}$ and $R_{\mathrm{el,tab,p}}$ denoted in figure 3.11 are solely used to calculate the heat generated in the tabs:

$$\begin{aligned} \dot{Q}_{\mathrm{tab}} &= I^2 R_{\mathrm{el,tab,n/p}} \\ &= I^2 \frac{1}{\sigma_{\mathrm{tab,n/p}}} \frac{h_{\mathrm{tab,n/p}}}{w_{\mathrm{tab,n/p}} t_{\mathrm{tab,n/p}}} \end{aligned} \tag{3.13}$$

All of the input and model parameters used in the equations above are described and listed in table 3.4.

Load case

With the simulation model, the 2C charging test described in section 3.4.2 is computed. The initial and load conditions are given in table 3.5. To model the charging test with a deactivated cooling system, the thermal conductivity of the plastic material $\lambda_{\mathrm{plastic}}$ was set to a sufficiently small value to deactivate the heat transfer from the tab to the cooling system ($\lambda_{\mathrm{plastic}} = 1 \times 10^{-7}\,\mathrm{W\,m^{-1}\,K^{-1}}$).

Tab. 3.4: Geometry and material parameters of the battery module prototype simulation model

Part	Parameter	Symbol	Value
Active volume	Width	w_{av}	210 mm
	Height	h_{av}	137 mm
	Thickness	t_{av}	7 mm
	Thermal conductivity	$\lambda_{\mathrm{av},\parallel}$, $\lambda_{\mathrm{av},\perp}$	see table 3.1
	Specific heat capacity	$c_{\mathrm{p,av}}$	see table 3.1
	Density	ρ_{av}	$2420\,\mathrm{kg\,m^{-3}}$
Negative tab (Copper)	Width	$w_{\mathrm{tab,n}}$	86.2 mm
	Height	$h_{\mathrm{tab,n}}$	40 mm
	Thickness	$t_{\mathrm{tab,n}}$	0.2 mm
	Thermal conductivity	$\lambda_{\mathrm{tab,n}}$	see table A.10
	Specific heat capacity	$c_{\mathrm{p,tab,n}}$	see table A.10
	Density	$\rho_{\mathrm{tab,n}}$	$8933\,\mathrm{kg\,m^{-3}}$
	Electrical conductivity	$\sigma_{\mathrm{tab,n}}$	$5.8\times10^{7}\,\mathrm{S\,m^{-1}}$
Positive tab (Aluminum)	Width	$w_{\mathrm{tab,p}}$	86.2 mm
	Height	$h_{\mathrm{tab,p}}$	40 mm
	Thickness	$t_{\mathrm{tab,p}}$	0.2 mm
	Thermal conductivity	$\lambda_{\mathrm{tab,p}}$	see table A.11
	Specific heat capacity	$c_{\mathrm{p,tab,p}}$	see table A.11
	Density	$\rho_{\mathrm{tab,p}}$	$2702\,\mathrm{kg\,m^{-3}}$
	Electrical conductivity	$\sigma_{\mathrm{tab,p}}$	$3.538\times10^{7}\,\mathrm{S\,m^{-1}}$
Plastic tape (Polyimide)	Thickness	t_{plastic}	0.078 mm
	Thermal conductivity	$\lambda_{\mathrm{plastic}}$	$0.46\,\mathrm{W\,m^{-1}\,K^{-1}}$
Tab channel (Aluminum)	Inner diameter	d_{i}	9.5 mm
	Outer diameter	d_{o}	10.5 mm
	Thermal conductivity	λ_{ch}	see table A.11
	Specific heat capacity	$c_{\mathrm{p,ch}}$	see table A.11
	Density	ρ_{ch}	$2702\,\mathrm{kg\,m^{-3}}$
Airgap	Thickness pouch bag	t_{bag}	0.2 mm
	Thickness air in gap	t_{air}	0.25 mm
	Th. cond. pouch bag	λ_{bag}	$0.25\,\mathrm{W\,m^{-1}\,K^{-1}}$
	Th. cond. air in gap	λ_{air}	$0.026\,\mathrm{W\,m^{-1}\,K^{-1}}$
End-plate (PA 6.6)	Thickness	t_{plate}	10 mm
	Thermal conductivity	λ_{plate}	$0.33\,\mathrm{W\,m^{-1}\,K^{-1}}$
	Specific heat capacity	$c_{\mathrm{p,plate}}$	see table A.12
	Density	ρ_{plate}	$1145\,\mathrm{kg\,m^{-3}}$
Cooling fluid (Water-Glycol (50/50))	Dynamic viscosity	μ_{fluid}	see table A.14
	Thermal conductivity	λ_{fluid}	table A.14
	Specific heat capacity	$c_{\mathrm{p,fluid}}$	see equation A.1
	Density	ρ_{fluid}	see equation A.2

Tab. 3.5: Initial parameters and load conditions of the battery module prototype simulation model for the simulation of the 2C charging test

Parameter	Symbol	no cooling	cooling
Cell nominal capacity	Q_{nom}	20 Ah	
C-rate	Cr	$-2\,\mathrm{h}^{-1}$	
Initial SoC	SoC_{init}	2.5 %	
Max. cell voltage	U_{end}	4.11 V	
Initial temperature components	T_{init}	19 °C	18 °C
Temperature environment	T_{env}	19 °C	18 °C
Initial temperature fluid	$T_{\mathrm{init,fluid}}$	19 °C	17 °C
Volume flow rate cooling fluid	$\dot{V}_{\mathrm{fluid}}$	30/13 L min^{-1}	
Outlet pressure	p_{out}	1 bar	

3.5 Generic battery module model

3.5.1 Generic design

The general design idea of the generic battery module model is shown in figure 3.12. As the model serves the purpose, to find the optimal thermal cell design, the dimensions displayed in the picture are only exemplary. All of the dimensions of the model will be varied but the general arrangement of the components shown in figure 3.12 will stay identical.
The generic module consists of six pouch cells which are all connected in series (6s1p). In contrast to the battery module prototype introduced in the previous section 3.4, pouch cells with a butterfly tab design were chosen. Firstly, that tab design is used more frequently in

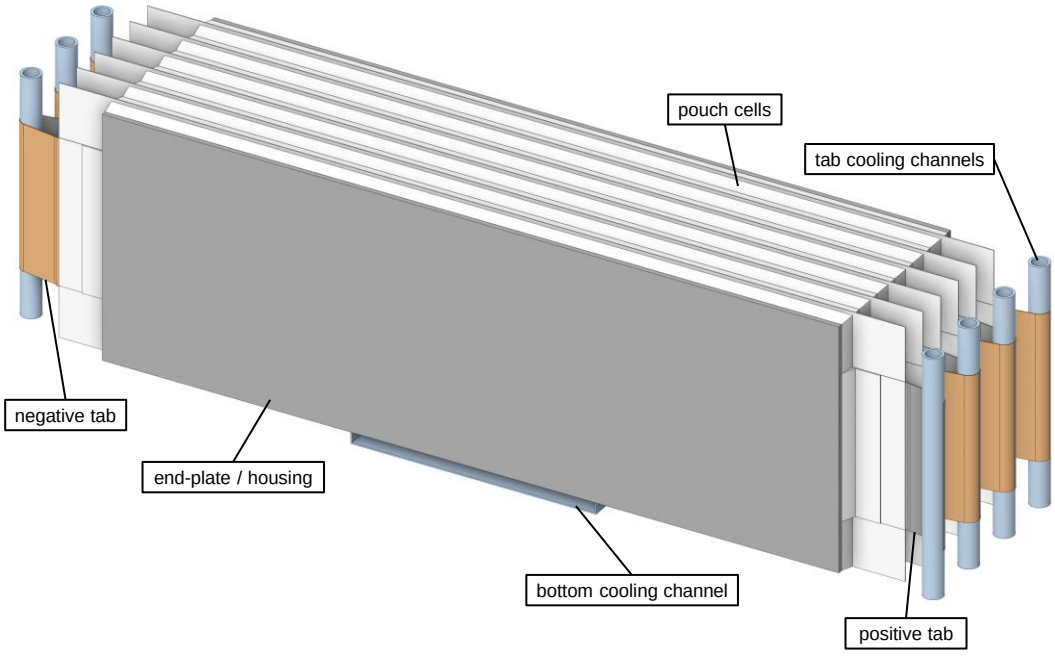

Fig. 3.12: Design of the generic battery module model

state of the art battery electric vehicles, secondly, the tests with the self-developed battery module prototype showed, that the realization of a tab cooling system is more difficult with the one-sided tab design, as there is less design space for the electrical connection of the cells as well as for the integration of the tab cooling channels. Thus, using a butterfly tab design is the more general and application-oriented approach.

The model only includes the most important parts for the thermal modeling of a module so that the major thermal effects are considered but at the same time, the model stays as simple and general as possible. Like in the previously presented battery module prototype, the tab cooling channels are made from aluminum and the tabs are bent around the round channels to electrically contact the cells with each other. Again, a thin, thermally conductive but electrically insulation plastic layer is assumed between the channels and the tab. Besides the tab cooling channels, also an aluminum bottom cooling channel is included in the model to be able to compare the different cooling approaches. It is placed in the middle of the thin cell side which is called for the sake of simplicity bottom of the cell. Again, between the bottom cooling channel and the cells a thin plastic layer is assumed. Theoretically, an electrical insulation is not necessary here, but many cooling systems include such an insulating layer for safety purposes [6].

On the large side surfaces of the module, thin aluminum end-plates are modeled to account for the heat that is dissipated on the cell sides of the first and the last cell. Other module housing structures are not considered as their contribution to the thermal behavior is assumed to be small. Moreover, a generic design of such structures is difficult to describe as it strongly depends on the integration of the module in the pack.

3.5.2 Simulation model

Figures 3.13 and 3.14 show the corresponding simulation model of the generic battery module. The model of the entire module is displayed in figure 3.13 and the model of a single battery cell is shown in figure 3.14. The modeling approach is very similar to the model of the battery module prototype. Again, a 1D thermal network is coupled to a 1D electrical and a 1D fluid network. Additionally, as mentioned in section 3.1, a cell meta-model (CMM) is applied as a post-processing step to determine the temperature difference within the cell after a charging process. The CMM is described in detail in the subsequent section 3.5.3. It is implemented using the programming language Python and afterwards integrated in the simulation model of the entire battery module which was again built up and simulated in the commercial simulation software GT SUITE, Version 2023 [158].

Again, the red lines and elements in figures 3.13 and 3.14 depict the thermal network consisting of thermal resistances (red boxes) and thermal point masses (red dots) to model all of the components. As the modeling approach is very similar to the model of the battery module prototype, in the following, only formulas are given if they differ from the previously described model.

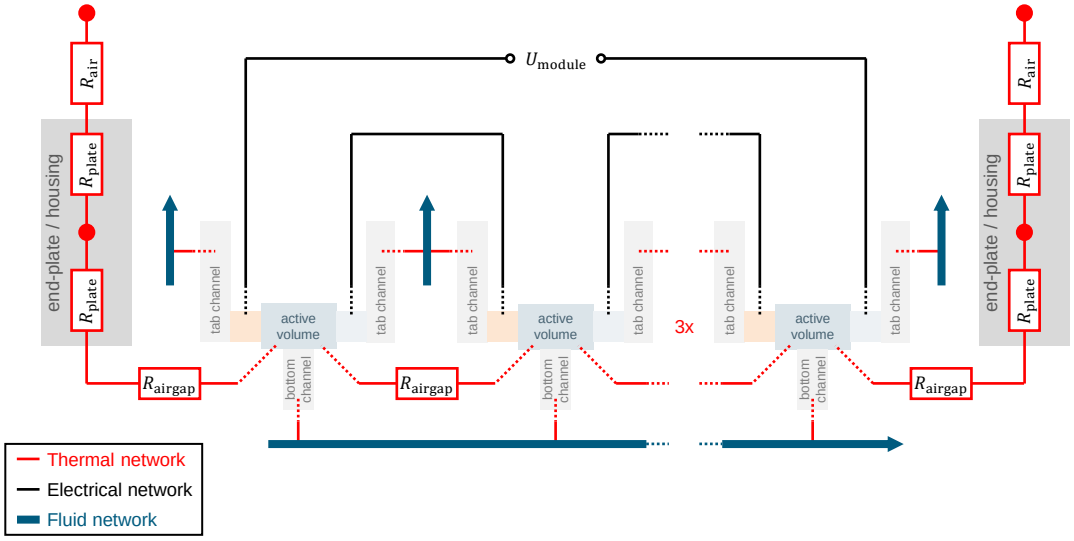

Fig. 3.13: Simulation model of the generic battery module. The modeling of the single battery cells is depicted in detail in figure 3.14.

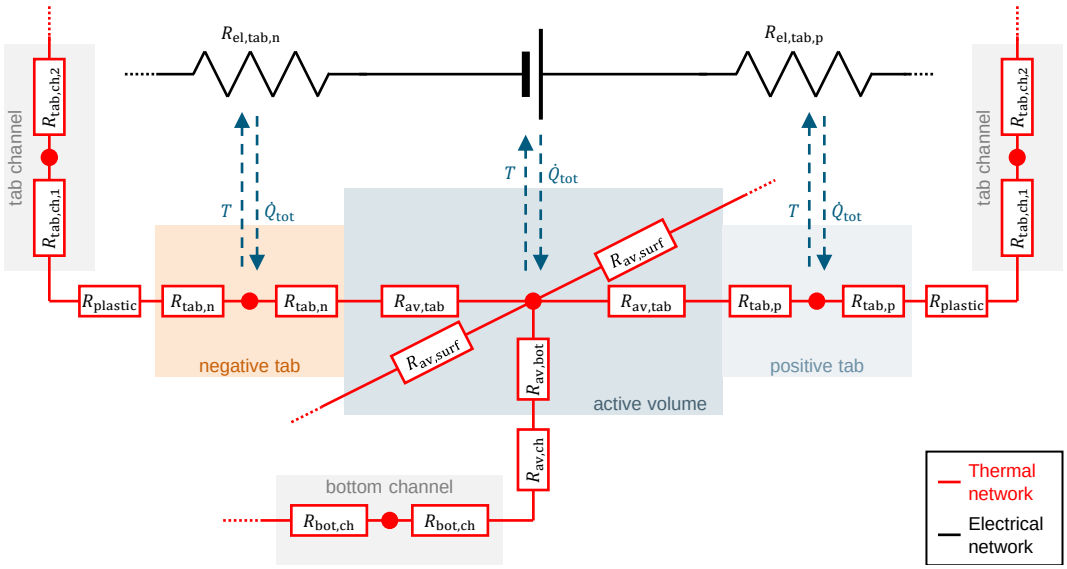

Fig. 3.14: Simulation model of a single battery cell in the generic battery module including the tab cooling channels and the bottom cooling channel

The thermal connection between the battery cells is modeled identically to the battery module prototype model with a thermal resistance R_{airgap}, representing the influence of the pouch bag foil and the air gap in-between the cells. At the end of the module, indicated in figure 3.13 on the left and the right side, there are the end-plates consisting of a thermal mass C_{plate} and two thermal resistances R_{plate}. In the generic module, aluminum is chosen as the material of the end-plates.

In contrast to the previous model, there is not a convection boundary condition on the outer side of the end-plates but a conduction boundary condition to a defined air volume. This is assumed, as in a real battery pack the modules are arranged closely together and there is much less space around the modules compared to the test bench setup. Consequently, it is very unlikely that convective flow conditions are established. Instead, a small air volume is placed in the generic battery module model next to the end-plates having a thermal mass C_{air} and connected with a thermal resistance R_{air} to the end-plates:

$$C_{\text{air}} = c_{\text{p,air}} \rho_{\text{air}} \left(w_{\text{av}} h_{\text{av}} t_{\text{air,o}} \right) \tag{3.14a}$$

$$R_{\text{air}} = \frac{0.5\, t_{\text{air,o}}}{\lambda_{\text{air,o}}\, w_{\text{av}} h_{\text{av}}} \tag{3.14b}$$

The tab cooling channels are thermally connected to the fluid network in the same way as in the battery module prototype model. Additionally, there is a thermal connection between the bottom cooling channel and the fluid network of the bottom cooling channel. The fluid volume is modeled as a 1D finite volume with a rectangular cross-sectional area. It is discretized with 30 elements and the thermal coupling occurs again with a heat transfer coefficient α_{fluid} that is based on the Nusselt number [157, 158]. The volume flow is distributed between all of the channels in such a way, that the average flow velocity is identical and thus, identical flow conditions in all of the channels prevail. As depicted in figure 3.14, the bottom cooling channel is modeled with a thermal mass $C_{\text{bot,ch}}$ and two thermal resistances $R_{\text{bot,ch}}$:

$$C_{\text{bot,ch}} = c_{\text{p,ch}} \rho_{\text{ch}} \left(\left(w_{\text{ch}} h_{\text{ch}} - \left(w_{\text{ch}} - 2\, t_{\text{ch}} \right) \left(h_{\text{ch}} - 2\, t_{\text{ch}} \right) \right) \left(t_{\text{av}} + 2\, t_{\text{bag}} + t_{\text{air}} \right) \right) \tag{3.15a}$$

$$R_{\text{bot,ch}} = \frac{0.5\, t_{\text{ch}}}{\lambda_{\text{ch}}\, w_{\text{ch}}\, t_{\text{av}}} \tag{3.15b}$$

The connection between the bottom cooling channel and the active volume is modeled with the thermal resistance $R_{\text{av,ch}}$. It includes the thermally conductive plastic tape between the channel and the cell, as well as the cell's components on the bottom side. Figure 3.15 shows an X-ray photo of the side of a pouch cell from Larsson et al. [159] (similar photos can be found in [160–162]). In the photo on the left hand side, the transition from the active volume to the outside of the cell can be seen. It is clearly visible that the "homogeneous" active volume does not extend until the side of the cell where the pouch bag foil marks the end of the cell. There is a transitional area in-between where the anodes are larger than the cathodes and remaining volume is filled with electrolyte. Also the anodes do not extend until the beginning of the pouch bag foil but there seems to be a small electrolyte film in-between.

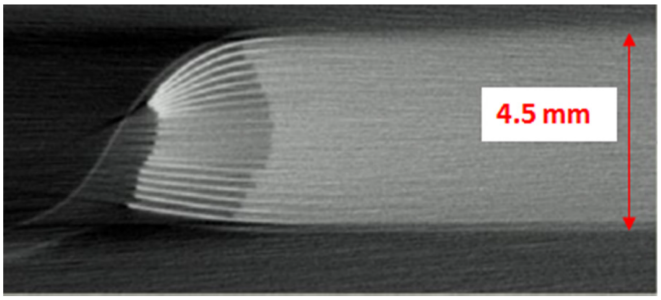

Fig. 3.15: X-ray photo of the side of a pouch cell, taken from: [159]

Consequently, the thermal resistance $R_{\mathrm{av,ch}}$ was modeled as a series connection of four thermal resistances: The thermal resistance R_{trans} of the "transition area" where the anodes are larger than the cathodes, a thermal resistance R_{elyte} of the electrolyte film, the thermal resistance $R_{\mathrm{bag,ch}}$ of the pouch bag foil and the thermal resistance $R_{\mathrm{plastic,ch}}$ of the plastic tape. This results in:

$$R_{\mathrm{av,ch}} = R_{\mathrm{trans}} + R_{\mathrm{elyte}} + R_{\mathrm{bag}} + R_{\mathrm{plastic}} \tag{3.16}$$

with:

$$R_{\mathrm{trans}} = \frac{t_{\mathrm{trans}}}{\left(0.5\lambda_{\parallel} + 0.5\lambda_{\mathrm{elyte}}\right) w_{\mathrm{ch}}\, t_{\mathrm{av}}} \tag{3.17a}$$

$$R_{\mathrm{elyte}} = \frac{t_{\mathrm{elyte}}}{\lambda_{\mathrm{elyte}}\, w_{\mathrm{ch}}\, t_{\mathrm{av}}} \tag{3.17b}$$

$$R_{\mathrm{bag,ch}} = \frac{t_{\mathrm{bag}}}{\lambda_{\mathrm{bag}}\, w_{\mathrm{ch}}\, t_{\mathrm{av}}} \tag{3.17c}$$

$$R_{\mathrm{plastic,ch}} = \frac{t_{\mathrm{plastic}}}{\lambda_{\mathrm{plastic}}\, w_{\mathrm{ch}}\, t_{\mathrm{av}}} \tag{3.17d}$$

The tab cooling channels are modeled identically to the battery module prototype model with the thermal mass $C_{\mathrm{tab,ch}}$ and the thermal resistances $R_{\mathrm{tab,ch,1}}$ and $R_{\mathrm{tab,ch,2}}$. Also the thermal resistance of the plastic R_{plastic} is identical as well as the thermal masses $C_{\mathrm{tab,n}}$ and $C_{\mathrm{tab,p}}$ and resistances $R_{\mathrm{tab,n}}$ and $R_{\mathrm{tab,p}}$ of the tabs. The same holds for the thermal mass of the active volume C_{av} and the thermal resistance of the active volume to the large side surfaces $R_{\mathrm{av,surf}}$. The thermal resistances $R_{\mathrm{av,tab}}$ within the active volume to the tabs changes due to the butterfly design of the cell and the thermal resistance $R_{\mathrm{av,bot}}$ of the active volume towards its bottom is newly introduced:

$$R_{\mathrm{av,tab}} = \frac{0.5\, w_{\mathrm{av}}}{\lambda_{\mathrm{av},\parallel}\, h_{\mathrm{av}}\, t_{\mathrm{av}}} \tag{3.18a}$$

$$R_{\mathrm{av,bot}} = \frac{0.5\, h_{\mathrm{av}}}{\lambda_{\mathrm{av},\parallel}\, w_{\mathrm{av}}\, t_{\mathrm{av}}} \tag{3.18b}$$

The coupling between the thermal network and the electrical network (dashed blue lines in figure 3.14) is done in the same manner as in the battery module prototype model. The

same holds for the modeling of the electrical network itself, indicated by the black lines and electronic symbols in figures 3.13 and 3.14. The cell chemistry is assumed to be identical to the KIT20 cell so that all parameters of the ECM stay the same. The nominal capacity Q_{nom} is always scaled according to the dimensions of the cell keeping the volumetric energy density constant all the time.

All of the fixed geometry and material parameters used in the equations above that differ from the parameters of the battery module prototype model (see table 3.4) are listed in table 3.6. The parameters that will be varied and do consequently not have a fixed value are described and listed in table 3.7. These are the major geometric parameters of the battery cell and the cooling system that have an influence on the thermal design. In section 3.5.4, where the optimization procedure is described, the exemplary load cases and the value ranges of the variable parameters are described in detail.

Tab. 3.6: Geometry and material parameters of the generic battery module model that are fixed and differ from the battery module prototype model

Part	Parameter	Symbol	Value
Bottom channel (Aluminum)	Height	h_{ch}	6 mm
	Wall thickness	t_{ch}	0.5 mm
Air volume	Thickness air volume	t_{air}	5 mm
	Thermal conductivity	$\lambda_{\mathrm{air,o}}$	see table A.13
	Specific heat capacity	$c_{\mathrm{p,air}}$	see table A.13
	Density	ρ_{air}	see table A.13
End-plate (Aluminum)	Thickness	t_{plate}	2 mm
	Thermal conductivity	λ_{plate}	see table A.11
	Specific heat capacity	$c_{\mathrm{p,plate}}$	see table A.11
	Density	ρ_{plate}	$2702\,\mathrm{kg\,m^{-3}}$
Interface active volume to bottom cooling channel	Thickness transition area	t_{trans}	1 mm
	Thickness electrolyte layer	t_{elyte}	0.2 mm
	Th. cond. electrolyte ([141])	λ_{elyte}	$0.18\,\mathrm{W\,m^{-1}\,K^{-1}}$

Tab. 3.7: Variable geometry parameters of the generic battery module simulation model

Part	Parameter	Symbol
Active volume	Width	w_{av}
	Height	h_{av}
	Thickness	t_{av}
Negative tab (Copper)	Width	$w_{\mathrm{tab,n}}$
	Thickness	$t_{\mathrm{tab,n}}$
Positive tab (Aluminum)	Width	$w_{\mathrm{tab,p}}$
	Thickness	$t_{\mathrm{tab,p}}$
Bottom channel (Aluminum)	Width	w_{ch}

3.5.3 Thermal cell meta-model

The thermal cell meta-model (CMM) is a novel meta-model that predicts the maximum temperature delta within a battery pouch cell after a charging process. It is based on a neural network where the central parameters that influence the cells spatial thermal behavior are given as an input, and the maximum and the minimum temperature in the cell are predicted to obtain the maximum temperature difference as an output. The neural network is implemented in Python using the two machine learning libraries TensorFlow [163] and scikit-learn [164]. As measurement data for the training of the neural network is not available for a high variety of different cell dimensions and boundary conditions, it is trained with data generated by the 3D ECM described in section 3.3.
Below, the data generation is described in detail. Afterwards, the development of the neural network is explained including setup, parametrization, training and evaluation.

Data generation

With the 3D ECM a great number of different charging processes are computed. At the end of the charging process, the maximum and the minimum temperature within the cell are evaluated. For all of the simulations, the 3D geometry given in figure 3.6b is used. The material properties of the active volume correspond to the materials of the KIT20 cell and are given in table 3.1.
The following parameters and boundary conditions determine the spatial temperature distribution within the active volume of a cell and are thus varied:

- Height, width and thickness of the active volume (h_{av}, w_{av} and t_{av}).
- Negative and positive tab width as well as the width of the bottom cooling channel ($w_{\mathrm{tab,n}}$, $w_{\mathrm{tab,p}}$ and w_{ch}). These widths define the location, where heat is exchanged with the cooling system.
- Heat flux at the positive and negative tab as well as at the bottom cooling channel ($\dot{q}_{\mathrm{tab,n}}$, $\dot{q}_{\mathrm{tab,p}}$ and $\dot{q}_{\mathrm{ch}}$). These fluxes determine the amount of heat that is transferred at the boundary interfaces to the cooling system.
- Heat flux at the side surfaces ($\dot{q}_{\mathrm{surf,1}}$ and $\dot{q}_{\mathrm{surf,2}}$). This flux determines the amount of heat that is exchanged at the large side surfaces of the cells (e.g. heat exchange between the single cells or between the outside cells and the end-plates).
- Initial temperature T_{init}. As the heat generation within the cell depends on the temperature, the initial temperature influences the thermal behavior.
- C-rate Cr. Like the initial temperature, the C-rate influences the heat generation within the cell as it depends on the C-rate.

The simulation of the charging process is a transient simulation which always starts at an initial voltage of 3.0 V and ends as soon as the maximum voltage of 4.2 V is reached. Naturally, from the above mentioned variation parameters the geometric parameters do not vary over time. As a simplification it is assumed that also the C-rate and the fluxes, which could also be non-constant during a charging process, are constant over time. These assumptions are justified in the following.

Assuming a fast-charging process with a CCCV charging protocol (which is, as explained in section 2.1.2, a good universal choice for a charging process), the C-rate is constant over a long time period and a very high state of charge is usually reached at the end of that constant current phase. This usually marks the end of the fast charging process as during the following constant voltage phase the electric load on the battery cell drops drastically as it is limited by the maximum voltage of the cell. Thus, the SoC increases much slower and the heat generation within the cell is significantly lower. Consequently it is reasonable to evaluate the temperature delta at the end of the fast charging phase with the constant current/C-rate until the maximum voltage is reached.

The heat fluxes across the boundary faces of the active volume could be non-constant over time, for instance because of a specific control scheme for the cooling fluid temperature. Still, they are assumed to be constant over time as a) including control schemes for the cooling temperatures increases the complexity significantly and b) controlling the cell cooling in a way that the heat flux is as constant as possible is an attractive strategy as the heat generation within the cell is also nearly constant for a wide time range (see figure 3.7e). Simple test simulations have shown, that the deviation in the temperature delta is small (approx. 0.5 K) when a constant, averaged heat flux is used compared to a transient profile.

The variation parameters are varied within the value ranges given in table 3.8. The value ranges for height, width and thickness are derived from [29]. The tab widths and the channel width are varied between 5 % and 95 % of the active volume height and active volume width respectively. The values for the tab and channel heat fluxes are obtained from a rough calculation that assumes, that the largest cell with the largest tab cooling widths could be kept at a constant temperature of 40 °C with tab cooling only during a 3C charging process. The side surface heat flux values are also obtained from a rough calculation, and correspond to the heat flux between two 5 mm thick cells when there is a temperature difference of 1 K between the cells. The range of the initial temperature corresponds to the operating temperatures during a charging process that are specified for the KIT20 cell [139]. The C-rate is varied between 1C and the maximum allowed charging C-rate for the KIT20 cell, which is 3C [139].

With the variation parameter ranges given in table 3.8, a Latin hypercube sampling [165, 166] is preformed to generate 2500 random samples of the variation parameters for the 3D simulations. On the created samples, a simple check is performed to eliminate parameter combinations that lead to extreme temperatures. The average volumetric heat generation rate $\dot{q}_{\mathrm{tot,avg}}$ within a cell is estimated via linear interpolation on a grid created with the 1D ETM described in section 3.2 for the C-rates and temperatures given in equation 3.3a and 3.3b

Tab. 3.8: Maximum and minimum value of the variation parameters for the data generation

Parameter	Symbol	Min. value	Max. value	Unit
Active volume height	h_{av}	90	230	mm
Active volume width	w_{av}	200	600	mm
Active volume thickness	t_{av}	5	15	mm
Negative tab width factor	$r_{\mathrm{tab,n}}$	0.05	0.95	-
Positive tab width factor	$r_{\mathrm{tab,p}}$	0.05	0.95	-
Channel width factor	r_{ch}	0.05	0.95	-
Heat flux negative tab	$\dot{q}_{\mathrm{tab,n}}$	-5527	5527	$\mathrm{W m^{-2}}$
Heat flux positive tab	$\dot{q}_{\mathrm{tab,p}}$	-5527	5527	$\mathrm{W m^{-2}}$
Heat flux channel	$\dot{q}_{\mathrm{ch}}$	-5527	5527	$\mathrm{W m^{-2}}$
Heat flux surface 1	$\dot{q}_{\mathrm{surf,1}}$	-232	232	$\mathrm{W m^{-2}}$
Heat flux surface 2	$\dot{q}_{\mathrm{surf,2}}$	-232	232	$\mathrm{W m^{-2}}$
Initial temperature	T_{init}	0	40	°C
C-rate	Cr	-3	-1	$\mathrm{h^{-1}}$

respectively. The final temperature T_{end} of the cell is then estimated based on the parameters of the sample and the assumed constant heat generation rate with the following formula:

$$T_{\mathrm{end}} = T_{\mathrm{init}} + \frac{\dot{q}_{\mathrm{tot,avg}} V_{\mathrm{av}} + \sum \dot{Q}_{\mathrm{boundary}}}{\rho_{\mathrm{av}} V_{\mathrm{av}} c_{\mathrm{p,av}}} \frac{1}{|Cr|} \tag{3.19}$$

Therein, $\dot{Q}_{\mathrm{boundary}}$ are the heat flow rates on the boundary surfaces of the active volume. If the final temperature T_{end} is below −10 °C or above 60 °C, the sample is dropped. After that check, 2108 parameter sets remained for the 3D simulations. During the 3D simulations, 19 simulations failed due to convergence issues that could not be resolved.

The results analysis of these remaining 2089 3D simulations showed, that in average a maximum temperature delta ΔT_{max} of 10.4 K was reached, defined as the difference between the maximum and the minimum cell temperature. The results of the 3D simulations are analyzed in more detail using the Pearson correlation coefficient between the variation parameters and the main outputs, namely the maximum, minimum and average cell temperature as well as the maximum temperature delta. The resulting correlation matrix is shown in figure 3.16.

Because of the random sampling of the variation parameters there should not be a correlation between them. However, a correlation between the tab widths and the active volume height and the channel width and the active volume width is observed. This results from the choice, that the tab and channel widths are always a fraction of active volume height and width. Also a slight correlation between the heat fluxes is observed. Due to the elimination of parameter sets that lead to extreme temperatures, this correlation is introduced. As extreme temperatures are usually reached, when all fluxes are positive or negative at the same time, these combinations are more likely to be eliminated. Consequently, a slightly negative correlation coefficient is observed.

Looking at the influence of the variation parameters on the output values it stands out, that the temperature delta is mainly influenced by the geometric parameters and the C-rate and less by the heat fluxes. Also, the thickness of the active volume does not seem to have a significant influence on the temperature delta. In contrast to that the cell temperatures are mainly influenced by the heat fluxes, C-rate and the initial temperature. The heat fluxes at the tabs have less impact than the heat flux to the cooling channel and again, the cooling channel heat flux has less influence than the side surface fluxes.
Overall, the variation parameters seem to be a good choice as they all are influencing the thermal behavior of the cell including the maximum temperature delta.

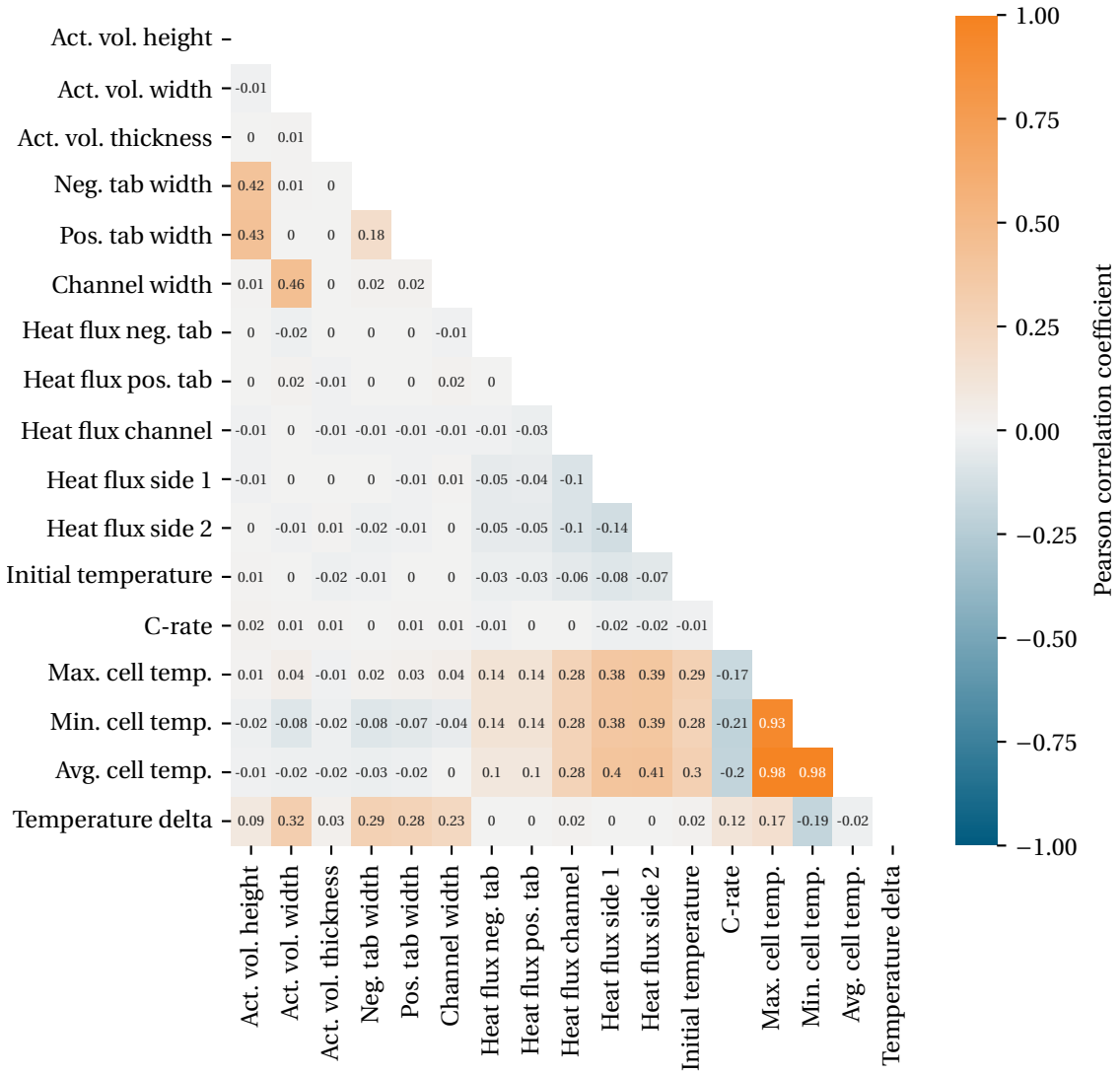

Fig. 3.16: Pearson correlation coefficient of the variation parameters and the main thermal outputs

Neural network

The structure of the neural network is shown in figure 3.17. All of the input quantities are depicted on the left at the input layer, the output quantities – the maximum and the minimum temperature within the cell ($T_{\max}$ and $T_{\min}$) – are displayed on the right at the output layer. In-between the hidden layers are sketched.
Besides the variation parameters of the data generation (table 3.8) that are used as input quantities, several tests revealed, that adding additional, available input parameters to the neural network improves the result. The following input parameters were added:

- End time t_{end}. The point in time when the charging process ends and the terminal voltage of 4.2 V is reached.
- Average temperature T_{avg}. The average temperature of the cell is available in the 1D simulation model of the module.
- Heat flow rates $\dot{Q}$. Besides the average heat fluxes (in $\mathrm{W\,m^{-2}}$) also the average heat flow rates (in W) of all boundary interfaces were added.

80 % of the data generated with the 3D ECM model is used for the training and the hyperparameter optimization of the neural network, 20 % of the data is set aside as a test set that is solely used to test the performance of the neural network after the training process. Prior to inputting the data in the neural network, it is scaled so that all inputs are within the range of 0 to 1.
In four steps, the hyperparameters of the neural network are optimized. During all of the steps when the hyperparameters are varied, repeated k-fold cross validation is used with 5 folds and 3 repetitions.
In the first step, the number of hidden layers is varied between 1 and 5 and the number of neurons between 5 and 60, depending on the number of hidden layers. A detailed summary of the hyperparameter inputs is given in the appendix in table A.15. Figure 3.18a shows the results of the first optimization step: For each number of hidden layers, the five neuron configurations with the lowest RMSE values are depicted. The overall lowest RMSE is achieved with 2 layers and 40 neurons in the first and 35 neurons in the second hidden layer. Consequently, for all following calculations these values are used.
In the second step, the activation function is varied (sigmoid vs. ReLU (rectified linear unit)) as well as the batch size, which is varied between 2 and 16. Again, the detailed hyperparameter inputs are given in table A.17. In figure 3.18b the results of that optimization process are displayed. The lowest RMSE is obtained with a sigmoid activation function and a batch size of 2. These values are used for the further calculations.
In the third step, the learning rate is varied between 1×10^{-4} and 1 (detailed inputs in table A.18). The results of the third optimization step are shown in figure 3.18c where the RMSE is displayed over the learning rate. The lowest RMSE is achieved with a learning rate of 0.001, which is consequently used in the following.

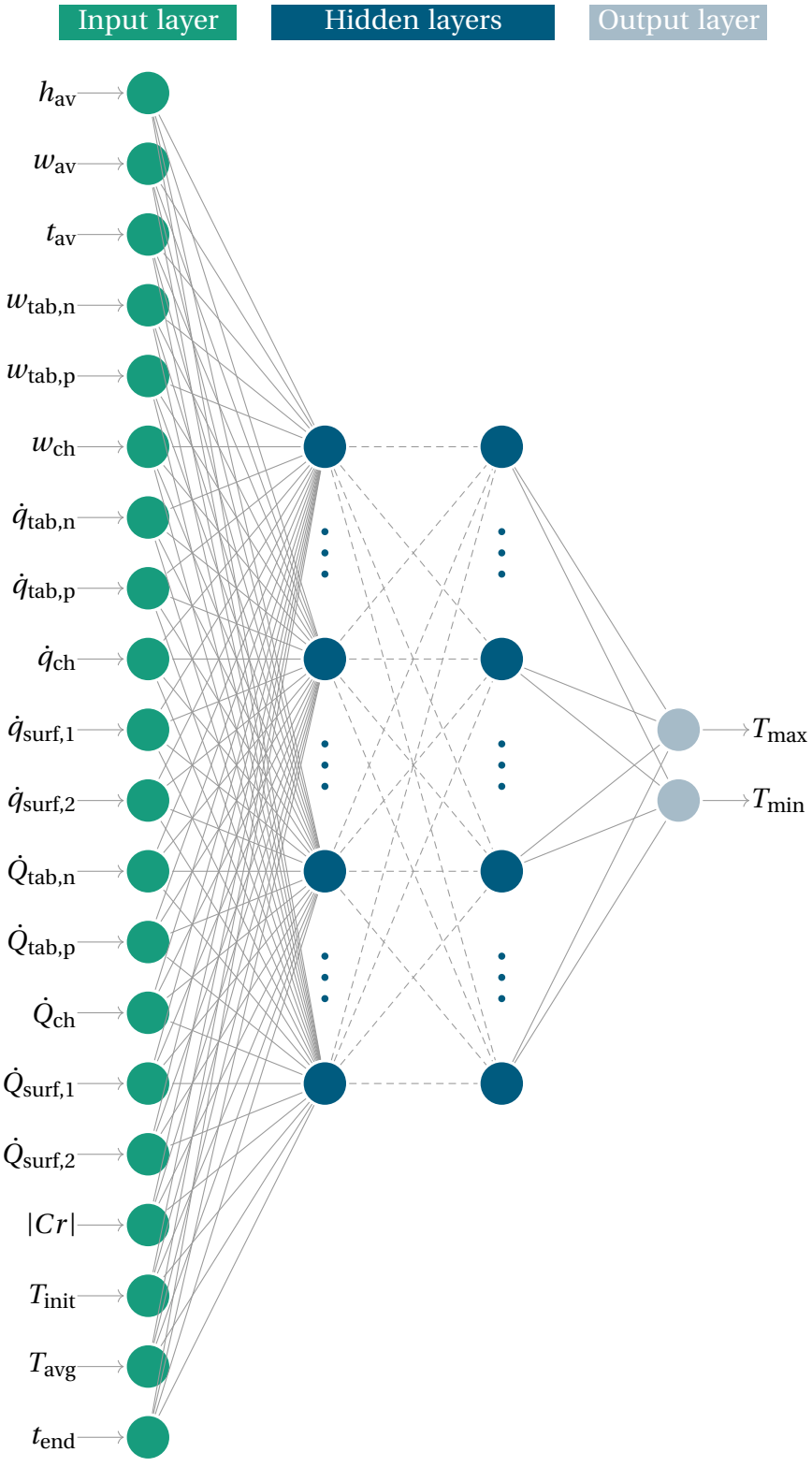

Fig. 3.17: Structure of the neural network for the prediction of the maximum and minimum temperature within the battery cell active volume

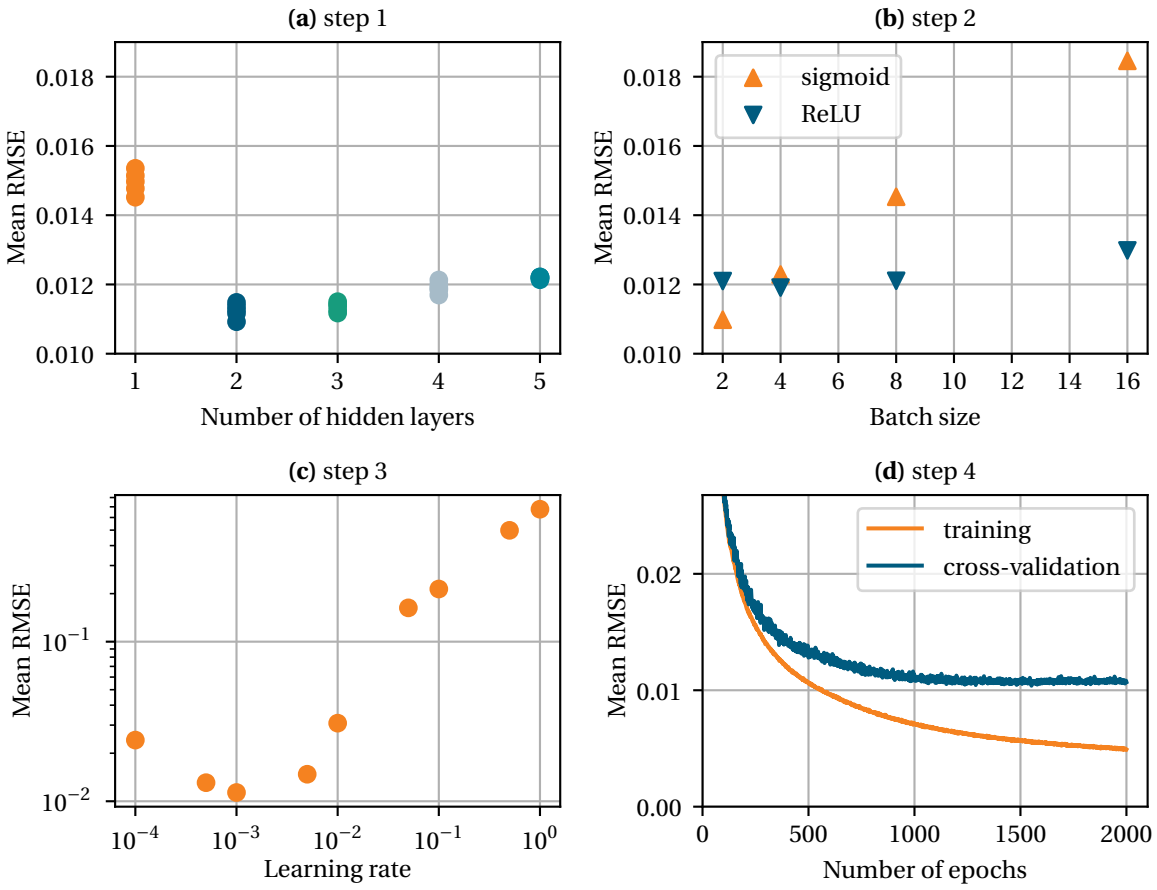

Fig. 3.18: Optimization results of the neural network hyperparameters

Tab. 3.9: Final hyperparameters of the neural network

Hyperparameter	Value
Number of hidden layers	2
Number of neurons in hidden layer 1	40
Number of neurons in hidden layer 2	35
Activation function in hidden layers	sigmoid
Activation function in output layer	linear
Batch size	2
Learning rate	0.001
Training epochs	1000
Loss function	mean squared error
Optimization algorithm	Adam

As a fourth and last step of the hyperparameter optimization procedure, the number of epochs is analyzed during the training process. As mentioned in section 2.4, this is a useful check to avoid overfitting. As can be seen from figure 3.18d, the error of the cross validation set decreases notably for the first 1000 training epochs, afterwards, it remains nearly constant while the training error still decreases. Thus, the training is stopped after 1000 training epochs to avoid overfitting. The final set of hyperparameters is given in table 3.9.
Evaluating the final, trained neural network with the test data leads to the results in table 3.10. The maximum temperature $T_{\max}$, the minimum temperature $T_{\min}$ and the maximum temperature delta $\Delta T_{\max}$ are compared using the RMSE and MAE between the reference result from the 3D simulations and the prediction of the neural network.
The error for the temperature delta is slightly higher than the errors for the max. and min. temperature as the delta value is based on both of the other values and thus, the errors sum up. Also, evaluating the error values only for test data up to 50 °C or 60 °C it may be observed that the errors decrease. Thus, the prediction of the neural network seems less accurate for high temperatures at the boundaries of the training data.
In summary, with a maximum RMSE of 0.79 K and a maximum MAE of 0.52 K the prediction of the neural network for the absolute temperatures is accurate. The same holds for the maximum temperature delta: Considering the fact, that the average $\Delta T_{\max}$ of the data is 10.4 K, the maximum RMSE of 1.05 K and maximum MAE of 0.71 K are low error values. Thus, the NN is considered valid for the prediction of the maximum temperature delta within a cell.

Tab. 3.10: Results of the neural network applied to the test data

	$T_{\max}$		$T_{\min}$		$\Delta T_{\max}$		
Temperature range	RMSE	MAE	RMSE	MAE	RMSE	MAE	**Unit**
Entire range	0.79	0.52	0.64	0.47	1.05	0.71	K
up to 60 °C	0.66	0.48	0.59	0.44	0.95	0.68	K
up to 50 °C	0.61	0.44	0.57	0.43	0.90	0.65	K

3.5.4 Optimization procedure

As mentioned in chapter 1, the thermal design of a battery system or module leads to a conflict of objectives between fast charging capability, energy density and lifetime of the system. From a thermal point of view, the fast charging capability is mainly limited by the maximum temperature within the battery system. Lowering the maximum temperatures in a battery system requires a more capable cooling system, which results in larger structures and thus an increased weight. At the same time, locally high cooling rates could lead to an uneven distribution of the heat within the cells, and thus larger temperature differences that lower the lifetime of the cells.
This conflict of objectives is analyzed with the developed generic battery module model. The optimization objectives are:

- Minimization of the maximum temperature $T_{\max}$ in the battery module.

- Minimization of the mass m of the cooling system. The mass of the cell tabs is considered in the cooling system mass as they are counted as a part of the cooling system due to the heat transfer during tab cooling. (The mass of the active volume is not considered as it does not contribute to the cooling system.)
- Minimization of the maximum temperature delta $\Delta T_{\max}$ within one cell of the module.

A multi-objective Pareto optimization is performed to find as many Pareto-optimal designs as possible. A genetic algorithm, namely NSGA-III [167, 168], is used for the solution of the optimization problem. It is implemented in the used simulation software GT SUITE, Version 2023 [158]. Two exemplary design optimization scenarios are set up to analyze the thermal design of the generic battery module.

Scenario 1

In the first design optimization scenario, the geometric parameters of the active volume are fixed and only the parameters of the cooling interfaces are varied. This is done to compare the cooling designs – tab cooling vs. bottom cooling vs. combined cooling – on a cell with dimensions similar to the dimensions of a given state of the art battery pouch cell. As an example, cell dimensions similar to the LG Chem E66A cell of the Porsche Taycan are selected [169]. The dimensions are given in table 3.11.

Tab. 3.11: Fixed geometry parameters of scenario 1

Parameter	Symbol	Value
Active volume height	h_{av}	104 mm
Active volume height	w_{av}	350 mm
Active volume height	t_{av}	12 mm

The cooling interface parameters that are optimized are summarized in table 3.12. The upper and lower bounds of the optimization variables are inserted to limit the design space. This avoids the optimization towards unreasonably low or high values and ensures that the variables remain within the training space of the CMM.
As a load case for the optimization a 2C charging process is selected. All load and initial conditions are summarized in table 3.13. The optimization is performed individually for a module with tab cooling only, a module with bottom cooling only and a module which

Tab. 3.12: Optimization variables of scenario 1 including the upper and lower bounds of the variables

Optimization variable	Symbol	Lower bound	Upper bound	Unit
Negative tab thickness	$t_{\text{tab,n}}$	0.2	5	mm
Positive tab thickness	$t_{\text{tab,p}}$	0.2	5	mm
Negative tab width factor	$r_{\text{tab,n}}$	0.5	0.9	-
Positive tab width factor	$r_{\text{tab,p}}$	0.5	0.9	-
Channel width factor	r_{ch}	0.25	0.9	-

combines both cooling systems. The given volume flow rate of the cooling fluid is in all three cases distributed over all channels to obtain similar flow conditions over all cooling variants.

Tab. 3.13: Initial and load conditions of design optimization scenario 1

Parameter	Symbol	Value
Cell nominal capacity	Q_{nom}	43.4 Ah
C-rate	Cr	$-2\,\mathrm{h}^{-1}$
Initial SoC	SoC_{init}	0.0 %
Max. cell voltage	U_{end}	4.2 V
Initial temperature components and air	T_{init}	30 °C
Initial temperature fluid	$T_{\mathrm{init,fluid}}$	20 °C
Volume flow rate cooling fluid	$\dot{V}_{\mathrm{fluid}}$	$10\,\mathrm{L\,min}^{-1}$
Outlet pressure	p_{out}	1 bar

Scenario 2

In the second design optimization scenario, also the geometric parameters of the active volume are optimized. As in many battery module design processes a certain capacity of the cell is required, it is assumed that the capacity of the cell is always constant in the second scenario and the optimal thermal design of the cell is sought. For the sake of simplicity, the thickness of the active volume is kept constant as the sensitivity analysis of the training data revealed that its influence on the thermal behavior is neglectable (see figure 3.16). The width and the height of the active volume will be varied though. The width is chosen as the optimization variable and the height is adjusted so that the capacity of the cell always equals $Q_{\mathrm{nom}} = 60\,\mathrm{Ah}$. The formula for the calculation is given in table 3.14 where the fixed geometry parameters are listed.
The variable parameters are shown in table 3.15, where also the upper and lower bounds are given. Again, the three different cooling approaches are taken into account during the optimization (tab cooling, bottom cooling, combined cooling). To investigate also the influence of the C-rate, the system is optimized with two different charging C-rates: 2C and 3C. The optimization is performed individually for the each cooling type and C-rate configuration. Table 3.16 displays the initial and load conditions of the second optimization scenario.

Tab. 3.14: Fixed geometry parameters of scenario 2. The height of the active volume is calculated so that the nominal capacity of the cell is constant and the volumetric energy density equals the volumetric energy density of the KIT20 cell.

Parameter	Symbol	Value
Active volume height	h_{av}	$= \frac{Q_{\mathrm{nom}}}{w_{\mathrm{av}} t_{\mathrm{av}}} \frac{V_{\mathrm{nom,KIT20}}}{Q_{\mathrm{av,KIT20}}}$
Active volume thickness	t_{av}	12 mm

Tab. 3.15: Optimization variables of scenario 2 including the upper and lower bounds of the variables

Optimization variable	Symbol	Lower bound	Upper bound	Unit
Active volume width	w_{av}	250	550	mm
Negative tab thickness	$t_{\mathrm{tab,n}}$	0.2	5	mm
Positive tab thickness	$t_{\mathrm{tab,p}}$	0.2	5	mm
Negative tab width factor	$r_{\mathrm{tab,n}}$	0.5	0.9	-
Positive tab width factor	$r_{\mathrm{tab,p}}$	0.5	0.9	-
Channel width factor	r_{ch}	0.25	0.9	-

Tab. 3.16: Initial and load conditions of design optimization scenario 2

Parameter	Symbol	Value
Cell nominal capacity	Q_{nom}	60 A h
C-rate	Cr	$\{-2, -3\}$ in h^{-1}
Initial SoC	SoC_{init}	0.0 %
Max. cell voltage	U_{end}	4.2 V
Initial temperature components and air	T_{init}	30 °C
Initial temperature fluid	$T_{\mathrm{init,fluid}}$	20 °C
Volume flow rate cooling fluid	$\dot{V}_{\mathrm{fluid}}$	10 L min^{-1}
Outlet pressure	p_{out}	1 bar

4 Results

4.1 Tab-cooled battery module prototype

4.1.1 Results of the tab cooling tests

The results of the tab cooling test were previously published in an own publication [154], as already mentioned in sections 3.4.1 and 3.4.2. The following paragraphs are based on this publication.

At first, the results of the heat-up-cool-down test are analyzed. They are shown in figure 4.1 where in 4.1a the average temperature of the fluid, the tabs and cells are given over time and in 4.1b the difference between the fluid temperature and the tab temperature over time.

As can be seen from figure 4.1a, the tab temperature is always close to the fluid temperature and reacts directly to the temperature changes when the heating or the cooling phase starts. In contrast, the temperature change of the cells is significantly slower. At the beginning of the heating phase, the maximum heating rate of the cells is $0.36\,\mathrm{K\,min^{-1}}$. When the cooling starts, a maximum cooling rate of $-0.40\,\mathrm{K\,min^{-1}}$ was measured for the cells. Still, even after the cooling and heating for 2 h a stationary state is not reached for the average cell temperature. This indicates a thermal bottleneck between the cells and the fluid. However, since the tab temperature is always very close to the fluid temperature, the plastic material between the

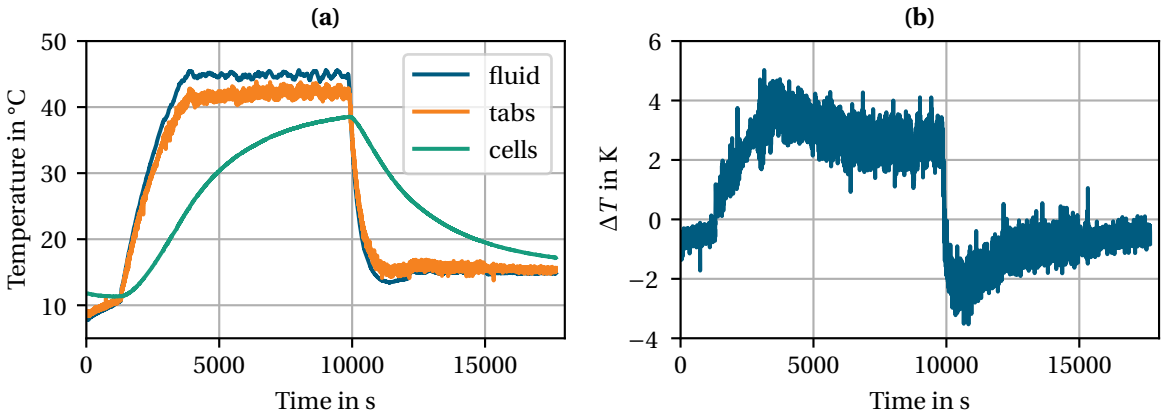

Fig. 4.1: Results of the heat-up-cool-down test: (a) shows the average temperature of the fluid, the tabs and the cells; (b) shows the temperature difference between the fluid and the tabs (from: [154])

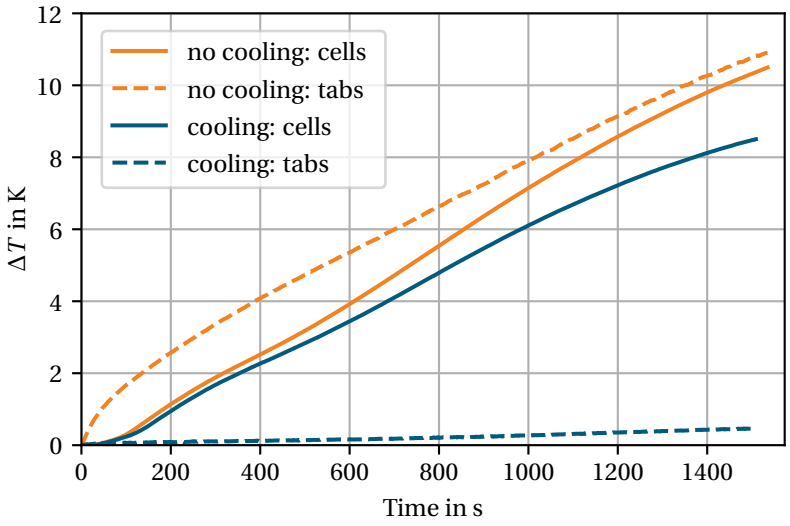

Fig. 4.2: Average temperature increase of the cells and the tabs of the 2C charging tests (based on: [154])

tabs and the cooling channels does not appear to be the limiting factor in the thermal path. It seems, that the cross-section of the tabs itself causes the slow heat transport.

The temperature difference between the fluid and the tabs in 4.1b shows, that during the heating phase the magnitude of the average temperature difference is with 3.0 K slightly higher compared to the cooling phase with in average −1.5 K. From this difference in magnitude it can be concluded, that the tab TCs are slightly sensitive to the ambient temperature.

In figure 4.2, the average temperature results of the 2C charging tests are displayed. The orange lines depict the results of the charging test without cooling, the blue lines depict the results with an activated cooling.

Without the tab cooling, the cell temperature increases by 10.5 K, with the cooling activated, the cell temperature increase is 8.5 K. Thus, the tab cooling reduces the maximum cell temperature by approximately 2 K. Without the tab cooling, the tab temperature is slightly higher than the cell temperature because of the Joule heating in the metallic tabs. In contrast to that, the activated tab cooling reduces the tab temperature drastically and nearly no temperature increase is observed for the tabs. Again, this shows that the thermal conductivity of the plastic material is sufficient but the high temperature difference between the tabs and the cells indicate an inefficient thermal path between the tabs and the cells.

Figure 4.3 compares the average cell temperature increase in the three measurement sections between the cells in the module for the 2C charging tests.

The cell temperatures in the middle of the module (between cells 6 and 7) are 2 K to 5 K higher than the temperatures in the outer measurement sections (between cells 1 and 2 and between cells 11 and 12). That temperature difference is higher when the cooling is not activated. It originates from the high thermal capacity of the module end-plates and the convective heat transfer to the environment. Even though the tab cooling is able to lower that difference, it is

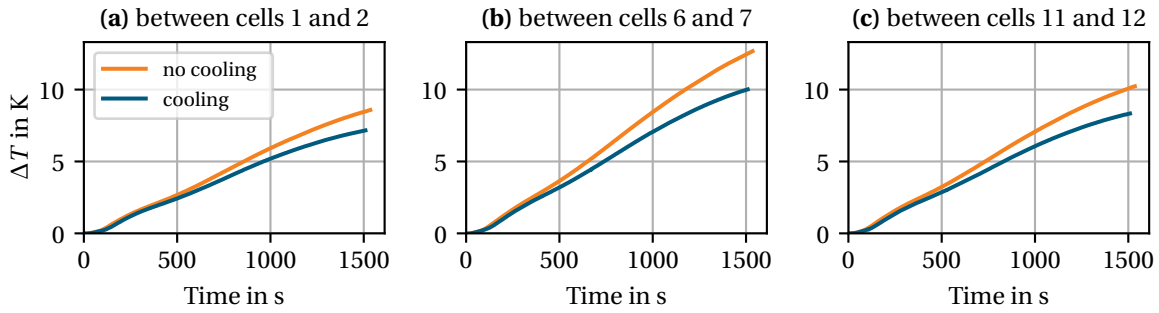

Fig. 4.3: Average cell temperature increase in the three different measurement sections during the 2C charging tests (based on: [154])

surprising that despite the symmetric design of the tab cooling these temperature differences between the inside and the outside of the module are so clearly present.

Conclusion

The following three key findings can be derived from the experimental investigations:

1. The technical realization of a tab cooling system in a battery module using thermally conductive plastics could be proven. For the tested cells, the thermal conductivity of the plastic material is sufficient to transport the heat from the tabs to the cooling system and thus, the plastic material is not the thermal bottleneck. So with respect to research question 1 a first answer may be given: Tab cooling with thermally conductive plastics is technically possible. However, its effectiveness in the presented configuration is very limited.

2. The thermal bottleneck in the tab cooling system are the cell tabs. Their cross-sectional area is too small and the distance between the active volume of the cell and the cooling channels is too large to transport the heat efficiently to the cooling fluid. Thus, tab cooling could only work if the cells are thermally optimized for the cooling system. This finding underlines the need for an answer to research question 2.

3. Despite the symmetric design of the tab cooling system, significant temperature differences between the single cells occurred. Thus, it is important to consider the thermal influences of the surrounding module structures to achieve equal temperatures in all cells. Of course, in a vehicle battery system with multiple modules, that effect is less present as there is less convective heat transfer to the environment and the module housing structures are thinner. Still, countermeasures on the outer sides of the battery system could be reasonable to enable equal cell temperatures.

4.1.2 Validation of the simulation model

With the measurements, the 1D simulation model of the battery module prototype introduced in section 3.4.3 is validated.

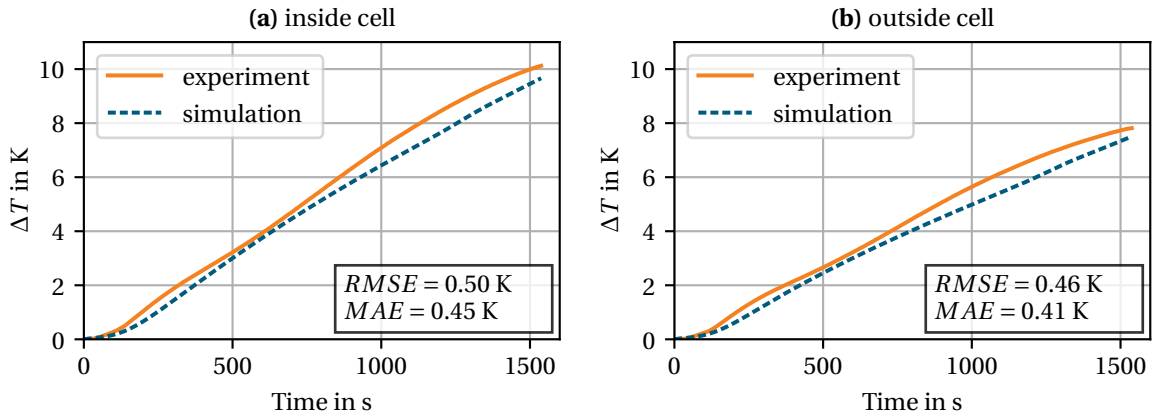

Fig. 4.4: Comparison of the average temperature increase between the measurements and the 1D simulation model of the battery module prototype with activated cooling.

Figure 4.4 compares the temperature results of the 2C charging test for the inside and the outside cell with the tab cooling activated. In the two plots, the increase of the average temperature is displayed over time. The measured temperature increase is illustrated by the orange line and the simulated temperature increase by the blue, dashed line.
The average temperature of the simulation model is slightly below the measured temperature, but overall, the curves are in good agreement, both for the inside cell and the outside cell. Even the non-linear start of the temperature rise at the beginning of the charging process is captured well by the simulation model. The visually good fit is confirmed by the error values, which are with an RMSE of 0.50 K and MAE of 0.45 K for the inside cell and an RMSE of 0.46 K and MAE of 0.41 K sufficiently low.
In figure 4.5, the same comparison is displayed for the 2C charging test with a deactivated tab cooling. Again, the simulation model slightly underestimates the temperature increase. The deviation is a little greater in magnitude than in the previously presented results with the activated tab cooling. Still, both for the inside and the outside cell, the simulation fits well to the measurements as the error values are sufficiently low. The error for the outside cell is with an RMSE of 0.70 K and MAE of 0.64 K slightly lower than for the inside cell with an RMSE of 0.92 K and MAE of 0.83 K.

Conclusion

Overall, the agreement between simulation and measurement is high for both load cases and the error values are low. The slight underestimation of the temperatures could originate from the data of the underlying DFN model (section 3.2). The used data sets are close to the cell chemistry of the KIT20 cell but of course not specifically parametrized for that exact cell. This could lead to the observed deviations.
Still, with errors below 0.92 K, the overall fit of the simulation results to the experimental data is good and the 1D simulation model of the battery module prototype is considered valid. It is able to accurately predict the average thermal behavior of the cells in a charging process

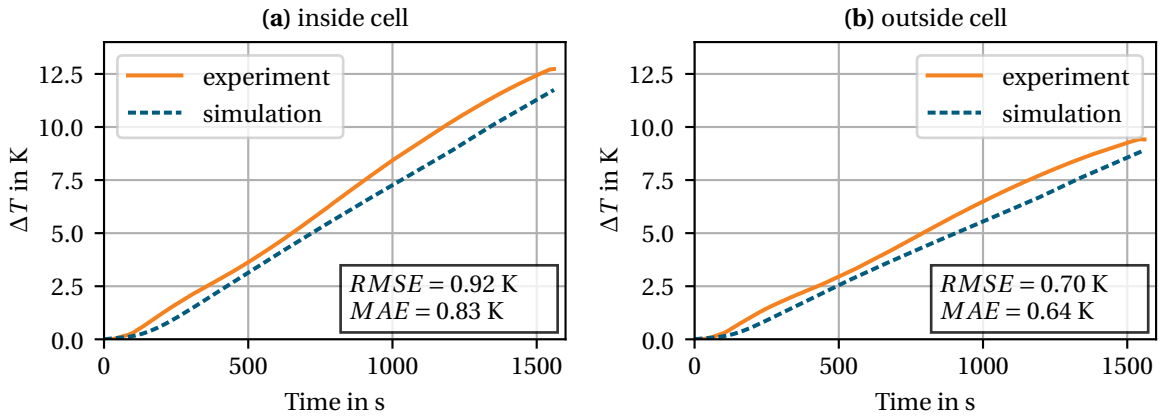

Fig. 4.5: Comparison of the average temperature increase between the measurements and the 1D simulation model of the battery module prototype without cooling.

under different cooling conditions (activated vs. deactivated tab cooling) and at different locations within the module (inside vs. outside cell). Thus, it is further used to analyze the influence of the plastic thermal conductivity in the battery module prototype and, as outlined in section 3.5, the modeling approach also forms the basis for the generic battery module model.

4.1.3 Analysis plastic thermal conductivity

The analysis of the experimental results leads to the hypothesis, that the plastic thermal conductivity is not the limiting factor in the tab cooling system. In contrast to that, the cell tabs itself were identified as the limiting factor for the removal of the heat. Both of these hypotheses are further investigated using the simulation model of the battery module prototype.

Solely by looking at the values for the thermal resistances of the plastic tape R_{plastic}, the negative tab $R_{\text{tab,n}}$ and positive tab $R_{\text{tab,p}}$ the hypothesis can be confirmed for the battery module prototype with the KIT20 cells:

$$R_{\text{plastic}} = 0.24\,\text{KW}^{-1} \tag{4.1a}$$

$$R_{\text{tab,n}} = 2.89\,\text{KW}^{-1} \approx 12 R_{\text{plastic}} \tag{4.1b}$$

$$R_{\text{tab,p}} = 4.89\,\text{KW}^{-1} \approx 21 R_{\text{plastic}} \tag{4.1c}$$

As $R_{\text{tab,n}}$ and $R_{\text{tab,p}}$ occur two times in the simulation model in each tab, the thermal resistance of the tabs is by a factor of 24 to 42 higher than the thermal resistance of the plastic tape.

A possible countermeasure to reduce the thermal resistance of the tabs would be an increased tab thickness. To further analyze that influence in interaction with the plastic thermal conductivity, the 2C charging process with activated tab cooling was repeated with the simulation

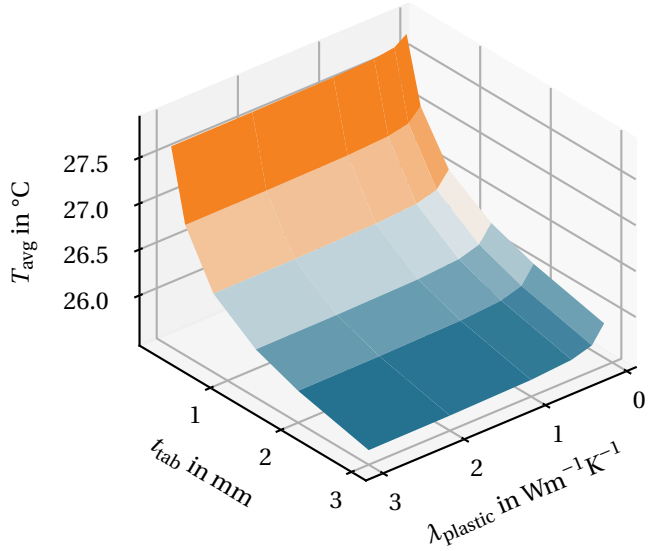

Fig. 4.6: Average cell temperature T_{avg} of the inside cell at the end of the 2C charging process depending on the tab thickness t_{tab} and the thermal conductivity of the plastic tape $\lambda_{plastic}$

model and the following parameter variations:

$$t_{tab} = \{0.2,\ 0.4,\ 0.8,\ 1.4,\ 2,\ 3\} \text{ in mm} \tag{4.2a}$$

$$\lambda_{plastic} = \{0.1,\ 0.25,\ 0.5,\ 1,\ 2,\ 3\} \text{ in } \mathrm{W\,m^{-1}\,K^{-1}} \tag{4.2b}$$

The results of that analysis are shown in figure 4.6 where the average temperature of the inside cell after the 2C charging process is displayed depending on the tab thickness t_{tab} and the plastic thermal conductivity $\lambda_{plastic}$.
Increasing the tab thickness has clearly a strong influence and the average temperature is reduced by approximately 2 K when the thickness is increased from 0.2 mm to 3 mm. However, the vanishing slope of the surface at greater tab thicknesses indicates that further increasing the thickness does not lead to significantly lower temperatures. The influence of the plastic thermal conductivity is nearly insignificant. Even when the thermal resistance of the tabs is low ($t_{tab} = 3\,\mathrm{mm}$), there is only a temperature difference of 0.31 K between the highest and the lowest thermal conductivity configuration.

Conclusion

The further investigations with the simulation model confirm that the thermal conductivity of the plastic material is not the limiting factor for the realization of a tab cooling system in a battery module. As the plastic's influence on the average cell temperature is small, there would be even room for design variations like a thicker plastic layer to improve the electrical insulation.
Also, the preceding analysis underlines that tab cooling is only effective if the thermal design of the battery cell is adjusted to the cooling approach. Increasing the tab thickness of the

KIT20 cells improves the cooling up to a factor of 2 compared to the initial configuration. However, this improvement is limited as soon as a certain tab thickness is reached. This leads to the assumption that all geometric parameters of the battery cell need to be optimized for an efficient tab cooling of the cell. The following section will investigate that issue using the generic battery module model.

4.2 Optimization with the generic battery module model

4.2.1 Computing performance

Before the results of the optimization scenarios are presented, the computing performance of the proposed simulation model is discussed.

The computation time for a single charging process with the generic battery module model took between 15 s and 18 s on a single core of a desktop computer (processor: 2× Intel® Xeon® CPU E5-2697 v4 (2.30 GHz), memory: 256 GB). The majority of the time is needed for the transient solution of the 1D model. The post-processing with the evaluation of the neural network is remarkably fast and takes less than 1 s. It does not significantly increase the overall computation time. Thus, the goal of a fast (<1 min) prediction of the temperature differences in a module after a charging process was successfully achieved. With that speed, in the optimization run of the first scenario, 864 designs could be computed per cooling method in around half a day (overall 2592 designs). In the second optimization scenario, also 864 designs per cooling method and per C-rate were calculated (overall 5184 designs), which took around one day.

Compared to other modeling approaches, these are excellent times for optimization during the development process of battery modules and systems. Equivalent 3D models, that are usually used for the prediction of spatial temperature differences in a module, require several hours of computation time for the simulation of a charging process. To achieve these times, the 3D simulations are performed on a powerful computing machine with multiple nodes and cores to parallelize the execution.

For instance, Damblanc [12] performed a 3D simulation of a battery system containing 456 cells and a bottom cooling. On a computer cluster with 128 cores, the computing time of the model was around 2 h for a 2C charging process [12]. Table 4.1 compares that computing time to the computing time of the generic battery module model. The scaling of the computing times to a single cell on a single core shows, that the novel model is faster by a factor of approximately 670. This is a significant reduction which enables the calculation of a high number of different designs in a short amount of time, as presented in the last row of table 4.1. With the novel model, 4800 different designs of a module with six cells can be calculated on a single core within one day. With the state of the art 3D model, only 7 module designs could be calculated in the same amount of time using the same resources.

Thus, the novel model enables and speeds up the optimization process significantly, as the computation time is decreased by two to three orders of magnitude compared to common approaches to date.

Tab. 4.1: Comparison of the computing performance between the developed generic battery module model and a state of the art 3D simulation from Damblanc [12]

	Generic battery module model	**State of the art 3D model [12]**
Number of cells in the module/pack	6	456
Number of used cores	1	128
Computing time charging process	18 s	2 h = 7200 s
Computing time per cell on a single core	3 s	2021 s
Number of designs of a 6-cell-module in one day using a single core	4800	7

4.2.2 Results scenario 1

In the first design optimization scenario, the cooling parameters determining the cooling interface of a state of the art automotive battery cell were optimized (see section 3.5.4). The results of that optimization are shown in figure 4.7 and figure 4.8. As there are three optimization objectives – maximum temperature $T_{\max}$, maximum temperature delta $\Delta T_{\max}$ and mass m – the Pareto front of the optimization is a three-dimensional surface. Both of the result figures contain three two-dimensional projections of that surface to facilitate the graphical visualization. In the two-dimensional projections, the Pareto points are plotted for two optimization variables each. In figure 4.7 the coloring of the points represents the third optimization variable. In figure 4.8, the points are colored according to the underlying cooling type.

In figure 4.7, three distinct points are marked with orange triangles. They represent the solutions where the minimum of each optimization objective was reached.

The minimum $T_{\max}$ is with 30.7 °C only slightly above the initial temperature of the simulation and is reached with a combined cooling, when both tab and bottom cooling were active. As can be seen from figure 4.7c, this choice also leads to a high mass due to the usage of both cooling types and a moderate temperature delta within the cell.

The minimum $\Delta T_{\max}$ of 2.2 K is achieved with a configuration where only the tab cooling is active. However, this configuration also leads to a high maximum temperature and very low weight, indicating that the cooling is overall limited and thus, also the temperature difference within the cell stays at a moderate level. An evaluation of the tab thicknesses and widths confirms that assumption as both the tab thicknesses $t_{\text{tab,n}} = 0.32\,\text{mm}$ and $t_{\text{tab,p}} = 0.27\,\text{mm}$ as well as the widths $w_{\text{tab,n}} = 52.4\,\text{mm}$ and $w_{\text{tab,p}} = 62.9\,\text{mm}$ are close to the lower limits of the optimization parameters.

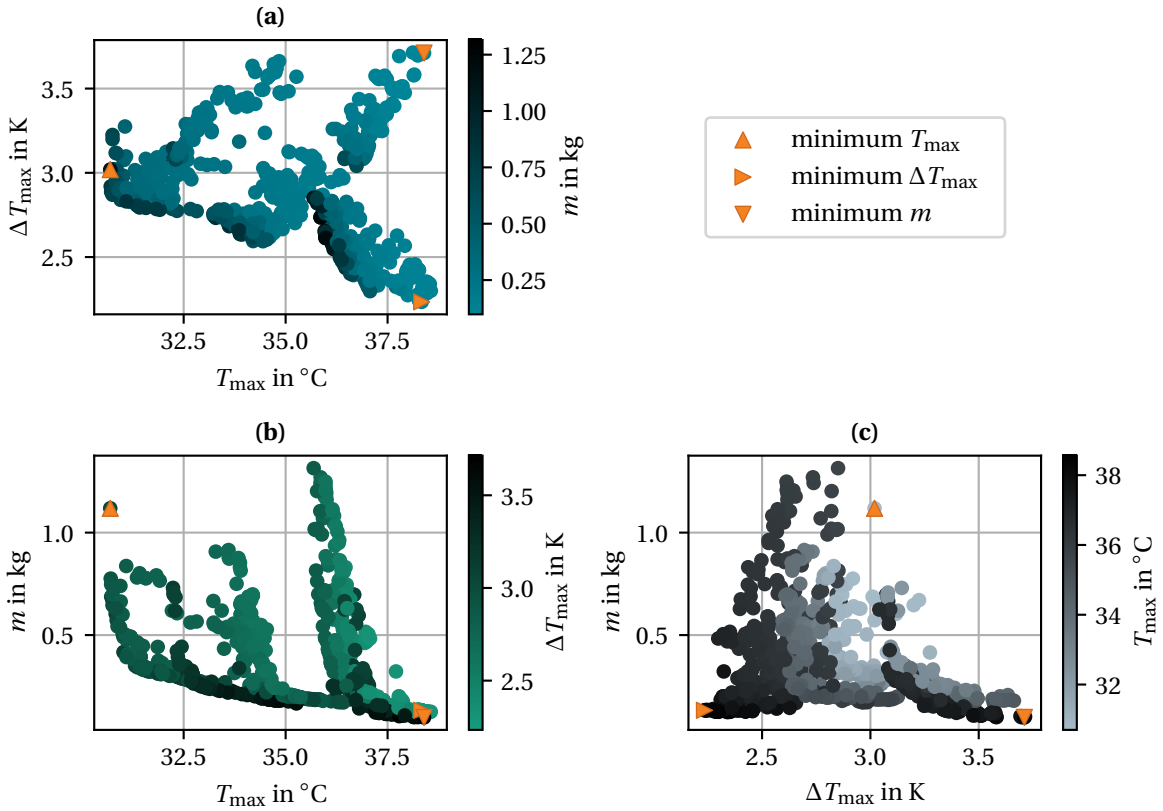

Fig. 4.7: Results of design optimization scenario 1. The three plots show the Pareto-optimal points of the optimization.

A configuration with bottom cooling only achieved the result with the minimum mass m. Here the disadvantage of the configuration is the high maximum temperature and the high temperature delta that results from the narrow cooling channel.

Looking at figure 4.8, the general trends and characteristics of the single cooling approaches are analyzed.

As can be seen from figure 4.8a, tab cooling leads to the lowest temperature differences within the cell, as also stated in literature [7, 8, 10]. However, the overall cooling potential is very limited and temperatures below approximately 35.5 °C are not reached. With a bottom cooling, also lower temperatures around 32 °C are possible, but the temperature delta is with a minimum around 3 K limited. Interestingly, there are two clusters for optimal solutions with the bottom cooling. One, on the right towards higher temperatures and one to the left towards lower temperatures. In the right cluster, the cooling channel width is always particularly small to achieve a low weight, in the left cluster, the opposite is the case. Both clusters are further influenced by the tab thickness and width. Increasing both parameters leads to lower temperature differences but also a higher mass, as depicted in figure 4.8b by the increasing mass at the left-hand side of both clusters.

With the combined cooling the overall lowest maximum temperatures are achieved and also the achievable temperature difference is lower compared to the bottom cooling. However, as

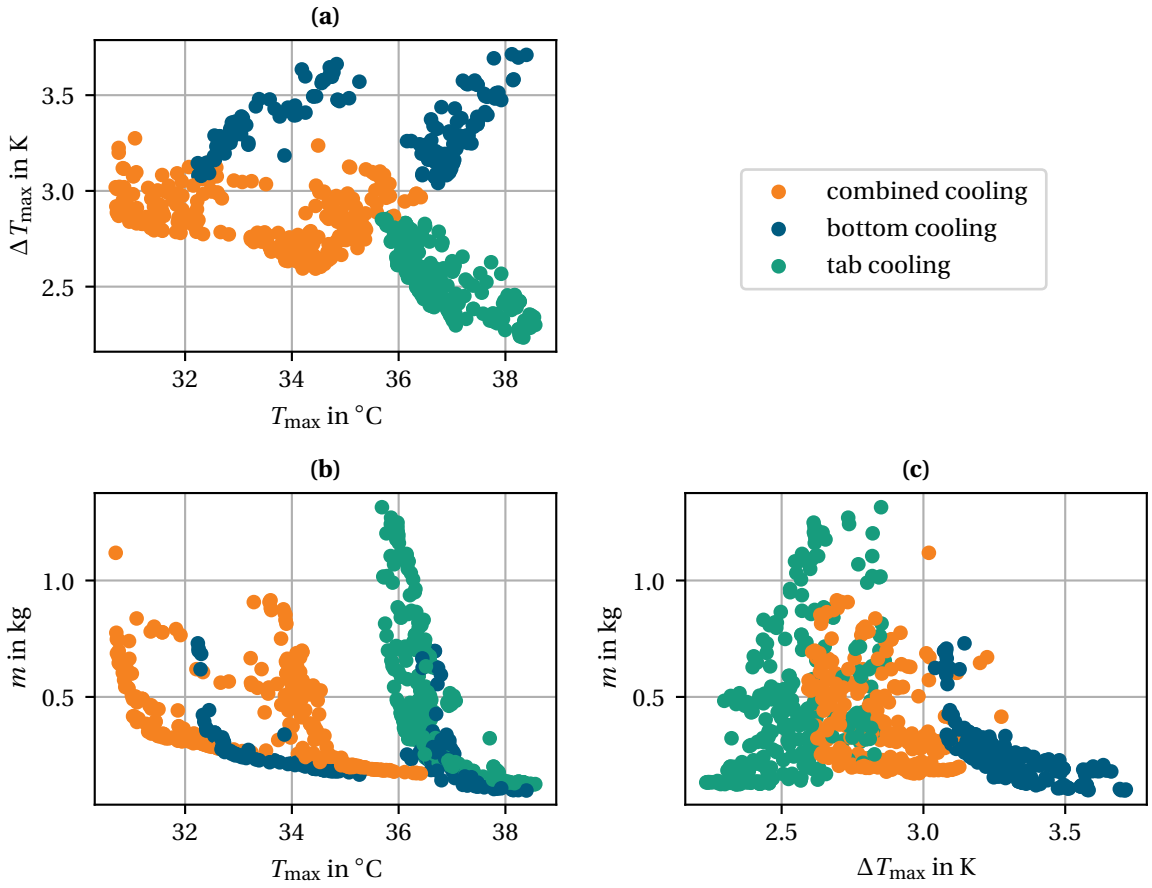

Fig. 4.8: Results of design optimization scenario 1 depending on the used cooling type. The three plots show the Pareto-optimal points of the optimization.

can be seen from figure 4.8c, the minimum mass is always a bit higher compared to the other two cooling methods.

Conclusion

On the first look, all of the cooling systems have their distinct strength as the results above show:

- Combined cooling is best for low maximum temperatures.
- Bottom cooling is the preferred choice for a minimum weight.
- Tab cooling leads to the lowest temperature differences within the cell.

However, regarding the tab cooling results in detail, the low temperature differences do not necessarily lead to a longer lifetime of the cell. As, according to equation 2.1, the temperature delta is only added with a weight of 10 % to the equivalent aging temperature, it could be more attractive to lower the overall temperature of the battery cell to increase the lifetime. Here, bottom cooling with a wide cooling channel or a combined cooling could be advantageous as the overall cooling potential of the tab cooling is limited with the given battery cell dimensions.

4.2.3 Results scenario 2

As described in section 3.5.4, in the second design optimization scenario also the dimensions of the active volume – namely the active volume width and height – are optimized for a cell with a fixed capacity of 60 A h.
The results of that optimization in form of the Pareto-optimal points are presented in figures 4.9 and 4.10. Again, like in the previous section, the 3D Pareto front is reduced to three two-dimensional projections. They are displayed in both figures for the two different C-rates (2C and 3C) with identically scaled axes. As before, in figure 4.9 the distinct points that mark the minimum values for the three optimization objectives are depicted with orange triangles.
Although the geometry of the active volume is free to change now, the results for the overall minimum values are identical to the previous optimization in scenario 1. For both C-rates, the minimum $T_{\max}$ is reached with a combined cooling, the minimum $\Delta T_{\max}$ with a tab cooling and the minimum mass m with a bottom cooling configuration.
In the combined cooling configuration, when the minimum $T_{\max}$ is achieved, the width of the cell and the cooling channel are maximized and close to the upper bound values specified in table 3.15. At the same time, the tabs are thickened moderately to remove a bit of heat through the tab cooling and decrease the heat generated in the tabs due to Joule losses.
In the tab-cooled configuration with the minimum $\Delta T_{\max}$, the width of the cell is reduced close to the lower bound and the width and thickness of the tabs is increased. Interestingly, the optimization lead to a thicker and wider negative tab (Copper) than the positive tab (Aluminum). This indicates, that it is more attractive to remove the heat through the thermally better conducting negative tab than the positive tab.
In the bottom cooling configuration with the minimum mass, the width of the cell is also reduced close to the allowed minimum value. Here, a slight difference between the C-rates occurred as the width was closer to the allowed minimum in the 3C charging process compared to the 2C charging. Both times, the channel width is also minimized to reduce the weight, which however also results in a high maximum temperature as can be seen from figures 4.9a and b.
Figure 4.10 displays the Pareto-optimal results depending on the different cooling methods. Again, the results are similar to design optimization scenario 1. Also, there is no significant difference in the trends between the two different C-rates.
In general, with the combined cooling the lowest temperatures may be achieved while the weight is higher compared to the other cooling approaches. The tab cooling once again leads to the lowest temperature delta within the cells. Interestingly, as the shape of the active volume is now also optimized, the disadvantage with respect to the minimization of $T_{\max}$ is smaller than before. Still, the lowest achievable temperatures are higher compared to the other cooling types. For the bottom cooling, again the slight trend to form two clusters with either a narrow cooling channel and a moderate to low cell width or a wide cooling channel with a high cell width is observed.

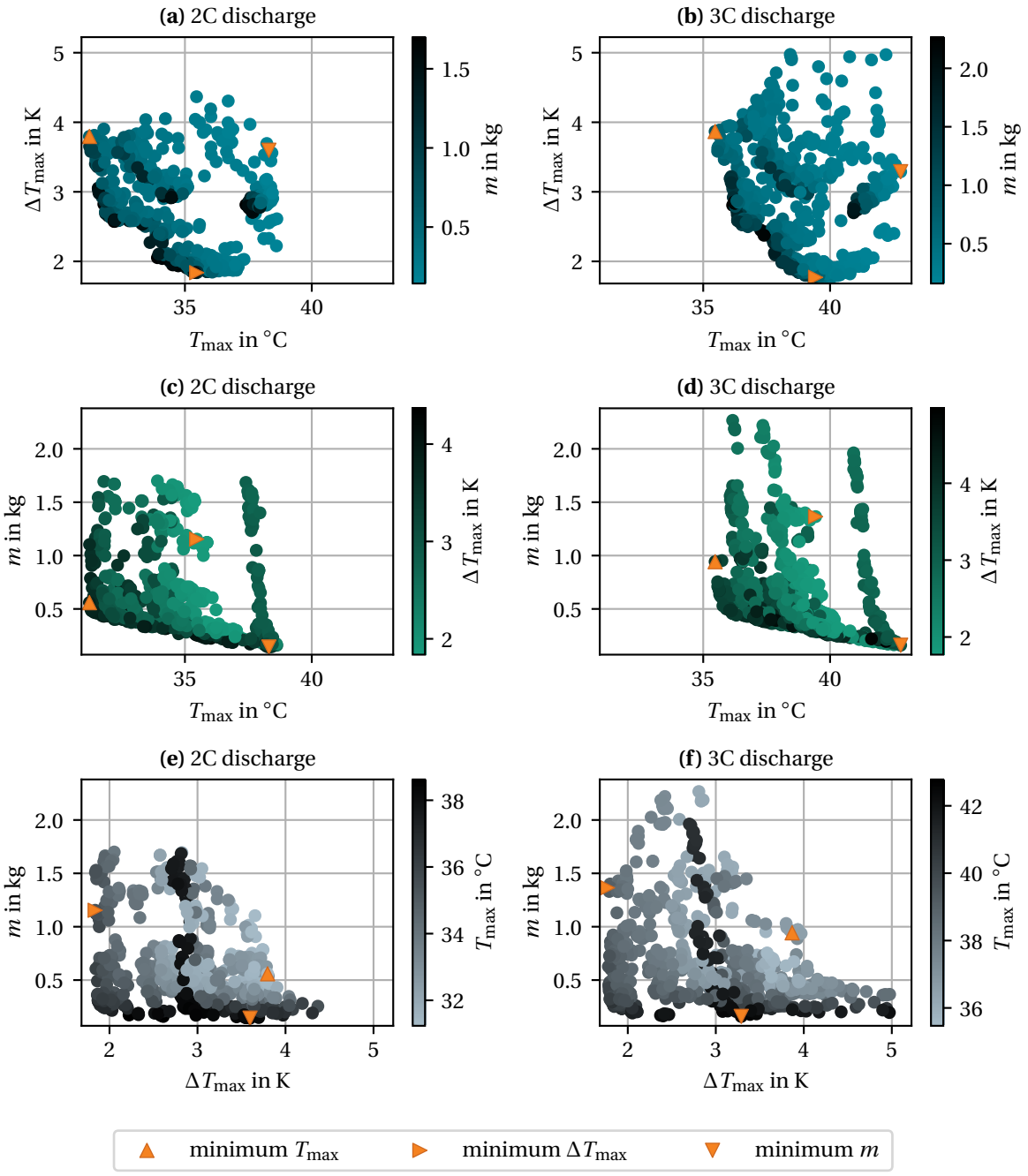

Fig. 4.9: Results of design optimization scenario 2. The three plots show the Pareto-optimal points of the optimization.

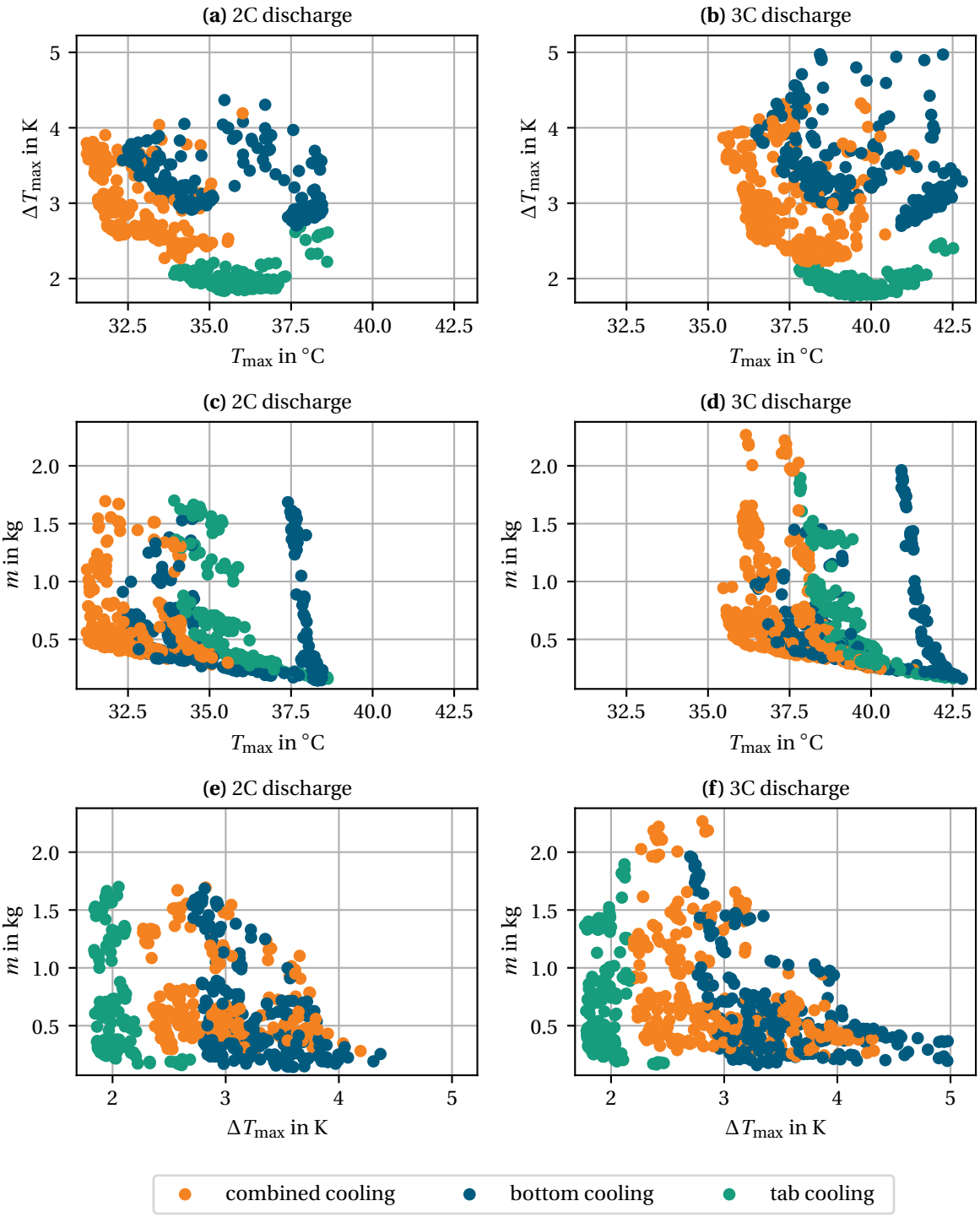

Fig. 4.10: Results of design optimization scenario 2 depending on the used cooling type. The three plots show the Pareto-optimal points of the optimization.

Conclusion

Despite adding an additional optimization variable and allowing flexibility in the geometry of the active volume, the strengths of the cooling approaches are nearly the same as in optimization scenario 1:

- Combined cooling is best for low maximum temperatures and medium-low temperature deltas, which comes at the cost of a higher weight.
- Bottom cooling is the preferred choice for a minimum weight and moderate maximum temperatures but also leads to high temperature differences within the cell.
- Tab cooling achieves the lowest temperature differences at a moderate weight, but with a disadvantage regarding the maximum temperatures.

Again, it may be noted, that even with the optimized geometry of the active volume, the low temperature deltas of the tab cooling are not necessarily an advantage with respect to the lifetime. Using a bottom cooling or a combined cooling, overall lower temperatures may be achieved that contribute stronger to the reduction of the equivalent aging temperature. Looking for example at figure 4.10a, the $\Delta T_{\max}$ is approximately 2 K lower with the tab cooling compared to the bottom cooling. So the equivalent aging temperature would be reduced by 0.2 K. However, with an optimized bottom cooling, $T_{\max}$ is approximately 1.5 K lower which directly lowers the equivalent aging temperature by 1.5 K. Thus, tab cooling seems only attractive if low temperature differences are explicitly needed or if the cells age stronger with the temperature difference than the ones used by Fleckenstein et al. [58].

4.3 Discussion

With the results presented above, it is possible to answer the two research questions posed in section 1.2:

Research question 1: *Is it possible to realize tab cooling with thermally conductive plastics in a module and how is its performance influenced by the thermal conductivity of the plastic material?*

With the experimental results and the validated 1D simulation model of the battery module prototype a clear answer may be given to the first research question: Yes, it is possible to realize a tab cooling system in a battery module using thermally conductive plastic materials. The plastic material is not the limiting factor for the heat transfer between the battery cells and the cooling system. On the contrary, there is even some room for variation regarding the material properties or its thickness without significantly influencing the thermal performance of the cooling system. The thermal bottlenecks in the tab-cooled battery module are the tabs of the cells itself. Due to the small cross-sectional area, their thermal resistance is high and limits the heat transfer to the cooling system. Thus, for a tab cooling system to work effectively, the thermal and geometric design of the cells must be specifically adjusted.

Research question 2: *For given boundary conditions and optimization objectives, what is the optimal thermal design of a pouch cell with tab or bottom cooling and which cooling method should be preferred?*

For both cooling types, the optimal thermal design strongly depends on the desired optimization objectives and boundary conditions. However, from the determined results, the following general trends are derived.

Bottom cooling works best with cells with a high width-to-height-ratio. Wide and slightly thickened cell tabs reduce the heat that is inserted into the cells active volume through the Joule losses in the tabs which leads to a lower temperature difference within the cell. Of course, wide channels are beneficial for the cooling, but increase the weight of the system. In terms of minimum weight, bottom cooling is the preferred cooling method while still providing low maximum temperatures and acceptable temperature differences in the cell.

Tab cooling works best on cells with a low width-to-height-ratio as well as wide and thick tabs to reduce the thermal bottleneck in the tabs. With such a cell design, the lowest temperature differences within a cell may be achieved. However, this does not necessarily lead to an advantage for the lifetime of the battery cells as the achievable maximum temperatures are higher compared to the bottom cooling and thus, the equivalent aging temperature of the cell is still higher despite the low temperature difference in the cells active volume.

The combination of both cooling approaches could be an interesting option for applications that need a high cooling performance. At the cost of an increased weight, the combined cooling leads to the lowest maximum temperatures and low temperature differences in the cell. However, this is also the most complex solution for the design of the cooling system. In general, the presented analysis focuses on the thermal effects and influences to evaluate the cooling potentials of the different cooling approaches. Other important aspects towards the real implementation of the identified cell designs are neglected. The thickening of the cell tabs could for example bring new difficulties in the manufacturing of the cells as the welding of the tabs to the electrodes and also the sealing of the pouch bag becomes more challenging.

Overall, the plurality of the possible designs depending on the specific application and their requirements underlines the importance of multidisciplinary and fast simulation models during the design process. With the novel approach, that uses a meta-model based on a neural network, an excellent solution to that issue was demonstrated. The results are accurate and obtained very quickly as demonstrated in the two different optimization scenarios. The model could be easily used in other application scenarios with given optimization objectives and design parameters. Thus, it enables the design of optimized battery systems with an improved thermal management system, leading to faster charging rates, higher energy densities and an increased lifetime.

The key challenge will be to find a good data basis for the training of such models as well as the creation of generally applicable models that cover for example not only one cell format or one specific cell chemistry. Still, it could be an option that cell manufactures provide such models for their cells or provide the data from cell test so that customers could use them to create their individual models.

5 Summary and outlook

Summary

The present thesis deals with the conflict of objectives in the thermal design of battery systems in electric vehicles. This conflict consists between the design requirements "fast charging capability", "long lifetime" and "high energy density". To find an optimal solution, different cooling methods need to be compared, ideally with fast simulation models so that many different variants may be analyzed depending on given constraints.
Among the cooling approaches for pouch cells, tab cooling was identified in the previous years as an interesting alternative compared to the predominant bottom cooling. It reduces the temperature differences within the cell and is consequently able to extend their lifetime. However, tab cooling was mainly analyzed on cell level and no experimental investigations of its performance on module level exist. Also, simulation models of battery modules that enable a fast prediction of the temperature difference within a single cell are not available to optimize the thermal design of a battery module/cell regarding the conflict of objectives and to compare the different cooling approaches.
These knowledge gaps are closed in the present thesis for pouch battery cells. A novel, tab-cooled battery module prototype was developed using thermally conductive plastic materials. The cooling performance of the prototype during a charging process was investigated on a test bench as well as with a validated 1D simulation model. In addition, a novel simulation model was developed that enables the fast an accurate prediction of temperature differences in a single pouch battery cell of a module after a charging process. It is based on a neural network that takes various geometric and thermal parameters as an input and predicts the maximum and minimum temperature occurring in the battery cell after charging it with a constant C-rate. The neural network was trained with data generated by an accurate 3D simulation model. Consequently, it was applied in a generic battery module model to compare tab cooling to bottom cooling approaches and find the optimal thermal design of a battery module/cell depending on the cooling method.
The following findings and conclusions were achieved with the developed demonstrator and the simulation model:

- Realizing a tab cooling system using thermally conductive plastic materials between the cell tabs and the cooling channels is possible. The plastic material is not the limiting factor for a high cooling performance.

- In the battery module prototype, the tabs itself were identified as the thermal bottleneck between the battery cell and the cooling system. In the tested configuration, their thermal resistance is by a factor of 24 to 42 higher than the thermal resistance of the plastic material. As a result, the tab cooling system only lowered the cell temperatures by 2 K compared to the uncooled module during a 2C charging process. Thus, it was shown that tab cooling only works effectively if cell and tab dimensions are specifically adjusted to the thermal design.

- Optimizing the thermal cell design with the novel simulation model shows, that tab cooling works best when the cell has a low width-to-height-ratio and the cross-sectional area of the tabs is high. Then it leads to the lowest temperature differences within a cell but its overall cooling performance is still inferior compared to bottom cooling. Thus, tab cooling seems not to be suitable for the usage in automotive applications where typically cells with a high width-to-height-ratio are used.

- Optimizing the cell dimensions in a battery module for bottom cooling leads to cells with a high width-to-height-ratio as well as wide and slightly thickened cell tabs. Bottom cooling is the best choice if a low weight and a good cooling performance is needed at the cost of the highest temperature differences within the cells.

- Still, the higher temperature differences in a bottom-cooled cell are not necessarily a disadvantage. The advantage of tab cooling with respect to the lifetime vanishes as the cell aging is not only influenced by the temperature difference but also by the average temperature of the cell. As lower average temperatures may be achieved with a bottom cooling system, the lifetime of a bottom-cooled cell might be higher despite a higher temperature difference within the cell. Consequently, bottom cooling is not only because of the cell dimensions a good choice for automotive applications.

- Combining both cooling approaches is complex to realize in practice but enables the highest cooling performances and low temperature differences within the cell. The weight is higher but it could be an attractive solution for special applications that demand a powerful cooling system.

- The novel simulation model to predict the temperature differences in a cell works excellently. The evaluation of the neural network is fast (<1 s) and its accuracy is satisfactory with a MAE of 0.71 K on the prediction of the temperature difference (whereas the average temperature difference within the data set was 10.4 K). Integrated in the 1D generic battery module simulation model, a charging process was simulated in 15 s to 18 s. Thus, extensive design optimization during the development of battery systems are possible and the final selection may be made based on quantified optimization objectives.

Outlook

Both the developed tab cooling design with thermally conductive plastics and the neural-network-based simulation model offer the potential for further improvements and research. Below, the most interesting aspects are listed.

Design of tab cooling systems for pouch cells

- Pouch cells with a one-sided tab design were used in the battery module prototype. That design offers less design space around the tabs and makes the integration of the cooling channels as well as the electrical connection of the cells difficult. The design should be adopted and tested with pouch cells having a butterfly tab design.

- Furthermore, the presented design could be improved regarding its usage and manufacturing in a high-volume application. For instance, a welded connection could be used for the electrical contacting of the tabs instead of the compression approach. This leads to a mechanically stronger connection and less electrical resistances. However, it also brings new challenges as the welding could damage the underlying plastic material.

Fast, meta-model-based simulation model

- The meta-model was entirely trained with data from the 3D simulation model and the occurring temperature differences were solely predicted by that simulated data. Even though these 3D simulation models provide a high accuracy, validating at least some of the data points with experimental data would be beneficial to ensure that the simulated data fits well to reality. This would require several cells with a different geometry but an identical cell chemistry and entails a great deal of effort.

- The proposed cell designs from the optimization contain some challenging parameters for the manufacturing of the pouch battery cells. For example, tab thicknesses in the range of 2 to 5 mm. Further investigations should be performed to check if the proposed designs are feasible for manufacturing and corresponding manufacturing constraints could be integrated in the model.

- Currently, the meta-model is only able to predict the temperature differences within the cell after a charging process with a constant C-rate and averaged boundary heat fluxes. Changing the meta-model to a truly transient model, so that the thermal behavior is predicted for a certain small time step would be an attractive modeling alternative, as this also enables predictions under transient load conditions. A first step in that direction was achieved in an own publication where the average temperature of a battery cell is predicted in such a manner using a nonlinear autoregressive exogenous network [170]. A similar approach could be created for the maximum and minimum temperature within the cell.

- Furthermore, the 1D simulation model including the cell meta-model could be extended to include additional physical effects of relevance. For instance, the lifetime is currently solely evaluated based on the thermal influence. However, as described in section 2.1.3, it depends on further effects that should be considered in the model, for instance the mechanical stresses.

A Appendix

A.1 ECM parameters

All values of the maps for $U_{\mathrm{oc}}(|Cr|, T, SoC)$, $R_{\mathrm{s}}(|Cr|, T, SoC)$ and $\frac{\partial U}{\partial T}(|Cr|, T, SoC)$ are given in the following. As the maps are three-dimensional they are split up for the documentation according to the C-rate. They are displayed as two-dimensional tables for the three different C-rate values.

Tab. A.1: Values of the OCV map $U_{oc}(|Cr| = 1\,h^{-1}, T, SoC)$

SoC	−10 °C	0 °C	10 °C	20 °C	30 °C	40 °C	50 °C	Unit
0.000	3.0000	3.0000	3.0000	3.0000	3.0000	3.0000	3.0000	V
0.001	3.2273	3.2154	3.1973	3.1740	3.1487	3.1250	3.1046	V
0.002	3.3352	3.3128	3.2811	3.2442	3.2078	3.1755	3.1485	V
0.004	3.4245	3.3978	3.3606	3.3181	3.2763	3.2387	3.2070	V
0.006	3.4575	3.4344	3.4007	3.3605	3.3193	3.2814	3.2491	V
0.008	3.4727	3.4542	3.4253	3.3889	3.3503	3.3138	3.2824	V
0.010	3.4811	3.4663	3.4419	3.4096	3.3740	3.3397	3.3100	V
0.015	3.4917	3.4826	3.4663	3.4427	3.4147	3.3867	3.3626	V
0.020	3.4978	3.4909	3.4796	3.4621	3.4405	3.4185	3.3998	V
0.030	3.5106	3.5004	3.4937	3.4836	3.4707	3.4575	3.4468	V
0.040	3.5282	3.5076	3.5016	3.4951	3.4871	3.4792	3.4729	V
0.050	3.5468	3.5161	3.5073	3.5025	3.4971	3.4922	3.4883	V
0.075	3.5812	3.5474	3.5222	3.5148	3.5116	3.5093	3.5076	V
0.100	3.6023	3.5745	3.5477	3.5298	3.5229	3.5202	3.5186	V
0.125	3.6121	3.5974	3.5728	3.5544	3.5440	3.5379	3.5344	V
0.150	3.6192	3.6117	3.5918	3.5782	3.5683	3.5623	3.5588	V
0.175	3.6255	3.6206	3.6114	3.5967	3.5886	3.5847	3.5822	V
0.200	3.6319	3.6273	3.6222	3.6157	3.6095	3.6043	3.6009	V
0.225	3.6388	3.6337	3.6301	3.6264	3.6229	3.6205	3.6188	V
0.250	3.6469	3.6403	3.6368	3.6343	3.6322	3.6305	3.6292	V
0.275	3.6563	3.6474	3.6437	3.6412	3.6394	3.6380	3.6370	V
0.300	3.6671	3.6550	3.6510	3.6483	3.6464	3.6451	3.6440	V
0.325	3.6793	3.6633	3.6590	3.6560	3.6540	3.6525	3.6514	V
0.350	3.6933	3.6726	3.6676	3.6644	3.6622	3.6606	3.6594	V
0.375	3.7109	3.6834	3.6771	3.6736	3.6711	3.6694	3.6681	V
0.400	3.7278	3.6965	3.6873	3.6835	3.6809	3.6790	3.6776	V
0.425	3.7420	3.7124	3.6988	3.6944	3.6915	3.6894	3.6879	V
0.450	3.7557	3.7333	3.7123	3.7062	3.7030	3.7008	3.6991	V
0.475	3.7700	3.7558	3.7300	3.7199	3.7157	3.7131	3.7113	V
0.500	3.7852	3.7732	3.7552	3.7384	3.7312	3.7275	3.7252	V
0.525	3.8013	3.7892	3.7790	3.7657	3.7547	3.7483	3.7445	V
0.550	3.8184	3.8057	3.7970	3.7897	3.7831	3.7777	3.7738	V
0.575	3.8365	3.8231	3.8142	3.8078	3.8031	3.7996	3.7970	V
0.600	3.8556	3.8415	3.8321	3.8255	3.8209	3.8175	3.8150	V
0.625	3.8756	3.8608	3.8509	3.8441	3.8392	3.8357	3.8331	V
0.650	3.8967	3.8811	3.8707	3.8635	3.8584	3.8547	3.8520	V
0.675	3.9187	3.9023	3.8914	3.8839	3.8786	3.8747	3.8718	V
0.700	3.9417	3.9244	3.9131	3.9052	3.8997	3.8956	3.8926	V
0.725	3.9658	3.9475	3.9357	3.9275	3.9217	3.9175	3.9143	V
0.750	3.9883	3.9716	3.9593	3.9507	3.9447	3.9403	3.9370	V
0.775	4.0067	3.9965	3.9837	3.9749	3.9686	3.9640	3.9606	V
0.800	4.0245	4.0225	4.0092	4.0000	3.9934	3.9887	3.9851	V
0.825	4.0426	4.0489	4.0356	4.0260	4.0192	4.0143	4.0106	V
0.850	4.0613	4.0696	4.0630	4.0531	4.0460	4.0409	4.0371	V
0.875	4.0810	4.0887	4.0915	4.0811	4.0738	4.0685	4.0645	V
0.900	4.1019	4.1082	4.1140	4.1103	4.1026	4.0971	4.0930	V
0.925	4.1241	4.1288	4.1338	4.1375	4.1326	4.1269	4.1226	V
0.950	4.1479	4.1509	4.1543	4.1579	4.1603	4.1578	4.1534	V
0.975	4.1558	4.1745	4.1763	4.1781	4.1800	4.1817	4.1825	V
1.000	4.1558	4.1745	4.1849	4.1908	4.1943	4.1963	4.1976	V

Tab. A.2: Values of the OCV map $U_{oc}(|Cr| = 2\,h^{-1}, T, SoC)$

SoC	−10 °C	0 °C	10 °C	20 °C	30 °C	40 °C	50 °C	Unit
0.000	3.0000	3.0000	3.0000	3.0000	3.0000	3.0000	3.0000	V
0.001	3.2339	3.2273	3.2164	3.2001	3.1792	3.1560	3.1334	V
0.002	3.3484	3.3355	3.3148	3.2860	3.2523	3.2182	3.1870	V
0.004	3.4408	3.4256	3.4008	3.3669	3.3279	3.2886	3.2525	V
0.006	3.4717	3.4593	3.4378	3.4071	3.3703	3.3320	3.2958	V
0.008	3.4847	3.4751	3.4578	3.4315	3.3985	3.3627	3.3281	V
0.010	3.4915	3.4840	3.4701	3.4479	3.4187	3.3859	3.3534	V
0.015	3.5024	3.4954	3.4867	3.4719	3.4507	3.4252	3.3988	V
0.020	3.5139	3.5020	3.4953	3.4849	3.4693	3.4496	3.4288	V
0.030	3.5425	3.5153	3.5052	3.4988	3.4896	3.4777	3.4651	V
0.040	3.5674	3.5323	3.5129	3.5067	3.5005	3.4929	3.4851	V
0.050	3.5839	3.5510	3.5220	3.5125	3.5076	3.5023	3.4971	V
0.075	3.6057	3.5857	3.5539	3.5287	3.5197	3.5160	3.5131	V
0.100	3.6171	3.6075	3.5808	3.5549	3.5362	3.5274	3.5238	V
0.125	3.6279	3.6180	3.6036	3.5795	3.5608	3.5494	3.5422	V
0.150	3.6380	3.6256	3.6175	3.5988	3.5839	3.5735	3.5664	V
0.175	3.6481	3.6325	3.6263	3.6170	3.6028	3.5929	3.5882	V
0.200	3.6582	3.6395	3.6333	3.6275	3.6204	3.6140	3.6082	V
0.225	3.6688	3.6473	3.6401	3.6353	3.6307	3.6266	3.6235	V
0.250	3.6800	3.6563	3.6473	3.6422	3.6386	3.6357	3.6334	V
0.275	3.6921	3.6667	3.6549	3.6495	3.6457	3.6430	3.6410	V
0.300	3.7055	3.6783	3.6633	3.6573	3.6532	3.6503	3.6482	V
0.325	3.7211	3.6913	3.6724	3.6658	3.6614	3.6582	3.6559	V
0.350	3.7365	3.7058	3.6827	3.6751	3.6702	3.6668	3.6643	V
0.375	3.7510	3.7230	3.6948	3.6852	3.6799	3.6762	3.6734	V
0.400	3.7656	3.7420	3.7091	3.6962	3.6904	3.6863	3.6834	V
0.425	3.7810	3.7584	3.7261	3.7086	3.7018	3.6974	3.6942	V
0.450	3.7974	3.7738	3.7475	3.7236	3.7144	3.7094	3.7059	V
0.475	3.8148	3.7895	3.7703	3.7428	3.7292	3.7228	3.7188	V
0.500	3.8334	3.8059	3.7887	3.7687	3.7491	3.7393	3.7338	V
0.525	3.8531	3.8233	3.8057	3.7920	3.7772	3.7641	3.7557	V
0.550	3.8703	3.8417	3.8232	3.8105	3.8006	3.7922	3.7853	V
0.575	3.8859	3.8610	3.8416	3.8284	3.8190	3.8121	3.8070	V
0.600	3.9008	3.8813	3.8609	3.8470	3.8373	3.8303	3.8252	V
0.625	3.9156	3.9026	3.8812	3.8666	3.8565	3.8491	3.8438	V
0.650	3.9303	3.9248	3.9024	3.8872	3.8765	3.8688	3.8632	V
0.675	3.9452	3.9480	3.9245	3.9087	3.8975	3.8895	3.8836	V
0.700	3.9603	3.9706	3.9476	3.9311	3.9195	3.9111	3.9049	V
0.725	3.9756	3.9888	3.9717	3.9545	3.9424	3.9336	3.9272	V
0.750	3.9914	4.0051	3.9966	3.9788	3.9662	3.9571	3.9504	V
0.775	4.0077	4.0211	4.0226	4.0040	3.9909	3.9815	3.9745	V
0.800	4.0247	4.0372	4.0450	4.0302	4.0166	4.0068	3.9996	V
0.825	4.0425	4.0537	4.0634	4.0574	4.0433	4.0331	4.0256	V
0.850	4.0612	4.0709	4.0803	4.0843	4.0710	4.0604	4.0526	V
0.875	4.0809	4.0890	4.0974	4.1042	4.0997	4.0888	4.0807	V
0.900	4.1019	4.1083	4.1152	4.1218	4.1252	4.1182	4.1098	V
0.925	4.1211	4.1289	4.1341	4.1394	4.1442	4.1460	4.1400	V
0.950	4.1211	4.1511	4.1544	4.1581	4.1617	4.1650	4.1663	V
0.975	4.1211	4.1525	4.1712	4.1782	4.1801	4.1819	4.1836	V
1.000	4.1211	4.1525	4.1712	4.1822	4.1888	4.1927	4.1952	V

Tab. A.3: Values of the OCV map $U_{oc}(|Cr| = 3\,h^{-1}, T, SoC)$

SoC	−10 °C	0 °C	10 °C	20 °C	30 °C	40 °C	50 °C	Unit
0.000	3.0000	3.0000	3.0000	3.0000	3.0000	3.0000	3.0000	V
0.001	3.2361	3.2317	3.2239	3.2117	3.1946	3.1738	3.1516	V
0.002	3.3531	3.3442	3.3290	3.3064	3.2770	3.2444	3.2123	V
0.004	3.4467	3.4363	3.4183	3.3913	3.3568	3.3191	3.2821	V
0.006	3.4769	3.4687	3.4536	3.4298	3.3981	3.3622	3.3258	V
0.008	3.4894	3.4831	3.4713	3.4515	3.4239	3.3912	3.3571	V
0.010	3.4963	3.4909	3.4815	3.4654	3.4417	3.4124	3.3809	V
0.015	3.5110	3.5015	3.4950	3.4847	3.4684	3.4466	3.4217	V
0.020	3.5275	3.5106	3.5023	3.4948	3.4832	3.4669	3.4475	V
0.030	3.5632	3.5317	3.5131	3.5061	3.4991	3.4893	3.4775	V
0.040	3.5847	3.5553	3.5254	3.5134	3.5078	3.5014	3.4937	V
0.050	3.5965	3.5748	3.5412	3.5205	3.5140	3.5090	3.5037	V
0.075	3.6164	3.6042	3.5770	3.5473	3.5278	3.5214	3.5178	V
0.100	3.6312	3.6176	3.6031	3.5756	3.5517	3.5359	3.5289	V
0.125	3.6435	3.6269	3.6183	3.5970	3.5766	3.5601	3.5500	V
0.150	3.6549	3.6358	3.6275	3.6166	3.5959	3.5838	3.5740	V
0.175	3.6664	3.6455	3.6350	3.6276	3.6166	3.6021	3.5939	V
0.200	3.6784	3.6561	3.6423	3.6357	3.6286	3.6214	3.6148	V
0.225	3.6913	3.6672	3.6500	3.6430	3.6375	3.6324	3.6281	V
0.250	3.7053	3.6791	3.6582	3.6504	3.6449	3.6407	3.6375	V
0.275	3.7205	3.6918	3.6676	3.6584	3.6524	3.6481	3.6450	V
0.300	3.7352	3.7055	3.6784	3.6671	3.6605	3.6559	3.6525	V
0.325	3.7486	3.7208	3.6909	3.6765	3.6693	3.6642	3.6606	V
0.350	3.7623	3.7386	3.7049	3.6868	3.6789	3.6734	3.6694	V
0.375	3.7761	3.7559	3.7206	3.6983	3.6893	3.6833	3.6790	V
0.400	3.7903	3.7721	3.7387	3.7117	3.7006	3.6941	3.6894	V
0.425	3.8056	3.7883	3.7601	3.7276	3.7131	3.7058	3.7008	V
0.450	3.8207	3.8050	3.7796	3.7467	3.7275	3.7186	3.7131	V
0.475	3.8346	3.8225	3.7970	3.7710	3.7456	3.7333	3.7266	V
0.500	3.8480	3.8411	3.8143	3.7941	3.7702	3.7526	3.7431	V
0.525	3.8615	3.8606	3.8322	3.8129	3.7968	3.7804	3.7675	V
0.550	3.8751	3.8812	3.8511	3.8311	3.8169	3.8057	3.7964	V
0.575	3.8888	3.9024	3.8709	3.8500	3.8354	3.8249	3.8171	V
0.600	3.9027	3.9188	3.8916	3.8697	3.8545	3.8436	3.8357	V
0.625	3.9167	3.9345	3.9133	3.8904	3.8744	3.8631	3.8547	V
0.650	3.9310	3.9491	3.9360	3.9120	3.8953	3.8834	3.8747	V
0.675	3.9456	3.9634	3.9596	3.9346	3.9172	3.9047	3.8956	V
0.700	3.9604	3.9777	3.9841	3.9581	3.9400	3.9270	3.9175	V
0.725	3.9757	3.9921	4.0026	3.9825	3.9637	3.9502	3.9403	V
0.750	3.9915	4.0068	4.0195	4.0079	3.9884	3.9743	3.9640	V
0.775	4.0078	4.0218	4.0348	4.0343	4.0140	3.9994	3.9887	V
0.800	4.0248	4.0374	4.0499	4.0561	4.0406	4.0254	4.0143	V
0.825	4.0426	4.0537	4.0652	4.0743	4.0681	4.0524	4.0409	V
0.850	4.0613	4.0709	4.0810	4.0902	4.0936	4.0805	4.0685	V
0.875	4.0811	4.0890	4.0976	4.1060	4.1122	4.1095	4.0971	V
0.900	4.0927	4.1083	4.1152	4.1223	4.1287	4.1318	4.1268	V
0.925	4.0927	4.1290	4.1342	4.1395	4.1449	4.1496	4.1512	V
0.950	4.0927	4.1332	4.1546	4.1581	4.1618	4.1654	4.1685	V
0.975	4.0927	4.1332	4.1586	4.1741	4.1801	4.1819	4.1837	V
1.000	4.0927	4.1332	4.1586	4.1741	4.1835	4.1893	4.1929	V

Tab. A.4: Values of the resistance map $R_s(|Cr| = 1\,\mathrm{h}^{-1}, T, SoC)$

SoC	−10 °C	0 °C	10 °C	20 °C	30 °C	40 °C	50 °C	Unit
0.000	1.3917×10^{-2}	1.0900×10^{-2}	8.5332×10^{-3}	6.6670×10^{-3}	5.1468×10^{-3}	3.8820×10^{-3}	2.8505×10^{-3}	VA^{-1}
0.001	1.2973×10^{-2}	9.9784×10^{-3}	7.6786×10^{-3}	5.9126×10^{-3}	4.5164×10^{-3}	3.3891×10^{-3}	2.4936×10^{-3}	VA^{-1}
0.002	1.2554×10^{-2}	9.6084×10^{-3}	7.3704×10^{-3}	5.6594×10^{-3}	4.3052×10^{-3}	3.2154×10^{-3}	2.3583×10^{-3}	VA^{-1}
0.004	1.2146×10^{-2}	9.2579×10^{-3}	7.0660×10^{-3}	5.3803×10^{-3}	4.0495×10^{-3}	2.9966×10^{-3}	2.1860×10^{-3}	VA^{-1}
0.006	1.1941×10^{-2}	9.0714×10^{-3}	6.8810×10^{-3}	5.1942×10^{-3}	3.8760×10^{-3}	2.8492×10^{-3}	2.0689×10^{-3}	VA^{-1}
0.008	1.1815×10^{-2}	8.9418×10^{-3}	6.7396×10^{-3}	5.0500×10^{-3}	3.7436×10^{-3}	2.7369×10^{-3}	1.9786×10^{-3}	VA^{-1}
0.010	1.1726×10^{-2}	8.8382×10^{-3}	6.6220×10^{-3}	4.9318×10^{-3}	3.6363×10^{-3}	2.6456×10^{-3}	1.9044×10^{-3}	VA^{-1}
0.015	1.1573×10^{-2}	8.6316×10^{-3}	6.3896×10^{-3}	4.7056×10^{-3}	3.4320×10^{-3}	2.4705×10^{-3}	1.7607×10^{-3}	VA^{-1}
0.020	1.1467×10^{-2}	8.4649×10^{-3}	6.2123×10^{-3}	4.5375×10^{-3}	3.2800×10^{-3}	2.3394×10^{-3}	1.6526×10^{-3}	VA^{-1}
0.030	1.1332×10^{-2}	8.2038×10^{-3}	5.9499×10^{-3}	4.2909×10^{-3}	3.0563×10^{-3}	2.1463×10^{-3}	1.4951×10^{-3}	VA^{-1}
0.040	1.1193×10^{-2}	8.0126×10^{-3}	5.7567×10^{-3}	4.1090×10^{-3}	2.8913×10^{-3}	2.0054×10^{-3}	1.3831×10^{-3}	VA^{-1}
0.050	1.1054×10^{-2}	7.8684×10^{-3}	5.6036×10^{-3}	3.9641×10^{-3}	2.7603×10^{-3}	1.8956×10^{-3}	1.2981×10^{-3}	VA^{-1}
0.075	1.0778×10^{-2}	7.5807×10^{-3}	5.3244×10^{-3}	3.6932×10^{-3}	2.5191×10^{-3}	1.7004×10^{-3}	1.1514×10^{-3}	VA^{-1}
0.100	1.0539×10^{-2}	7.3664×10^{-3}	5.1172×10^{-3}	3.4994×10^{-3}	2.3504×10^{-3}	1.5692×10^{-3}	1.0556×10^{-3}	VA^{-1}
0.125	1.0364×10^{-2}	7.2062×10^{-3}	4.9535×10^{-3}	3.3467×10^{-3}	2.2242×10^{-3}	1.4742×10^{-3}	9.8756×10^{-4}	VA^{-1}
0.150	1.0240×10^{-2}	7.0674×10^{-3}	4.8223×10^{-3}	3.2239×10^{-3}	2.1247×10^{-3}	1.4007×10^{-3}	9.3554×10^{-4}	VA^{-1}
0.175	1.0149×10^{-2}	6.9539×10^{-3}	4.7096×10^{-3}	3.1246×10^{-3}	2.0447×10^{-3}	1.3426×10^{-3}	8.9481×10^{-4}	VA^{-1}
0.200	1.0078×10^{-2}	6.8621×10^{-3}	4.6162×10^{-3}	3.0403×10^{-3}	1.9801×10^{-3}	1.2962×10^{-3}	8.6244×10^{-4}	VA^{-1}
0.225	1.0033×10^{-2}	6.7876×10^{-3}	4.5362×10^{-3}	2.9705×10^{-3}	1.9260×10^{-3}	1.2576×10^{-3}	8.3566×10^{-4}	VA^{-1}
0.250	1.0011×10^{-2}	6.7259×10^{-3}	4.4697×10^{-3}	2.9113×10^{-3}	1.8811×10^{-3}	1.2259×10^{-3}	8.1371×10^{-4}	VA^{-1}
0.275	1.0001×10^{-2}	6.6747×10^{-3}	4.4138×10^{-3}	2.8618×10^{-3}	1.8433×10^{-3}	1.1992×10^{-3}	7.9530×10^{-4}	VA^{-1}
0.300	9.9956×10^{-3}	6.6328×10^{-3}	4.3667×10^{-3}	2.8202×10^{-3}	1.8118×10^{-3}	1.1770×10^{-3}	7.8000×10^{-4}	VA^{-1}
0.325	9.9907×10^{-3}	6.5995×10^{-3}	4.3274×10^{-3}	2.7853×10^{-3}	1.7854×10^{-3}	1.1584×10^{-3}	7.6718×10^{-4}	VA^{-1}
0.350	9.9818×10^{-3}	6.5763×10^{-3}	4.2951×10^{-3}	2.7563×10^{-3}	1.7634×10^{-3}	1.1429×10^{-3}	7.5649×10^{-4}	VA^{-1}
0.375	9.9619×10^{-3}	6.5663×10^{-3}	4.2693×10^{-3}	2.7325×10^{-3}	1.7452×10^{-3}	1.1301×10^{-3}	7.4762×10^{-4}	VA^{-1}
0.400	9.9346×10^{-3}	6.5637×10^{-3}	4.2497×10^{-3}	2.7135×10^{-3}	1.7305×10^{-3}	1.1197×10^{-3}	7.4040×10^{-4}	VA^{-1}
0.425	9.9336×10^{-3}	6.5619×10^{-3}	4.2371×10^{-3}	2.6990×10^{-3}	1.7190×10^{-3}	1.1114×10^{-3}	7.3466×10^{-4}	VA^{-1}
0.450	9.9558×10^{-3}	6.5622×10^{-3}	4.2337×10^{-3}	2.6891×10^{-3}	1.7105×10^{-3}	1.1052×10^{-3}	7.3032×10^{-4}	VA^{-1}
0.475	9.9919×10^{-3}	6.5585×10^{-3}	4.2334×10^{-3}	2.6852×10^{-3}	1.7054×10^{-3}	1.1011×10^{-3}	7.2733×10^{-4}	VA^{-1}
0.500	1.0038×10^{-2}	6.5605×10^{-3}	4.2353×10^{-3}	2.6858×10^{-3}	1.7047×10^{-3}	1.0999×10^{-3}	7.2628×10^{-4}	VA^{-1}
0.525	1.0095×10^{-2}	6.5786×10^{-3}	4.2368×10^{-3}	2.6868×10^{-3}	1.7056×10^{-3}	1.1008×10^{-3}	7.2700×10^{-4}	VA^{-1}
0.550	1.0161×10^{-2}	6.6070×10^{-3}	4.2453×10^{-3}	2.6885×10^{-3}	1.7055×10^{-3}	1.1002×10^{-3}	7.2613×10^{-4}	VA^{-1}
0.575	1.0239×10^{-2}	6.6436×10^{-3}	4.2630×10^{-3}	2.6961×10^{-3}	1.7087×10^{-3}	1.1016×10^{-3}	7.2687×10^{-4}	VA^{-1}
0.600	1.0330×10^{-2}	6.6885×10^{-3}	4.2875×10^{-3}	2.7094×10^{-3}	1.7161×10^{-3}	1.1058×10^{-3}	7.2948×10^{-4}	VA^{-1}
0.625	1.0435×10^{-2}	6.7423×10^{-3}	4.3184×10^{-3}	2.7274×10^{-3}	1.7266×10^{-3}	1.1122×10^{-3}	7.3352×10^{-4}	VA^{-1}
0.650	1.0557×10^{-2}	6.8058×10^{-3}	4.3562×10^{-3}	2.7500×10^{-3}	1.7403×10^{-3}	1.1206×10^{-3}	7.3890×10^{-4}	VA^{-1}
0.675	1.0698×10^{-2}	6.8812×10^{-3}	4.4018×10^{-3}	2.7778×10^{-3}	1.7573×10^{-3}	1.1312×10^{-3}	7.4570×10^{-4}	VA^{-1}
0.700	1.0862×10^{-2}	6.9699×10^{-3}	4.4566×10^{-3}	2.8118×10^{-3}	1.7782×10^{-3}	1.1443×10^{-3}	7.5412×10^{-4}	VA^{-1}
0.725	1.1052×10^{-2}	7.0732×10^{-3}	4.5214×10^{-3}	2.8525×10^{-3}	1.8035×10^{-3}	1.1603×10^{-3}	7.6443×10^{-4}	VA^{-1}
0.750	1.1750×10^{-2}	7.1938×10^{-3}	4.5976×10^{-3}	2.9007×10^{-3}	1.8337×10^{-3}	1.1794×10^{-3}	7.7678×10^{-4}	VA^{-1}
0.775	1.2605×10^{-2}	7.3355×10^{-3}	4.6874×10^{-3}	2.9579×10^{-3}	1.8696×10^{-3}	1.2021×10^{-3}	7.9148×10^{-4}	VA^{-1}
0.800	1.3491×10^{-2}	7.5033×10^{-3}	4.7939×10^{-3}	3.0258×10^{-3}	1.9123×10^{-3}	1.2291×10^{-3}	8.0903×10^{-4}	VA^{-1}
0.825	1.4471×10^{-2}	7.7725×10^{-3}	4.9212×10^{-3}	3.1071×10^{-3}	1.9636×10^{-3}	1.2616×10^{-3}	8.3005×10^{-4}	VA^{-1}
0.850	1.5576×10^{-2}	8.5191×10^{-3}	5.0754×10^{-3}	3.2056×10^{-3}	2.0256×10^{-3}	1.3009×10^{-3}	8.5547×10^{-4}	VA^{-1}
0.875	1.6830×10^{-2}	9.2290×10^{-3}	5.2656×10^{-3}	3.3266×10^{-3}	2.1017×10^{-3}	1.3490×10^{-3}	8.8656×10^{-4}	VA^{-1}
0.900	1.8248×10^{-2}	1.0001×10^{-2}	5.7610×10^{-3}	3.4793×10^{-3}	2.1974×10^{-3}	1.4093×10^{-3}	9.2536×10^{-4}	VA^{-1}
0.925	1.9829×10^{-2}	1.0852×10^{-2}	6.2452×10^{-3}	3.7334×10^{-3}	2.3217×10^{-3}	1.4871×10^{-3}	9.7525×10^{-4}	VA^{-1}
0.950	2.1540×10^{-2}	1.1782×10^{-2}	6.7605×10^{-3}	4.0457×10^{-3}	2.5043×10^{-3}	1.5930×10^{-3}	1.0425×10^{-3}	VA^{-1}
0.975	2.2099×10^{-2}	1.2768×10^{-2}	7.3259×10^{-3}	4.3736×10^{-3}	2.7072×10^{-3}	1.7306×10^{-3}	1.1365×10^{-3}	VA^{-1}
1.000	2.2099×10^{-2}	1.2768×10^{-2}	7.5518×10^{-3}	4.5908×10^{-3}	2.8705×10^{-3}	1.8449×10^{-3}	1.2172×10^{-3}	VA^{-1}

Tab. A.5: Values of the resistance map $R_s(|Cr| = 2\,\mathrm{h}^{-1}, T, SoC)$

SoC	−10 °C	0 °C	10 °C	20 °C	30 °C	40 °C	50 °C	Unit
0.000	9.2813×10^{-3}	7.3997×10^{-3}	5.9144×10^{-3}	4.7323×10^{-3}	3.7896×10^{-3}	3.0172×10^{-3}	2.3662×10^{-3}	VA^{-1}
0.001	8.8107×10^{-3}	6.9091×10^{-3}	5.4327×10^{-3}	4.2806×10^{-3}	3.3831×10^{-3}	2.6666×10^{-3}	2.0780×10^{-3}	VA^{-1}
0.002	8.5758×10^{-3}	6.6882×10^{-3}	5.2362×10^{-3}	4.1148×10^{-3}	3.2454×10^{-3}	2.5502×10^{-3}	1.9790×10^{-3}	VA^{-1}
0.004	8.3310×10^{-3}	6.4709×10^{-3}	5.0495×10^{-3}	3.9534×10^{-3}	3.0981×10^{-3}	2.4123×10^{-3}	1.8543×10^{-3}	VA^{-1}
0.006	8.2029×10^{-3}	6.3621×10^{-3}	4.9517×10^{-3}	3.8579×10^{-3}	3.0011×10^{-3}	2.3178×10^{-3}	1.7692×10^{-3}	VA^{-1}
0.008	8.1265×10^{-3}	6.2958×10^{-3}	4.8853×10^{-3}	3.7859×10^{-3}	2.9255×10^{-3}	2.2449×10^{-3}	1.7042×10^{-3}	VA^{-1}
0.010	8.0791×10^{-3}	6.2500×10^{-3}	4.8332×10^{-3}	3.7260×10^{-3}	2.8629×10^{-3}	2.1856×10^{-3}	1.6513×10^{-3}	VA^{-1}
0.015	8.0507×10^{-3}	6.1739×10^{-3}	4.7304×10^{-3}	3.6065×10^{-3}	2.7419×10^{-3}	2.0722×10^{-3}	1.5500×10^{-3}	VA^{-1}
0.020	8.0872×10^{-3}	6.1227×10^{-3}	4.6470×10^{-3}	3.5138×10^{-3}	2.6514×10^{-3}	1.9878×10^{-3}	1.4741×10^{-3}	VA^{-1}
0.030	8.1354×10^{-3}	6.0618×10^{-3}	4.5139×10^{-3}	3.3751×10^{-3}	2.5183×10^{-3}	1.8634×10^{-3}	1.3620×10^{-3}	VA^{-1}
0.040	8.1608×10^{-3}	5.9962×10^{-3}	4.4159×10^{-3}	3.2726×10^{-3}	2.4201×10^{-3}	1.7714×10^{-3}	1.2794×10^{-3}	VA^{-1}
0.050	8.1548×10^{-3}	5.9260×10^{-3}	4.3414×10^{-3}	3.1915×10^{-3}	2.3418×10^{-3}	1.6981×10^{-3}	1.2145×10^{-3}	VA^{-1}
0.075	8.0407×10^{-3}	5.7826×10^{-3}	4.1899×10^{-3}	3.0447×10^{-3}	2.1952×10^{-3}	1.5616×10^{-3}	1.0971×10^{-3}	VA^{-1}
0.100	7.9783×10^{-3}	5.6576×10^{-3}	4.0772×10^{-3}	2.9343×10^{-3}	2.0899×10^{-3}	1.4648×10^{-3}	1.0168×10^{-3}	VA^{-1}
0.125	7.9771×10^{-3}	5.5660×10^{-3}	3.9931×10^{-3}	2.8470×10^{-3}	2.0058×10^{-3}	1.3910×10^{-3}	9.5781×10^{-4}	VA^{-1}
0.150	7.9868×10^{-3}	5.5017×10^{-3}	3.9209×10^{-3}	2.7784×10^{-3}	1.9376×10^{-3}	1.3323×10^{-3}	9.1171×10^{-4}	VA^{-1}
0.175	7.9910×10^{-3}	5.4557×10^{-3}	3.8622×10^{-3}	2.7181×10^{-3}	1.8827×10^{-3}	1.2848×10^{-3}	8.7500×10^{-4}	VA^{-1}
0.200	7.9904×10^{-3}	5.4215×10^{-3}	3.8155×10^{-3}	2.6688×10^{-3}	1.8354×10^{-3}	1.2463×10^{-3}	8.4571×10^{-4}	VA^{-1}
0.225	7.9884×10^{-3}	5.4014×10^{-3}	3.7781×10^{-3}	2.6267×10^{-3}	1.7965×10^{-3}	1.2140×10^{-3}	8.2125×10^{-4}	VA^{-1}
0.250	7.9871×10^{-3}	5.3932×10^{-3}	3.7473×10^{-3}	2.5919×10^{-3}	1.7634×10^{-3}	1.1870×10^{-3}	8.0112×10^{-4}	VA^{-1}
0.275	7.9873×10^{-3}	5.3907×10^{-3}	3.7219×10^{-3}	2.5627×10^{-3}	1.7358×10^{-3}	1.1645×10^{-3}	7.8428×10^{-4}	VA^{-1}
0.300	7.9880×10^{-3}	5.3904×10^{-3}	3.7015×10^{-3}	2.5382×10^{-3}	1.7125×10^{-3}	1.1456×10^{-3}	7.7021×10^{-4}	VA^{-1}
0.325	7.9852×10^{-3}	5.3901×10^{-3}	3.6857×10^{-3}	2.5179×10^{-3}	1.6931×10^{-3}	1.1298×10^{-3}	7.5844×10^{-4}	VA^{-1}
0.350	7.9980×10^{-3}	5.3880×10^{-3}	3.6765×10^{-3}	2.5013×10^{-3}	1.6769×10^{-3}	1.1166×10^{-3}	7.4862×10^{-4}	VA^{-1}
0.375	8.0370×10^{-3}	5.3816×10^{-3}	3.6740×10^{-3}	2.4883×10^{-3}	1.6638×10^{-3}	1.1058×10^{-3}	7.4052×10^{-4}	VA^{-1}
0.400	8.0942×10^{-3}	5.3686×10^{-3}	3.6743×10^{-3}	2.4787×10^{-3}	1.6534×10^{-3}	1.0971×10^{-3}	7.3395×10^{-4}	VA^{-1}
0.425	8.1632×10^{-3}	5.3654×10^{-3}	3.6748×10^{-3}	2.4737×10^{-3}	1.6456×10^{-3}	1.0903×10^{-3}	7.2880×10^{-4}	VA^{-1}
0.450	8.2407×10^{-3}	5.3766×10^{-3}	3.6761×10^{-3}	2.4735×10^{-3}	1.6407×10^{-3}	1.0854×10^{-3}	7.2494×10^{-4}	VA^{-1}
0.475	8.3263×10^{-3}	5.3968×10^{-3}	3.6742×10^{-3}	2.4739×10^{-3}	1.6395×10^{-3}	1.0826×10^{-3}	7.2244×10^{-4}	VA^{-1}
0.500	8.4205×10^{-3}	5.4232×10^{-3}	3.6764×10^{-3}	2.4760×10^{-3}	1.6400×10^{-3}	1.0826×10^{-3}	7.2183×10^{-4}	VA^{-1}
0.525	8.5240×10^{-3}	5.4551×10^{-3}	3.6877×10^{-3}	2.4772×10^{-3}	1.6412×10^{-3}	1.0832×10^{-3}	7.2248×10^{-4}	VA^{-1}
0.550	8.9037×10^{-3}	5.4926×10^{-3}	3.7048×10^{-3}	2.4831×10^{-3}	1.6427×10^{-3}	1.0836×10^{-3}	7.2230×10^{-4}	VA^{-1}
0.575	9.2702×10^{-3}	5.5360×10^{-3}	3.7265×10^{-3}	2.4943×10^{-3}	1.6479×10^{-3}	1.0859×10^{-3}	7.2335×10^{-4}	VA^{-1}
0.600	9.5885×10^{-3}	5.5862×10^{-3}	3.7527×10^{-3}	2.5093×10^{-3}	1.6565×10^{-3}	1.0908×10^{-3}	7.2629×10^{-4}	VA^{-1}
0.625	9.9333×10^{-3}	5.6449×10^{-3}	3.7837×10^{-3}	2.5278×10^{-3}	1.6678×10^{-3}	1.0978×10^{-3}	7.3062×10^{-4}	VA^{-1}
0.650	1.0316×10^{-2}	5.7136×10^{-3}	3.8210×10^{-3}	2.5504×10^{-3}	1.6818×10^{-3}	1.1066×10^{-3}	7.3625×10^{-4}	VA^{-1}
0.675	1.0748×10^{-2}	5.7925×10^{-3}	3.8652×10^{-3}	2.5780×10^{-3}	1.6992×10^{-3}	1.1176×10^{-3}	7.4330×10^{-4}	VA^{-1}
0.700	1.1230×10^{-2}	5.9781×10^{-3}	3.9167×10^{-3}	2.6111×10^{-3}	1.7206×10^{-3}	1.1312×10^{-3}	7.5212×10^{-4}	VA^{-1}
0.725	1.1773×10^{-2}	6.4165×10^{-3}	3.9767×10^{-3}	2.6497×10^{-3}	1.7459×10^{-3}	1.1477×10^{-3}	7.6286×10^{-4}	VA^{-1}
0.750	1.2387×10^{-2}	6.7974×10^{-3}	4.0470×10^{-3}	2.6953×10^{-3}	1.7758×10^{-3}	1.1672×10^{-3}	7.7563×10^{-4}	VA^{-1}
0.775	1.3084×10^{-2}	7.2058×10^{-3}	4.1301×10^{-3}	2.7491×10^{-3}	1.8113×10^{-3}	1.1904×10^{-3}	7.9081×10^{-4}	VA^{-1}
0.800	1.3877×10^{-2}	7.6526×10^{-3}	4.3841×10^{-3}	2.8134×10^{-3}	1.8536×10^{-3}	1.2181×10^{-3}	8.0895×10^{-4}	VA^{-1}
0.825	1.4787×10^{-2}	8.1565×10^{-3}	4.7249×10^{-3}	2.8908×10^{-3}	1.9046×10^{-3}	1.2514×10^{-3}	8.3074×10^{-4}	VA^{-1}
0.850	1.5831×10^{-2}	8.7236×10^{-3}	5.0588×10^{-3}	3.0103×10^{-3}	1.9667×10^{-3}	1.2919×10^{-3}	8.5721×10^{-4}	VA^{-1}
0.875	1.7030×10^{-2}	9.3678×10^{-3}	5.4237×10^{-3}	3.2701×10^{-3}	2.0440×10^{-3}	1.3421×10^{-3}	8.8984×10^{-4}	VA^{-1}
0.900	1.8396×10^{-2}	1.0100×10^{-2}	5.8280×10^{-3}	3.5113×10^{-3}	2.1751×10^{-3}	1.4059×10^{-3}	9.3106×10^{-4}	VA^{-1}
0.925	1.9717×10^{-2}	1.0924×10^{-2}	6.2796×10^{-3}	3.7690×10^{-3}	2.3463×10^{-3}	1.4963×10^{-3}	9.8523×10^{-4}	VA^{-1}
0.950	1.9717×10^{-2}	1.1829×10^{-2}	6.7825×10^{-3}	4.0552×10^{-3}	2.5164×10^{-3}	1.6127×10^{-3}	1.0595×10^{-3}	VA^{-1}
0.975	1.9717×10^{-2}	1.1883×10^{-2}	7.2016×10^{-3}	4.3778×10^{-3}	2.7091×10^{-3}	1.7318×10^{-3}	1.1395×10^{-3}	VA^{-1}
1.000	1.9717×10^{-2}	1.1883×10^{-2}	7.2016×10^{-3}	4.4439×10^{-3}	2.8061×10^{-3}	1.8154×10^{-3}	1.2031×10^{-3}	VA^{-1}

Tab. A.6: Values of the resistance map $R_s(|Cr| = 3\,\mathrm{h}^{-1}, T, SoC)$

SoC	−10 °C	0 °C	10 °C	20 °C	30 °C	40 °C	50 °C	Unit
0.000	7.3043×10^{-3}	5.8467×10^{-3}	4.7198×10^{-3}	3.8175×10^{-3}	3.0943×10^{-3}	2.5098×10^{-3}	2.0236×10^{-3}	VA^{-1}
0.001	7.0085×10^{-3}	5.5179×10^{-3}	4.3854×10^{-3}	3.4936×10^{-3}	2.7931×10^{-3}	2.2399×10^{-3}	1.7906×10^{-3}	VA^{-1}
0.002	6.8437×10^{-3}	5.3597×10^{-3}	4.2390×10^{-3}	3.3654×10^{-3}	2.6853×10^{-3}	2.1495×10^{-3}	1.7132×10^{-3}	VA^{-1}
0.004	6.6616×10^{-3}	5.1970×10^{-3}	4.0964×10^{-3}	3.2433×10^{-3}	2.5782×10^{-3}	2.0503×10^{-3}	1.6199×10^{-3}	VA^{-1}
0.006	6.5587×10^{-3}	5.1132×10^{-3}	4.0243×10^{-3}	3.1773×10^{-3}	2.5128×10^{-3}	1.9840×10^{-3}	1.5556×10^{-3}	VA^{-1}
0.008	6.4953×10^{-3}	5.0631×10^{-3}	3.9792×10^{-3}	3.1309×10^{-3}	2.4627×10^{-3}	1.9322×10^{-3}	1.5059×10^{-3}	VA^{-1}
0.010	6.4602×10^{-3}	5.0309×10^{-3}	3.9467×10^{-3}	3.0937×10^{-3}	2.4209×10^{-3}	1.8893×10^{-3}	1.4654×10^{-3}	VA^{-1}
0.015	6.4808×10^{-3}	4.9920×10^{-3}	3.8886×10^{-3}	3.0194×10^{-3}	2.3380×10^{-3}	1.8066×10^{-3}	1.3880×10^{-3}	VA^{-1}
0.020	6.5301×10^{-3}	4.9938×10^{-3}	3.8441×10^{-3}	2.9597×10^{-3}	2.2743×10^{-3}	1.7449×10^{-3}	1.3302×10^{-3}	VA^{-1}
0.030	6.6136×10^{-3}	5.0038×10^{-3}	3.7781×10^{-3}	2.8660×10^{-3}	2.1799×10^{-3}	1.6541×10^{-3}	1.2450×10^{-3}	VA^{-1}
0.040	6.6800×10^{-3}	4.9871×10^{-3}	3.7276×10^{-3}	2.7957×10^{-3}	2.1102×10^{-3}	1.5871×10^{-3}	1.1819×10^{-3}	VA^{-1}
0.050	6.7256×10^{-3}	4.9646×10^{-3}	3.6768×10^{-3}	2.7424×10^{-3}	2.0547×10^{-3}	1.5335×10^{-3}	1.1316×10^{-3}	VA^{-1}
0.075	6.8962×10^{-3}	4.8715×10^{-3}	3.5704×10^{-3}	2.6408×10^{-3}	1.9529×10^{-3}	1.4330×10^{-3}	1.0382×10^{-3}	VA^{-1}
0.100	7.0419×10^{-3}	4.7890×10^{-3}	3.4956×10^{-3}	2.5635×10^{-3}	1.8777×10^{-3}	1.3606×10^{-3}	9.7206×10^{-4}	VA^{-1}
0.125	7.1245×10^{-3}	4.7380×10^{-3}	3.4316×10^{-3}	2.5056×10^{-3}	1.8177×10^{-3}	1.3030×10^{-3}	9.2185×10^{-4}	VA^{-1}
0.150	7.1922×10^{-3}	4.7191×10^{-3}	3.3835×10^{-3}	2.4558×10^{-3}	1.7691×10^{-3}	1.2565×10^{-3}	8.8189×10^{-4}	VA^{-1}
0.175	7.2703×10^{-3}	4.7162×10^{-3}	3.3484×10^{-3}	2.4159×10^{-3}	1.7287×10^{-3}	1.2190×10^{-3}	8.4962×10^{-4}	VA^{-1}
0.200	7.3648×10^{-3}	4.7179×10^{-3}	3.3218×10^{-3}	2.3825×10^{-3}	1.6947×10^{-3}	1.1871×10^{-3}	8.2362×10^{-4}	VA^{-1}
0.225	7.4773×10^{-3}	4.7193×10^{-3}	3.3009×10^{-3}	2.3558×10^{-3}	1.6659×10^{-3}	1.1609×10^{-3}	8.0188×10^{-4}	VA^{-1}
0.250	7.6108×10^{-3}	4.7192×10^{-3}	3.2850×10^{-3}	2.3338×10^{-3}	1.6419×10^{-3}	1.1387×10^{-3}	7.8382×10^{-4}	VA^{-1}
0.275	7.7720×10^{-3}	4.7177×10^{-3}	3.2761×10^{-3}	2.3155×10^{-3}	1.6219×10^{-3}	1.1202×10^{-3}	7.6873×10^{-4}	VA^{-1}
0.300	7.9764×10^{-3}	4.7151×10^{-3}	3.2732×10^{-3}	2.3006×10^{-3}	1.6051×10^{-3}	1.1047×10^{-3}	7.5611×10^{-4}	VA^{-1}
0.325	8.1947×10^{-3}	4.7109×10^{-3}	3.2732×10^{-3}	2.2886×10^{-3}	1.5911×10^{-3}	1.0917×10^{-3}	7.4554×10^{-4}	VA^{-1}
0.350	8.2867×10^{-3}	4.7023×10^{-3}	3.2743×10^{-3}	2.2794×10^{-3}	1.5797×10^{-3}	1.0809×10^{-3}	7.3674×10^{-4}	VA^{-1}
0.375	8.3520×10^{-3}	4.6989×10^{-3}	3.2755×10^{-3}	2.2741×10^{-3}	1.5706×10^{-3}	1.0721×10^{-3}	7.2950×10^{-4}	VA^{-1}
0.400	8.4212×10^{-3}	4.7095×10^{-3}	3.2754×10^{-3}	2.2732×10^{-3}	1.5637×10^{-3}	1.0651×10^{-3}	7.2368×10^{-4}	VA^{-1}
0.425	8.5132×10^{-3}	4.7309×10^{-3}	3.2721×10^{-3}	2.2741×10^{-3}	1.5594×10^{-3}	1.0598×10^{-3}	7.1916×10^{-4}	VA^{-1}
0.450	8.6204×10^{-3}	4.7592×10^{-3}	3.2690×10^{-3}	2.2751×10^{-3}	1.5583×10^{-3}	1.0563×10^{-3}	7.1588×10^{-4}	VA^{-1}
0.475	8.7424×10^{-3}	4.7929×10^{-3}	3.2748×10^{-3}	2.2771×10^{-3}	1.5590×10^{-3}	1.0552×10^{-3}	7.1397×10^{-4}	VA^{-1}
0.500	8.9008×10^{-3}	4.8316×10^{-3}	3.2873×10^{-3}	2.2771×10^{-3}	1.5601×10^{-3}	1.0557×10^{-3}	7.1390×10^{-4}	VA^{-1}
0.525	9.0856×10^{-3}	4.8753×10^{-3}	3.3040×10^{-3}	2.2815×10^{-3}	1.5615×10^{-3}	1.0565×10^{-3}	7.1443×10^{-4}	VA^{-1}
0.550	9.2982×10^{-3}	4.9244×10^{-3}	3.3242×10^{-3}	2.2910×10^{-3}	1.5644×10^{-3}	1.0574×10^{-3}	7.1466×10^{-4}	VA^{-1}
0.575	9.5422×10^{-3}	4.9941×10^{-3}	3.3478×10^{-3}	2.3037×10^{-3}	1.5711×10^{-3}	1.0606×10^{-3}	7.1614×10^{-4}	VA^{-1}
0.600	9.8218×10^{-3}	5.2750×10^{-3}	3.3757×10^{-3}	2.3193×10^{-3}	1.5803×10^{-3}	1.0661×10^{-3}	7.1938×10^{-4}	VA^{-1}
0.625	1.0141×10^{-2}	5.5344×10^{-3}	3.4091×10^{-3}	2.3383×10^{-3}	1.5918×10^{-3}	1.0732×10^{-3}	7.2392×10^{-4}	VA^{-1}
0.650	1.0503×10^{-2}	5.7658×10^{-3}	3.4482×10^{-3}	2.3615×10^{-3}	1.6061×10^{-3}	1.0822×10^{-3}	7.2969×10^{-4}	VA^{-1}
0.675	1.0918×10^{-2}	6.0193×10^{-3}	3.4931×10^{-3}	2.3891×10^{-3}	1.6239×10^{-3}	1.0936×10^{-3}	7.3699×10^{-4}	VA^{-1}
0.700	1.1383×10^{-2}	6.2951×10^{-3}	3.5452×10^{-3}	2.4212×10^{-3}	1.6450×10^{-3}	1.1076×10^{-3}	7.4614×10^{-4}	VA^{-1}
0.725	1.1915×10^{-2}	6.5984×10^{-3}	3.7775×10^{-3}	2.4589×10^{-3}	1.6698×10^{-3}	1.1241×10^{-3}	7.5713×10^{-4}	VA^{-1}
0.750	1.2518×10^{-2}	6.9349×10^{-3}	4.0248×10^{-3}	2.5032×10^{-3}	1.6991×10^{-3}	1.1436×10^{-3}	7.7012×10^{-4}	VA^{-1}
0.775	1.3205×10^{-2}	7.3129×10^{-3}	4.2578×10^{-3}	2.5560×10^{-3}	1.7340×10^{-3}	1.1669×10^{-3}	7.8559×10^{-4}	VA^{-1}
0.800	1.3990×10^{-2}	7.7424×10^{-3}	4.5116×10^{-3}	2.7012×10^{-3}	1.7758×10^{-3}	1.1947×10^{-3}	8.0410×10^{-4}	VA^{-1}
0.825	1.4893×10^{-2}	8.2279×10^{-3}	4.7905×10^{-3}	2.9031×10^{-3}	1.8265×10^{-3}	1.2284×10^{-3}	8.2644×10^{-4}	VA^{-1}
0.850	1.5934×10^{-2}	8.7833×10^{-3}	5.1041×10^{-3}	3.0937×10^{-3}	1.9139×10^{-3}	1.2697×10^{-3}	8.5371×10^{-4}	VA^{-1}
0.875	1.7129×10^{-2}	9.4178×10^{-3}	5.4541×10^{-3}	3.2984×10^{-3}	2.0620×10^{-3}	1.3216×10^{-3}	8.8771×10^{-4}	VA^{-1}
0.900	1.7876×10^{-2}	1.0142×10^{-2}	5.8519×10^{-3}	3.5255×10^{-3}	2.2032×10^{-3}	1.4106×10^{-3}	9.3141×10^{-4}	VA^{-1}
0.925	1.7876×10^{-2}	1.0959×10^{-2}	6.3008×10^{-3}	3.7777×10^{-3}	2.3517×10^{-3}	1.5123×10^{-3}	9.9391×10^{-4}	VA^{-1}
0.950	1.7876×10^{-2}	1.1128×10^{-2}	6.7987×10^{-3}	4.0624×10^{-3}	2.5193×10^{-3}	1.6148×10^{-3}	1.0650×10^{-3}	VA^{-1}
0.975	1.7876×10^{-2}	1.1128×10^{-2}	6.8976×10^{-3}	4.3140×10^{-3}	2.7105×10^{-3}	1.7324×10^{-3}	1.1400×10^{-3}	VA^{-1}
1.000	1.7876×10^{-2}	1.1128×10^{-2}	6.8976×10^{-3}	4.3140×10^{-3}	2.7475×10^{-3}	1.7879×10^{-3}	1.1897×10^{-3}	VA^{-1}

Tab. A.7: Values of the entropic heating map $\frac{\partial U}{\partial T}(|Cr| = 1\,\mathrm{h}^{-1}, T, SoC)$

SoC	−10 °C	0 °C	10 °C	20 °C	30 °C	40 °C	50 °C	Unit
0.000	-1.7580×10^{-4}	-1.7580×10^{-4}	-1.7580×10^{-4}	-1.7580×10^{-4}	-1.7580×10^{-4}	-1.7580×10^{-4}	-1.7580×10^{-4}	VK^{-1}
0.001	-2.0826×10^{-4}	-2.0581×10^{-4}	-2.0237×10^{-4}	-1.9833×10^{-4}	-1.9435×10^{-4}	-1.9094×10^{-4}	-1.8822×10^{-4}	VK^{-1}
0.002	-2.3916×10^{-4}	-2.3098×10^{-4}	-2.2139×10^{-4}	-2.1224×10^{-4}	-2.0473×10^{-4}	-1.9899×10^{-4}	-1.9472×10^{-4}	VK^{-1}
0.004	-2.9441×10^{-4}	-2.7182×10^{-4}	-2.5028×10^{-4}	-2.3311×10^{-4}	-2.2051×10^{-4}	-2.1149×10^{-4}	-2.0505×10^{-4}	VK^{-1}
0.006	-3.3966×10^{-4}	-3.0455×10^{-4}	-2.7357×10^{-4}	-2.5026×10^{-4}	-2.3374×10^{-4}	-2.2219×10^{-4}	-2.1411×10^{-4}	VK^{-1}
0.008	-3.7501×10^{-4}	-3.3184×10^{-4}	-2.9380×10^{-4}	-2.6553×10^{-4}	-2.4573×10^{-4}	-2.3206×10^{-4}	-2.2264×10^{-4}	VK^{-1}
0.010	-4.0120×10^{-4}	-3.5497×10^{-4}	-3.1192×10^{-4}	-2.7959×10^{-4}	-2.5697×10^{-4}	-2.4147×10^{-4}	-2.3093×10^{-4}	VK^{-1}
0.015	-4.3270×10^{-4}	-3.9826×10^{-4}	-3.5037×10^{-4}	-3.1109×10^{-4}	-2.8303×10^{-4}	-2.6393×10^{-4}	-2.5136×10^{-4}	VK^{-1}
0.020	-4.2834×10^{-4}	-4.2450×10^{-4}	-3.8099×10^{-4}	-3.3873×10^{-4}	-3.0716×10^{-4}	-2.8563×10^{-4}	-2.7186×10^{-4}	VK^{-1}
0.030	-3.6937×10^{-4}	-4.3731×10^{-4}	-4.2232×10^{-4}	-3.8429×10^{-4}	-3.5089×10^{-4}	-3.2761×10^{-4}	-3.1316×10^{-4}	VK^{-1}
0.040	-2.8779×10^{-4}	-4.1358×10^{-4}	-4.3988×10^{-4}	-4.1710×10^{-4}	-3.8815×10^{-4}	-3.6659×10^{-4}	-3.5308×10^{-4}	VK^{-1}
0.050	-2.1230×10^{-4}	-3.6969×10^{-4}	-4.3682×10^{-4}	-4.3649×10^{-4}	-4.1712×10^{-4}	-4.0004×10^{-4}	-3.8875×10^{-4}	VK^{-1}
0.075	-1.0404×10^{-4}	-2.3563×10^{-4}	-3.6588×10^{-4}	-4.2551×10^{-4}	-4.4109×10^{-4}	-4.4232×10^{-4}	-4.4067×10^{-4}	VK^{-1}
0.100	-6.8339×10^{-5}	-1.3616×10^{-4}	-2.5693×10^{-4}	-3.4687×10^{-4}	-3.9066×10^{-4}	-4.1010×10^{-4}	-4.1925×10^{-4}	VK^{-1}
0.125	-5.1880×10^{-5}	-8.2932×10^{-5}	-1.6093×10^{-4}	-2.4185×10^{-4}	-2.9249×10^{-4}	-3.2009×10^{-4}	-3.3522×10^{-4}	VK^{-1}
0.150	-3.9094×10^{-5}	-5.7141×10^{-5}	-9.7469×10^{-5}	-1.5052×10^{-4}	-1.9032×10^{-4}	-2.1491×10^{-4}	-2.2951×10^{-4}	VK^{-1}
0.175	-2.7413×10^{-5}	-4.1809×10^{-5}	-6.1713×10^{-5}	-8.9767×10^{-5}	-1.1383×10^{-4}	-1.3017×10^{-4}	-1.4050×10^{-4}	VK^{-1}
0.200	-1.6678×10^{-5}	-3.0036×10^{-5}	-4.1755×10^{-5}	-5.5375×10^{-5}	-6.7682×10^{-5}	-7.6652×10^{-5}	-8.2630×10^{-5}	VK^{-1}
0.225	-7.0883×10^{-6}	-1.9872×10^{-5}	-2.8778×10^{-5}	-3.6233×10^{-5}	-4.2469×10^{-5}	-4.7104×10^{-5}	-5.0321×10^{-5}	VK^{-1}
0.250	1.2197×10^{-6}	-1.0989×10^{-5}	-1.8780×10^{-5}	-2.4011×10^{-5}	-2.7785×10^{-5}	-3.0490×10^{-5}	-3.2396×10^{-5}	VK^{-1}
0.275	8.2470×10^{-6}	-3.3694×10^{-6}	-1.0468×10^{-5}	-1.4814×10^{-5}	-1.7653×10^{-5}	-1.9588×10^{-5}	-2.0941×10^{-5}	VK^{-1}
0.300	1.4110×10^{-5}	3.0358×10^{-6}	-3.4902×10^{-6}	-7.3153×10^{-6}	-9.6965×10^{-6}	-1.1265×10^{-5}	-1.2343×10^{-5}	VK^{-1}
0.325	1.8997×10^{-5}	8.3636×10^{-6}	2.3247×10^{-6}	-1.0973×10^{-6}	-3.1598×10^{-6}	-4.4810×10^{-6}	-5.3706×10^{-6}	VK^{-1}
0.350	2.3117×10^{-5}	1.2807×10^{-5}	7.1592×10^{-6}	4.0614×10^{-6}	2.2518×10^{-6}	1.1264×10^{-6}	3.8776×10^{-7}	VK^{-1}
0.375	2.6675×10^{-5}	1.6575×10^{-5}	1.1220×10^{-5}	8.3707×10^{-6}	6.7580×10^{-6}	5.7866×10^{-6}	5.1683×10^{-6}	VK^{-1}
0.400	2.9841×10^{-5}	1.9857×10^{-5}	1.4709×10^{-5}	1.2039×10^{-5}	1.0571×10^{-5}	9.7145×10^{-6}	9.1867×10^{-6}	VK^{-1}
0.425	3.2748×10^{-5}	2.2812×10^{-5}	1.7800×10^{-5}	1.5253×10^{-5}	1.3885×10^{-5}	1.3109×10^{-5}	1.2645×10^{-5}	VK^{-1}
0.450	3.5490×10^{-5}	2.5558×10^{-5}	2.0631×10^{-5}	1.8162×10^{-5}	1.6860×10^{-5}	1.6138×10^{-5}	1.5717×10^{-5}	VK^{-1}
0.475	3.8133×10^{-5}	2.8177×10^{-5}	2.3300×10^{-5}	2.0880×10^{-5}	1.9618×10^{-5}	1.8929×10^{-5}	1.8535×10^{-5}	VK^{-1}
0.500	4.0717×10^{-5}	3.0723×10^{-5}	2.5874×10^{-5}	2.3481×10^{-5}	2.2244×10^{-5}	2.1574×10^{-5}	2.1197×10^{-5}	VK^{-1}
0.525	4.3270×10^{-5}	3.3229×10^{-5}	2.8395×10^{-5}	2.6017×10^{-5}	2.4793×10^{-5}	2.4135×10^{-5}	2.3767×10^{-5}	VK^{-1}
0.550	4.5956×10^{-5}	3.5724×10^{-5}	3.0888×10^{-5}	2.8518×10^{-5}	2.7301×10^{-5}	2.6648×10^{-5}	2.6285×10^{-5}	VK^{-1}
0.575	5.0530×10^{-5}	3.8481×10^{-5}	3.3418×10^{-5}	3.1014×10^{-5}	2.9791×10^{-5}	2.9139×10^{-5}	2.8778×10^{-5}	VK^{-1}
0.600	6.4037×10^{-5}	4.4259×10^{-5}	3.6911×10^{-5}	3.3869×10^{-5}	3.2441×10^{-5}	3.1711×10^{-5}	3.1314×10^{-5}	VK^{-1}
0.625	8.7097×10^{-5}	6.1450×10^{-5}	4.7180×10^{-5}	4.0539×10^{-5}	3.7390×10^{-5}	3.5796×10^{-5}	3.4932×10^{-5}	VK^{-1}
0.650	9.2010×10^{-5}	8.3648×10^{-5}	7.0267×10^{-5}	5.9728×10^{-5}	5.2869×10^{-5}	4.8573×10^{-5}	4.5845×10^{-5}	VK^{-1}
0.675	7.4249×10^{-5}	8.0050×10^{-5}	8.2548×10^{-5}	8.0355×10^{-5}	7.6469×10^{-5}	7.2633×10^{-5}	6.9404×10^{-5}	VK^{-1}
0.700	6.3621×10^{-5}	6.1344×10^{-5}	6.6664×10^{-5}	7.2510×10^{-5}	7.6573×10^{-5}	7.8918×10^{-5}	8.0116×10^{-5}	VK^{-1}
0.725	6.3450×10^{-5}	5.4455×10^{-5}	5.2632×10^{-5}	5.4398×10^{-5}	5.7435×10^{-5}	6.0548×10^{-5}	6.3277×10^{-5}	VK^{-1}
0.750	6.5318×10^{-5}	5.5533×10^{-5}	5.1012×10^{-5}	4.9280×10^{-5}	4.8967×10^{-5}	4.9345×10^{-5}	5.0013×10^{-5}	VK^{-1}
0.775	6.6411×10^{-5}	5.7920×10^{-5}	5.3111×10^{-5}	5.0784×10^{-5}	4.9639×10^{-5}	4.9086×10^{-5}	4.8839×10^{-5}	VK^{-1}
0.800	6.7152×10^{-5}	6.0383×10^{-5}	5.5564×10^{-5}	5.3203×10^{-5}	5.1995×10^{-5}	5.1352×10^{-5}	5.0998×10^{-5}	VK^{-1}
0.825	6.7666×10^{-5}	6.2766×10^{-5}	5.8029×10^{-5}	5.5668×10^{-5}	5.4458×10^{-5}	5.3812×10^{-5}	5.3454×10^{-5}	VK^{-1}
0.850	6.8008×10^{-5}	6.4263×10^{-5}	6.0494×10^{-5}	5.8133×10^{-5}	5.6923×10^{-5}	5.6277×10^{-5}	5.5919×10^{-5}	VK^{-1}
0.875	6.8229×10^{-5}	6.5336×10^{-5}	6.2959×10^{-5}	6.0599×10^{-5}	5.9389×10^{-5}	5.8743×10^{-5}	5.8385×10^{-5}	VK^{-1}
0.900	6.8385×10^{-5}	6.6251×10^{-5}	6.4712×10^{-5}	6.3064×10^{-5}	6.1854×10^{-5}	6.1208×10^{-5}	6.0850×10^{-5}	VK^{-1}
0.925	6.8550×10^{-5}	6.7102×10^{-5}	6.6074×10^{-5}	6.5285×10^{-5}	6.4320×10^{-5}	6.3674×10^{-5}	6.3316×10^{-5}	VK^{-1}
0.950	6.8822×10^{-5}	6.7978×10^{-5}	6.7370×10^{-5}	6.6920×10^{-5}	6.6569×10^{-5}	6.6139×10^{-5}	6.5781×10^{-5}	VK^{-1}
0.975	6.8949×10^{-5}	6.8961×10^{-5}	6.8712×10^{-5}	6.8510×10^{-5}	6.8352×10^{-5}	6.8234×10^{-5}	6.8139×10^{-5}	VK^{-1}
1.000	6.8949×10^{-5}	6.8961×10^{-5}	6.9235×10^{-5}	6.9478×10^{-5}	6.9659×10^{-5}	6.9787×10^{-5}	6.9877×10^{-5}	VK^{-1}

Tab. A.8: Values of the entropic heating map $\frac{\partial U}{\partial T}(|Cr| = 2\,\mathrm{h}^{-1}, T, SoC)$

SoC	−10 °C	0 °C	10 °C	20 °C	30 °C	40 °C	50 °C	Unit
0.000	-1.7580×10^{-4}	-1.7580×10^{-4}	-1.7580×10^{-4}	-1.7580×10^{-4}	-1.7580×10^{-4}	-1.7580×10^{-4}	-1.7580×10^{-4}	VK^{-1}
0.001	-2.0979×10^{-4}	-2.0836×10^{-4}	-2.0612×10^{-4}	-2.0302×10^{-4}	-1.9935×10^{-4}	-1.9562×10^{-4}	-1.9230×10^{-4}	VK^{-1}
0.002	-2.4478×10^{-4}	-2.3938×10^{-4}	-2.3182×10^{-4}	-2.2298×10^{-4}	-2.1436×10^{-4}	-2.0704×10^{-4}	-2.0127×10^{-4}	VK^{-1}
0.004	-3.1210×10^{-4}	-2.9461×10^{-4}	-2.7361×10^{-4}	-2.5338×10^{-4}	-2.3680×10^{-4}	-2.2425×10^{-4}	-2.1501×10^{-4}	VK^{-1}
0.006	-3.6819×10^{-4}	-3.3970×10^{-4}	-3.0702×10^{-4}	-2.7778×10^{-4}	-2.5511×10^{-4}	-2.3855×10^{-4}	-2.2663×10^{-4}	VK^{-1}
0.008	-4.0728×10^{-4}	-3.7494×10^{-4}	-3.3478×10^{-4}	-2.9885×10^{-4}	-2.7132×10^{-4}	-2.5142×10^{-4}	-2.3726×10^{-4}	VK^{-1}
0.010	-4.2765×10^{-4}	-4.0116×10^{-4}	-3.5819×10^{-4}	-3.1761×10^{-4}	-2.8615×10^{-4}	-2.6341×10^{-4}	-2.4731×10^{-4}	VK^{-1}
0.015	-4.1452×10^{-4}	-4.3330×10^{-4}	-4.0156×10^{-4}	-3.5699×10^{-4}	-3.1905×10^{-4}	-2.9090×10^{-4}	-2.7099×10^{-4}	VK^{-1}
0.020	-3.6012×10^{-4}	-4.3002×10^{-4}	-4.2713×10^{-4}	-3.8773×10^{-4}	-3.4745×10^{-4}	-3.1596×10^{-4}	-2.9347×10^{-4}	VK^{-1}
0.030	-2.3126×10^{-4}	-3.7356×10^{-4}	-4.3725×10^{-4}	-4.2733×10^{-4}	-3.9292×10^{-4}	-3.6027×10^{-4}	-3.3591×10^{-4}	VK^{-1}
0.040	-1.4422×10^{-4}	-2.9373×10^{-4}	-4.1066×10^{-4}	-4.4129×10^{-4}	-4.2376×10^{-4}	-3.9658×10^{-4}	-3.7425×10^{-4}	VK^{-1}
0.050	-1.0042×10^{-4}	-2.1772×10^{-4}	-3.6454×10^{-4}	-4.3373×10^{-4}	-4.3975×10^{-4}	-4.2335×10^{-4}	-4.0621×10^{-4}	VK^{-1}
0.075	-6.1568×10^{-5}	-1.0389×10^{-4}	-2.2734×10^{-4}	-3.5307×10^{-4}	-4.1789×10^{-4}	-4.3882×10^{-4}	-4.4246×10^{-4}	VK^{-1}
0.100	-4.1743×10^{-5}	-6.3375×10^{-5}	-1.2772×10^{-4}	-2.4039×10^{-4}	-3.3155×10^{-4}	-3.8055×10^{-4}	-4.0387×10^{-4}	VK^{-1}
0.125	-2.5999×10^{-5}	-4.4538×10^{-5}	-7.4760×10^{-5}	-1.4615×10^{-4}	-2.2515×10^{-4}	-2.7907×10^{-4}	-3.1034×10^{-4}	VK^{-1}
0.150	-1.2749×10^{-5}	-3.0881×10^{-5}	-4.9098×10^{-5}	-8.6013×10^{-5}	-1.3678×10^{-4}	-1.7798×10^{-4}	-2.0514×10^{-4}	VK^{-1}
0.175	-1.5307×10^{-6}	-1.9378×10^{-5}	-3.3944×10^{-5}	-5.2950×10^{-5}	-7.9759×10^{-5}	-1.0443×10^{-4}	-1.2232×10^{-4}	VK^{-1}
0.200	7.8415×10^{-6}	-9.5082×10^{-6}	-2.2728×10^{-5}	-3.4599×10^{-5}	-4.8119×10^{-5}	-6.0924×10^{-5}	-7.0859×10^{-5}	VK^{-1}
0.225	1.5567×10^{-5}	-1.1596×10^{-6}	-1.3493×10^{-5}	-2.2733×10^{-5}	-3.0617×10^{-5}	-3.7428×10^{-5}	-4.2769×10^{-5}	VK^{-1}
0.250	2.1915×10^{-5}	5.7881×10^{-6}	-5.7370×10^{-6}	-1.3741×10^{-5}	-1.9473×10^{-5}	-2.3808×10^{-5}	-2.7079×10^{-5}	VK^{-1}
0.275	2.7181×10^{-5}	1.1524×10^{-5}	7.3185×10^{-7}	-6.4187×10^{-6}	-1.1158×10^{-5}	-1.4462×10^{-5}	-1.6848×10^{-5}	VK^{-1}
0.300	3.1646×10^{-5}	1.6279×10^{-5}	6.0936×10^{-6}	-3.6301×10^{-7}	-4.4539×10^{-6}	-7.1844×10^{-6}	-9.0970×10^{-6}	VK^{-1}
0.325	3.5546×10^{-5}	2.0289×10^{-5}	1.0557×10^{-5}	4.6583×10^{-6}	1.0691×10^{-6}	-1.2447×10^{-6}	-2.8212×10^{-6}	VK^{-1}
0.350	3.9063×10^{-5}	2.3763×10^{-5}	1.4335×10^{-5}	8.8603×10^{-6}	5.6591×10^{-6}	3.6692×10^{-6}	2.3561×10^{-6}	VK^{-1}
0.375	4.2326×10^{-5}	2.6874×10^{-5}	1.7625×10^{-5}	1.2450×10^{-5}	9.5339×10^{-6}	7.7874×10^{-6}	6.6758×10^{-6}	VK^{-1}
0.400	4.5424×10^{-5}	2.9747×10^{-5}	2.0584×10^{-5}	1.5610×10^{-5}	1.2891×10^{-5}	1.1317×10^{-5}	1.0351×10^{-5}	VK^{-1}
0.425	4.8413×10^{-5}	3.2473×10^{-5}	2.3333×10^{-5}	1.8485×10^{-5}	1.5894×10^{-5}	1.4436×10^{-5}	1.3570×10^{-5}	VK^{-1}
0.450	5.1333×10^{-5}	3.5107×10^{-5}	2.5954×10^{-5}	2.1180×10^{-5}	1.8670×10^{-5}	1.7285×10^{-5}	1.6483×10^{-5}	VK^{-1}
0.475	5.4335×10^{-5}	3.7688×10^{-5}	2.8502×10^{-5}	2.3770×10^{-5}	2.1306×10^{-5}	1.9965×10^{-5}	1.9202×10^{-5}	VK^{-1}
0.500	5.8695×10^{-5}	4.0252×10^{-5}	3.1009×10^{-5}	2.6299×10^{-5}	2.3861×10^{-5}	2.2545×10^{-5}	2.1805×10^{-5}	VK^{-1}
0.525	6.9437×10^{-5}	4.3148×10^{-5}	3.3506×10^{-5}	2.8796×10^{-5}	2.6372×10^{-5}	2.5069×10^{-5}	2.4342×10^{-5}	VK^{-1}
0.550	8.6583×10^{-5}	4.9307×10^{-5}	3.6276×10^{-5}	3.1302×10^{-5}	2.8862×10^{-5}	2.7564×10^{-5}	2.6843×10^{-5}	VK^{-1}
0.575	9.8413×10^{-5}	6.6475×10^{-5}	4.2123×10^{-5}	3.4388×10^{-5}	3.1469×10^{-5}	3.0079×10^{-5}	2.9337×10^{-5}	VK^{-1}
0.600	9.8568×10^{-5}	8.7712×10^{-5}	5.9357×10^{-5}	4.2498×10^{-5}	3.5946×10^{-5}	3.3344×10^{-5}	3.2173×10^{-5}	VK^{-1}
0.625	8.8221×10^{-5}	8.4307×10^{-5}	8.1378×10^{-5}	6.3624×10^{-5}	4.9994×10^{-5}	4.2542×10^{-5}	3.8708×10^{-5}	VK^{-1}
0.650	7.6627×10^{-5}	6.6199×10^{-5}	7.7703×10^{-5}	8.1030×10^{-5}	7.3936×10^{-5}	6.4935×10^{-5}	5.7694×10^{-5}	VK^{-1}
0.675	7.0714×10^{-5}	5.9279×10^{-5}	5.9090×10^{-5}	6.9206×10^{-5}	7.7294×10^{-5}	7.9775×10^{-5}	7.8612×10^{-5}	VK^{-1}
0.700	6.8891×10^{-5}	6.0141×10^{-5}	5.2234×10^{-5}	5.2650×10^{-5}	5.8440×10^{-5}	6.5424×10^{-5}	7.1188×10^{-5}	VK^{-1}
0.725	6.8766×10^{-5}	6.1506×10^{-5}	5.3312×10^{-5}	4.9217×10^{-5}	4.8545×10^{-5}	5.0153×10^{-5}	5.2937×10^{-5}	VK^{-1}
0.750	6.8971×10^{-5}	6.2577×10^{-5}	5.5699×10^{-5}	5.1036×10^{-5}	4.8757×10^{-5}	4.7798×10^{-5}	4.7642×10^{-5}	VK^{-1}
0.775	6.9124×10^{-5}	6.3461×10^{-5}	5.8162×10^{-5}	5.3474×10^{-5}	5.1069×10^{-5}	4.9795×10^{-5}	4.9112×10^{-5}	VK^{-1}
0.800	6.9173×10^{-5}	6.4216×10^{-5}	6.0135×10^{-5}	5.5939×10^{-5}	5.3531×10^{-5}	5.2243×10^{-5}	5.1529×10^{-5}	VK^{-1}
0.825	6.9127×10^{-5}	6.4866×10^{-5}	6.1589×10^{-5}	5.8404×10^{-5}	5.5996×10^{-5}	5.4708×10^{-5}	5.3993×10^{-5}	VK^{-1}
0.850	6.9013×10^{-5}	6.5456×10^{-5}	6.2803×10^{-5}	6.0756×10^{-5}	5.8461×10^{-5}	5.7173×10^{-5}	5.6459×10^{-5}	VK^{-1}
0.875	6.8867×10^{-5}	6.6015×10^{-5}	6.3929×10^{-5}	6.2467×10^{-5}	6.0926×10^{-5}	5.9639×10^{-5}	5.8924×10^{-5}	VK^{-1}
0.900	6.8740×10^{-5}	6.6587×10^{-5}	6.5036×10^{-5}	6.3951×10^{-5}	6.3108×10^{-5}	6.2104×10^{-5}	6.1390×10^{-5}	VK^{-1}
0.925	6.8703×10^{-5}	6.7226×10^{-5}	6.6172×10^{-5}	6.5418×10^{-5}	6.4875×10^{-5}	6.4436×10^{-5}	6.3855×10^{-5}	VK^{-1}
0.950	6.8703×10^{-5}	6.7996×10^{-5}	6.7382×10^{-5}	6.6927×10^{-5}	6.6584×10^{-5}	6.6332×10^{-5}	6.6131×10^{-5}	VK^{-1}
0.975	6.8703×10^{-5}	6.8046×10^{-5}	6.8385×10^{-5}	6.8507×10^{-5}	6.8349×10^{-5}	6.8224×10^{-5}	6.8127×10^{-5}	VK^{-1}
1.000	6.8703×10^{-5}	6.8046×10^{-5}	6.8385×10^{-5}	6.8816×10^{-5}	6.9158×10^{-5}	6.9407×10^{-5}	6.9586×10^{-5}	VK^{-1}

Tab. A.9: Values of the entropic heating map $\frac{\partial U}{\partial T}(|Cr| = 3\,\mathrm{h}^{-1}, T, SoC)$

SoC	−10 °C	0 °C	10 °C	20 °C	30 °C	40 °C	50 °C	Unit
0.000	-1.7580×10^{-4}	-1.7580×10^{-4}	-1.7580×10^{-4}	-1.7580×10^{-4}	-1.7580×10^{-4}	-1.7580×10^{-4}	-1.7580×10^{-4}	VK^{-1}
0.001	-2.1035×10^{-4}	-2.0934×10^{-4}	-2.0770×10^{-4}	-2.0526×10^{-4}	-2.0210×10^{-4}	-1.9854×10^{-4}	-1.9506×10^{-4}	VK^{-1}
0.002	-2.4695×10^{-4}	-2.4297×10^{-4}	-2.3696×10^{-4}	-2.2917×10^{-4}	-2.2065×10^{-4}	-2.1270×10^{-4}	-2.0607×10^{-4}	VK^{-1}
0.004	-3.1948×10^{-4}	-3.0579×10^{-4}	-2.8728×10^{-4}	-2.6700×10^{-4}	-2.4861×10^{-4}	-2.3386×10^{-4}	-2.2268×10^{-4}	VK^{-1}
0.006	-3.7972×10^{-4}	-3.5774×10^{-4}	-3.2789×10^{-4}	-2.9715×10^{-4}	-2.7110×10^{-4}	-2.5116×10^{-4}	-2.3648×10^{-4}	VK^{-1}
0.008	-4.1709×10^{-4}	-3.9606×10^{-4}	-3.6045×10^{-4}	-3.2254×10^{-4}	-2.9066×10^{-4}	-2.6652×10^{-4}	-2.4892×10^{-4}	VK^{-1}
0.010	-4.2831×10^{-4}	-4.2041×10^{-4}	-3.8617×10^{-4}	-3.4443×10^{-4}	-3.0821×10^{-4}	-2.8061×10^{-4}	-2.6052×10^{-4}	VK^{-1}
0.015	-3.8426×10^{-4}	-4.3018×10^{-4}	-4.2570×10^{-4}	-3.8724×10^{-4}	-3.4575×10^{-4}	-3.1213×10^{-4}	-2.8723×10^{-4}	VK^{-1}
0.020	-3.0306×10^{-4}	-3.9835×10^{-4}	-4.3712×10^{-4}	-4.1611×10^{-4}	-3.7613×10^{-4}	-3.3970×10^{-4}	-3.1173×10^{-4}	VK^{-1}
0.030	-1.6270×10^{-4}	-2.9768×10^{-4}	-4.0849×10^{-4}	-4.4002×10^{-4}	-4.1868×10^{-4}	-3.8506×10^{-4}	-3.5558×10^{-4}	VK^{-1}
0.040	-1.0209×10^{-4}	-2.0153×10^{-4}	-3.4882×10^{-4}	-4.2944×10^{-4}	-4.3917×10^{-4}	-4.1763×10^{-4}	-3.9225×10^{-4}	VK^{-1}
0.050	-7.7460×10^{-5}	-1.3687×10^{-4}	-2.7894×10^{-4}	-3.9660×10^{-4}	-4.3986×10^{-4}	-4.3676×10^{-4}	-4.2008×10^{-4}	VK^{-1}
0.075	-4.7111×10^{-5}	-6.8944×10^{-5}	-1.4108×10^{-4}	-2.7329×10^{-4}	-3.7684×10^{-4}	-4.2496×10^{-4}	-4.3979×10^{-4}	VK^{-1}
0.100	-2.6093×10^{-5}	-4.4561×10^{-5}	-7.5061×10^{-5}	-1.6061×10^{-4}	-2.6894×10^{-4}	-3.4501×10^{-4}	-3.8515×10^{-4}	VK^{-1}
0.125	-9.5438×10^{-6}	-2.8102×10^{-5}	-4.7401×10^{-5}	-9.0481×10^{-5}	-1.6727×10^{-4}	-2.3818×10^{-4}	-2.8451×10^{-4}	VK^{-1}
0.150	3.6718×10^{-6}	-1.5072×10^{-5}	-3.1537×10^{-5}	-5.3850×10^{-5}	-9.6785×10^{-5}	-1.4495×10^{-4}	-1.8171×10^{-4}	VK^{-1}
0.175	1.4097×10^{-5}	-4.4771×10^{-6}	-1.9825×10^{-5}	-3.4472×10^{-5}	-5.6205×10^{-5}	-8.2883×10^{-5}	-1.0566×10^{-4}	VK^{-1}
0.200	2.2299×10^{-5}	4.1139×10^{-6}	-1.0368×10^{-5}	-2.2242×10^{-5}	-3.4483×10^{-5}	-4.8100×10^{-5}	-6.0324×10^{-5}	VK^{-1}
0.225	2.8847×10^{-5}	1.1051×10^{-5}	-2.6161×10^{-6}	-1.3122×10^{-5}	-2.1684×10^{-5}	-2.9394×10^{-5}	-3.6032×10^{-5}	VK^{-1}
0.250	3.4233×10^{-5}	1.6679×10^{-5}	3.7226×10^{-6}	-5.8026×10^{-6}	-1.2772×10^{-5}	-1.8116×10^{-5}	-2.2328×10^{-5}	VK^{-1}
0.275	3.8838×10^{-5}	2.1327×10^{-5}	8.9123×10^{-6}	1.9109×10^{-7}	-5.8180×10^{-6}	-1.0072×10^{-5}	-1.3216×10^{-5}	VK^{-1}
0.300	4.2502×10^{-5}	2.5280×10^{-5}	1.3215×10^{-5}	5.1347×10^{-6}	-1.5495×10^{-7}	-3.7231×10^{-6}	-6.2584×10^{-6}	VK^{-1}
0.325	4.5670×10^{-5}	2.8762×10^{-5}	1.6871×10^{-5}	9.2656×10^{-6}	4.5313×10^{-6}	1.4749×10^{-6}	-6.2097×10^{-7}	VK^{-1}
0.350	4.8431×10^{-5}	3.1937×10^{-5}	2.0081×10^{-5}	1.2799×10^{-5}	8.4750×10^{-6}	5.8039×10^{-6}	4.0429×10^{-6}	VK^{-1}
0.375	5.1030×10^{-5}	3.4917×10^{-5}	2.2998×10^{-5}	1.5919×10^{-5}	1.1880×10^{-5}	9.4850×10^{-6}	7.9707×10^{-6}	VK^{-1}
0.400	5.3389×10^{-5}	3.7773×10^{-5}	2.5731×10^{-5}	1.8767×10^{-5}	1.4914×10^{-5}	1.2707×10^{-5}	1.1365×10^{-5}	VK^{-1}
0.425	5.5580×10^{-5}	4.0549×10^{-5}	2.8354×10^{-5}	2.1446×10^{-5}	1.7709×10^{-5}	1.5622×10^{-5}	1.4393×10^{-5}	VK^{-1}
0.450	5.7894×10^{-5}	4.3294×10^{-5}	3.0913×10^{-5}	2.4026×10^{-5}	2.0357×10^{-5}	1.8343×10^{-5}	1.7184×10^{-5}	VK^{-1}
0.475	6.0671×10^{-5}	4.6409×10^{-5}	3.3438×10^{-5}	2.6550×10^{-5}	2.2918×10^{-5}	2.0947×10^{-5}	1.9829×10^{-5}	VK^{-1}
0.500	6.6369×10^{-5}	5.2781×10^{-5}	3.6014×10^{-5}	2.9045×10^{-5}	2.5432×10^{-5}	2.3484×10^{-5}	2.2390×10^{-5}	VK^{-1}
0.525	7.6893×10^{-5}	6.9360×10^{-5}	3.9712×10^{-5}	3.1573×10^{-5}	2.7924×10^{-5}	2.5985×10^{-5}	2.4903×10^{-5}	VK^{-1}
0.550	9.0428×10^{-5}	9.0006×10^{-5}	5.0305×10^{-5}	3.4996×10^{-5}	3.0497×10^{-5}	2.8480×10^{-5}	2.7394×10^{-5}	VK^{-1}
0.575	1.0044×10^{-4}	8.8276×10^{-5}	7.2790×10^{-5}	4.4771×10^{-5}	3.4578×10^{-5}	3.1314×10^{-5}	2.9967×10^{-5}	VK^{-1}
0.600	9.9849×10^{-5}	7.5660×10^{-5}	8.4451×10^{-5}	6.7265×10^{-5}	4.7221×10^{-5}	3.7818×10^{-5}	3.4067×10^{-5}	VK^{-1}
0.625	8.9493×10^{-5}	6.6556×10^{-5}	6.9200×10^{-5}	8.0765×10^{-5}	7.1099×10^{-5}	5.6692×10^{-5}	4.6876×10^{-5}	VK^{-1}
0.650	7.7828×10^{-5}	6.2231×10^{-5}	5.5386×10^{-5}	6.5979×10^{-5}	7.7746×10^{-5}	7.7654×10^{-5}	7.0911×10^{-5}	VK^{-1}
0.675	7.1555×10^{-5}	6.2057×10^{-5}	5.3675×10^{-5}	5.1317×10^{-5}	5.9630×10^{-5}	7.0470×10^{-5}	7.7131×10^{-5}	VK^{-1}
0.700	6.9347×10^{-5}	6.2527×10^{-5}	5.5752×10^{-5}	4.9238×10^{-5}	4.8241×10^{-5}	5.2201×10^{-5}	5.8771×10^{-5}	VK^{-1}
0.725	6.9109×10^{-5}	6.3193×10^{-5}	5.7401×10^{-5}	5.1267×10^{-5}	4.7881×10^{-5}	4.6809×10^{-5}	4.7593×10^{-5}	VK^{-1}
0.750	6.9218×10^{-5}	6.3822×10^{-5}	5.8839×10^{-5}	5.3716×10^{-5}	5.0133×10^{-5}	4.8255×10^{-5}	4.7340×10^{-5}	VK^{-1}
0.775	6.9299×10^{-5}	6.4377×10^{-5}	6.0014×10^{-5}	5.6180×10^{-5}	5.2592×10^{-5}	5.0670×10^{-5}	4.9606×10^{-5}	VK^{-1}
0.800	6.9287×10^{-5}	6.4867×10^{-5}	6.1074×10^{-5}	5.8161×10^{-5}	5.5057×10^{-5}	5.3134×10^{-5}	5.2066×10^{-5}	VK^{-1}
0.825	6.9191×10^{-5}	6.5314×10^{-5}	6.2083×10^{-5}	5.9800×10^{-5}	5.7522×10^{-5}	5.5599×10^{-5}	5.4531×10^{-5}	VK^{-1}
0.850	6.9036×10^{-5}	6.5739×10^{-5}	6.3069×10^{-5}	6.1205×10^{-5}	5.9773×10^{-5}	5.8064×10^{-5}	5.6996×10^{-5}	VK^{-1}
0.875	6.8859×10^{-5}	6.6174×10^{-5}	6.4059×10^{-5}	6.2584×10^{-5}	6.1541×10^{-5}	6.0530×10^{-5}	5.9462×10^{-5}	VK^{-1}
0.900	6.8769×10^{-5}	6.6658×10^{-5}	6.5086×10^{-5}	6.3979×10^{-5}	6.3198×10^{-5}	6.2598×10^{-5}	6.1927×10^{-5}	VK^{-1}
0.925	6.8769×10^{-5}	6.7245×10^{-5}	6.6181×10^{-5}	6.5416×10^{-5}	6.4859×10^{-5}	6.4460×10^{-5}	6.4147×10^{-5}	VK^{-1}
0.950	6.8769×10^{-5}	6.7374×10^{-5}	6.7375×10^{-5}	6.6922×10^{-5}	6.6577×10^{-5}	6.6314×10^{-5}	6.6117×10^{-5}	VK^{-1}
0.975	6.8769×10^{-5}	6.7374×10^{-5}	6.7614×10^{-5}	6.8180×10^{-5}	6.8347×10^{-5}	6.8223×10^{-5}	6.8124×10^{-5}	VK^{-1}
1.000	6.8769×10^{-5}	6.7374×10^{-5}	6.7614×10^{-5}	6.8180×10^{-5}	6.8668×10^{-5}	6.9032×10^{-5}	6.9296×10^{-5}	VK^{-1}

A.2 Material parameters

If not stated differently, in all of the following tables that contain temperature dependent data, linear interpolation is used between the given values.

Copper

Tab. A.10: Copper: Temperature dependent thermal conductivity λ and specific heat capacity c_p (data from [158])

Temperature in K	λ in $Wm^{-1}K^{-1}$	c_p in $Jkg^{-1}K^{-1}$
100.0	482.0	252.0
200.0	413.0	356.0
300.0	401.0	385.0
400.0	393.0	397.0
600.0	379.0	417.0
800.0	366.0	433.0
1000.0	352.0	451.0
1200.0	339.0	480.0

Aluminum

Tab. A.11: Aluminium: Temperature dependent thermal conductivity λ and specific heat capacity c_p (data from [158])

Temperature in K	λ in $Wm^{-1}K^{-1}$	c_p in $Jkg^{-1}K^{-1}$
100.0	302.0	482.0
200.0	237.0	798.0
300.0	237.0	903.0
400.0	240.0	949.0
600.0	231.0	1033.0
800.0	218.0	1146.0

Polyamide 6.6

Tab. A.12: Polyamide 6.6: Temperature dependent specific heat capacity c_p (data from [158])

Temperature in K	c_p in $Jkg^{-1}K^{-1}$
123.15	730.0
173.15	930.0
223.15	1150.0
273.15	1380.0
293.15	1480.0
323.15	1680.0
373.15	2150.0
423.15	2600.0

Air

Tab. A.13: Air: Temperature dependent thermal conductivity λ, specific heat capacity c_p and density ρ (data from [158])

Temperature in K	λ in $Wm^{-1}K^{-1}$	c_p in $Jkg^{-1}K^{-1}$	ρ in kgm^{-3}
100.0	0.00934	1032.0	3.5562
150.0	0.0138	1012.0	2.3364
200.0	0.0181	1007.0	1.7458
250.0	0.0223	1006.0	1.3947
300.0	0.0263	1007.0	1.1614
350.0	0.03	1009.0	0.995
400.0	0.0338	1014.0	0.8711
450.0	0.0373	1021.0	0.774
500.0	0.0407	1030.0	0.6964

Cooling fluid water-glycol

Tab. A.14: Water-glycol (50/50): Temperature dependent dymanic viscosity μ and thermal conductivity λ (data from [158])

Temperature in K	μ in $\mathrm{kg\,m^{-1}\,s^{-1}}$	λ in $\mathrm{W\,m^{-1}\,K^{-1}}$
253.15	0.02207	0.344
258.15	0.01653	0.349
263.15	0.01274	0.354
268.15	0.01005	0.359
273.15	0.00809	0.364
278.15	0.00663	0.368
283.15	0.0055	0.373
288.15	0.00463	0.377
293.15	0.00394	0.38
298.15	0.00339	0.384
303.15	0.00294	0.387
308.15	0.00256	0.391
313.15	0.00226	0.394
318.15	0.002	0.397
323.15	0.00178	0.399
328.15	0.00159	0.402
333.15	0.00143	0.404
338.15	0.00129	0.406
343.15	0.00117	0.408
348.15	0.00107	0.41
353.15	9.8E-4	0.411
358.15	8.9E-4	0.413

Polynomial approximation of the specific heat capacity $c_{\mathrm{p,fluid}}$ from [158]:

$$\begin{aligned} c_{\mathrm{p,fluid}} &= a_1 + 2a_2\,(T - T_{\mathrm{ref}}) \\ &\text{with:} \\ a_1 &= 3300\,\mathrm{J\,kg^{-1}\,K^{-1}} \\ a_2 &= 1.9308\,\mathrm{J\,kg^{-1}\,K^{-2}} \end{aligned} \tag{A.1}$$

Polynomial approximation of the density ρ_{fluid} from [158]:

$$\begin{aligned} \rho_{\mathrm{fluid}} &= \rho_{\mathrm{ref}} + a_1\,(T - T_{\mathrm{ref}}) + a_2\,(T - T_{\mathrm{ref}})^2 + a_3\,(T - T_{\mathrm{ref}})\left(p - p_{\mathrm{ref}}\right) + a_4\left(p - p_{\mathrm{ref}}\right) \\ &\text{with:} \\ \rho_{\mathrm{ref}} &= 1071.11\,\mathrm{kg\,m^{-3}} \\ T_{\mathrm{ref}} &= 298\,\mathrm{K} \\ p_{\mathrm{ref}} &= 1\,\mathrm{bar} \\ a_1 &= -0.459\,749\,\mathrm{kg\,m^{-3}\,K^{-1}} \\ a_2 &= -0.002\,432\,\mathrm{kg\,m^{-3}\,K^{-2}} \\ a_3 &= 1.6481 \times 10^{-4}\,\mathrm{kg\,m^{-3}\,K^{-1}\,bar^{-1}} \\ a_4 &= 0.0385\,\mathrm{kg\,m^{-3}\,bar^{-1}} \end{aligned} \tag{A.2}$$

A.3 Hyperparameters during neural network optimization

For an easier understanding, the varied parameters are always marked in blue.

Step 1

Tab. A.15: Hyperparameters in step 1 of the optimization procedure

Hyperparameter	Value
Hidden layers	{1, 2, 3, 4, 5}
Neurons in hidden layers	see table A.16
Activation function in hidden layers	sigmoid
Activation function in output layer	linear
Batch size	2
Learning rate	0.001
Training epochs	1000
Loss function	mean squared error
Optimization algorithm	Adam

Tab. A.16: Step 1 of the hyperparameter optimization: Number of neurons in the hidden layers depending on the number of hidden layers

Number of hidden layers	Hidden layer	Number of neurons
1	1	{5, 10, 15, 20, 25, 30, 35, 40, 45, 50, 55, 60}
2	1	{20, 25, 30, 35, 40}
	2	{15, 20, 25, 30, 35}
3	1	{20, 25, 30, 35, 40}
	2	{15, 20, 25, 30, 35}
	3	{10, 15, 20, 25, 30}
4	1	{20, 30, 40}
	2	{15, 25, 35}
	3	{10, 20, 30}
	4	{5, 15, 25}
5	1	{30, 35, 40}
	2	{25, 30, 35}
	3	{20, 25, 30}
	4	{15, 20, 25}
	5	{10, 15, 20}

Step 2

Tab. A.17: Hyperparameters in step 2 of the optimization procedure

Hyperparameter	Value
Hidden layers	2
Neurons in hidden layer 1	40
Neurons in hidden layer 2	35
Activation function in hidden layers	{sigmoid, ReLU}
Activation function in output layer	linear
Batch size	{2, 4, 8, 16}
Learning rate	0.001
Training epochs	1000
Loss function	mean squared error
Optimization algorithm	Adam

Step 3

Tab. A.18: Hyperparameters in step 3 of the optimization procedure

Hyperparameter	Value
Hidden layers	2
Neurons in hidden layer 1	40
Neurons in hidden layer 2	35
Act. funct. in hidden layers	sigmoid
Act. funct. in output layer	linear
Batch size	2
Learning rate	{0.0001, 0.0005, 0.001, 0.005, 0.01, 0.01, 0.05, 0.1, 0.5, 1.0}
Training epochs	1000
Loss function	mean squared error
Optimization algorithm	Adam

Nomenclature

Abbreviations

ANN	Artificial Neural Network
BaTec	Battery Technology Center
BEV	Battery Electric Vehicle
BMS	Battery Management System
CCCV	Constant-Current Constant-Voltage
CMM	Cell Meta-Model
DC	Direct Current
DFN	Doyle–Fuller–Newman
ECM	Equivalent-Circuit Model
EoL	End of Life
ETM	Electrochemical-Thermal Model
FVM	Finite Volume Method
IAM-ESS	Institute for Applied Materials - Energy Storage Systems
ICT	Institute for Chemical Technology
KIT	Karlsruhe Institute of Technology
LCO	Lithium-Cobalt-Oxide
LMO	Lithium-Manganese-Oxide
MAE	Mean Absolute Error
MSE	Mean Squared Error
MSMD	Multi-Scale Multi-Dimensional

NCA	Lithium-Nickel-Cobalt-Aluminium
NMC	Nickel-Manganese-Cobalt
NN	Neural Network
OCP	Open Circuit Potential
OCV	Open Circuit Voltage
P2D	Pseudo-Two-Dimensional
PA	Polyamide
PyBaMM	Python Battery Mathematical Modelling
RC	Resistor-Capacitor
ReLU	Rectified Linear Unit
RMSE	Root Mean Squared Error
SoC	State of Charge
SPM	Single Particle Model
TC	Thermocouple
TMS	Thermal Management System

Symbols

α	heat transfer coefficient	$(\mathrm{W\,m^{-2}\,K^{-1}})$
c_p	specific heat capacity	$(\mathrm{J\,kg^{-1}\,K^{-1}})$
C	capacitance	(F)
C	thermal mass	$(\mathrm{J\,K^{-1}})$
Cr	C-rate	$(\mathrm{h^{-1}})$
d	diameter	(m)
ΔT	temperature difference	(K)
ΔT_max	maximum temperature difference	(K)
h	height	(m)
i	volumetric current rate	$(\mathrm{A\,m^{-3}})$
I	current	(A)
λ	thermal conductivity	$(\mathrm{W\,m^{-1}\,K^{-1}})$
MAE	mean absolute error	(-)
MSE	mean squared error	(-)
μ	dynamic viscosity	$(\mathrm{kg\,m^{-1}\,s^{-1}})$
Nu	Nusselt number	(-)

p	pressure	(Pa)
Φ	electric potential	(V)
$\dot{q}$	heat flux	($\mathrm{W\,m^{-2}}$)
$\dot{q}$	volumetric heat generation rate	($\mathrm{W\,m^{-3}}$)
Q	battery cell capacity	(Ah)
$\dot{Q}$	rate of heat flow	(W)
r	width factor	(-)
r_{xy}	Pearson correlation coefficient	(-)
R	electrical resistance	(Ω)
R	thermal resistance	($\mathrm{K\,W^{-1}}$)
$RMSE$	root mean squared error	(-)
ρ	density	($\mathrm{kg\,m^{-3}}$)
SoC	state of charge	(-)
σ	electrical conductivity	($\mathrm{S\,m^{-1}}$)
σ	standard deviation	(-)
t	thickness	(m)
t	time	(s)
T	temperature	(°C)
T_{aging}	equivalent aging temperature	(°C)
U	voltage	(V)
U_{oc}	open circuit voltage	(V)
V	volume	($\mathrm{m^3}$)
$\dot{V}$	volume flow rate	($\mathrm{L\,min^{-1}}$)
w	width	(m)

Subscripts and superscripts

$(\cdot)_{\mathrm{air}}$	air
$(\cdot)_{\mathrm{airgap}}$	air gap
$(\cdot)_{\mathrm{av}}$	active volume
$(\cdot)_{\mathrm{avg}}$	average
$(\cdot)_{\mathrm{bag}}$	pouch bag
$(\cdot)_{\mathrm{bot}}$	bottom
$(\cdot)_{\mathrm{boundary}}$	boundary
$(\cdot)_{\mathrm{ch}}$	channel
$(\cdot)_{\mathrm{el}}$	electrical
$(\cdot)_{\mathrm{elyte}}$	electrolyte
$(\cdot)_{\mathrm{end}}$	end
$(\cdot)_{\mathrm{env}}$	environment
$(\cdot)_{\mathrm{fluid}}$	fluid

$(\cdot)_{\mathrm{i}}$	inside
$(\cdot)_{\mathrm{init}}$	initial
$(\cdot)_{\mathrm{irv}}$	irreversible
$(\cdot)_{\mathrm{max}}$	maximum
$(\cdot)_{\mathrm{min}}$	minimum
$(\cdot)_{\mathrm{n}}$	negative
$(\cdot)_{\mathrm{nom}}$	nominal
$(\cdot)_{\mathrm{o}}$	outside
$(\cdot)_{\mathrm{out}}$	outlet
$(\cdot)_{\mathrm{p}}$	positive
$(\cdot)_{\mathrm{plastic}}$	plastic
$(\cdot)_{\mathrm{plate}}$	end plate
$(\cdot)_{\mathrm{pred}}$	predicted
$(\cdot)_{\mathrm{ref}}$	reference
$(\cdot)_{\mathrm{rev}}$	reversible
$(\cdot)_{\mathrm{surf}}$	surface
$(\cdot)_{\mathrm{tab}}$	tab
$(\cdot)_{\mathrm{top}}$	top
$(\cdot)_{\mathrm{tot}}$	total
$(\cdot)_{\mathrm{trans}}$	transition
$(\cdot)_{\mathrm{true}}$	true
$(\cdot)_{-}$	negative
$(\cdot)_{\parallel}$	parallel / in-plane
$(\cdot)_{\perp}$	perpendicular / cross-plane
$(\cdot)_{+}$	positive

List of Figures

List of Tables

Bibliography

[1] E. M. Bibra *et al.*, "Global EV Outlook 2021," International Energy Agency, Tech. Rep., 2021.

[2] J. Bühler, R. Goebelt, and M. Shahd, "Mobility Studie 2020," Verband der TÜV e. V., Tech. Rep., 2020.

[3] A. Kampker *et al.*, "Battery Monitor 2023," PEM of RWTH Aachen University and Roland Berger GmbH, Tech. Rep., 2023.

[4] C. Xu, Q. Dai, L. Gaines, M. Hu, A. Tukker, and B. Steubing, "Future material demand for automotive lithium-based batteries," *Communications Materials*, vol. 1, no. 1, 2020.

[5] S. Bauer, *AkkuWelt*, 1st ed. Würzburg, Germany: Vogel Buchverlag, 2017.

[6] W. Prochazka, "Glimpses into BEV batteries on the market – AVL series battery benchmarking," Presentation at the Advanced Automotive Battery Conference Europe (AABC Europe), Mainz, Germany, 2020.

[7] Y. Zhao, L. B. Diaz, Y. Patel, T. Zhang, and G. J. Offer, "How to cool lithium ion batteries: Optimising cell design using a thermally coupled model," *Journal of The Electrochemical Society*, vol. 166, no. 13, A2849–A2859, 2019.

[8] Y. Zhao, Y. Patel, T. Zhang, and G. J. Offer, "Modeling the effects of thermal gradients induced by tab and surface cooling on lithium ion cell performance," *Journal of The Electrochemical Society*, vol. 165, no. 13, A3169–A3178, 2018.

[9] I. A. Hunt, Y. Zhao, Y. Patel, and J. Offer, "Surface cooling causes accelerated degradation compared to tab cooling for lithium-ion pouch cells," *Journal of The Electrochemical Society*, vol. 163, no. 9, A1846–A1852, 2016.

[10] S. J. Bazinski and X. Wang, "Thermal effect of cooling the cathode grid tabs of a lithium-ion pouch cell," *Journal of The Electrochemical Society*, vol. 161, no. 14, A2168–A2174, 2014.

[11] N. Ziegler. "Safety: The price for long range and high performance in electric vehicles?" (2023), [Online]. Available: https://blogs.sw.siemens.com/simcenter/battery-simulation-thermal-runaway/. Accessed: January 13, 2024.

[12] G. Damblanc. “The fast and the obvious – battery pack thermal simulation.” (2021), [Online]. Available: https://blogs.sw.siemens.com/simcenter/battery-pack-thermal-simulation/. Accessed: January 14, 2024.

[13] V. V. Ganesan and A. Jain, “Computationally-efficient thermal simulations of large Li-ion battery packs using submodeling technique,” *International Journal of Heat and Mass Transfer*, vol. 165, p. 120 616, 2021.

[14] L. H. Saw, Y. Ye, A. A. Tay, W. T. Chong, S. H. Kuan, and M. C. Yew, “Computational fluid dynamic and thermal analysis of lithium-ion battery pack with air cooling,” *Applied Energy*, vol. 177, pp. 783–792, 2016.

[15] X. Lin, M. Kerler, K. P. Birke, and M. Lienkamp, “Optimal battery cell design for electric vehicles – a holistic method with consideration of ageing due to electrothermal gradients,” in *2019 8th International Conference on Power Science and Engineering (ICPSE)*, IEEE, 2019, pp. 55–62.

[16] M. Kerler, “Eine Methode zur Bestimmung der optimalen Zellgröße für Elektrofahrzeuge,” Ph.D. dissertation, Technische Universität München, 2018.

[17] M. Kerler, F. Hoffmann, and M. Lienkamp, “Optimization through rapid meta-model based transient thermal simulation of lithium ion battery cells,” in *2017 IEEE Transportation and Electrification Conference and Expo (ITEC)*, IEEE, 2017, pp. 334–341.

[18] A. Tomaszewska *et al.*, “Lithium-ion battery fast charging: A review,” *eTransportation*, vol. 1, p. 100 011, 2019.

[19] N. Wassiliadis, J. Kriegler, K. A. Gamra, and M. Lienkamp, “Model-based health-aware fast charging to mitigate the risk of lithium plating and prolong the cycle life of lithium-ion batteries in electric vehicles,” *Journal of Power Sources*, vol. 561, p. 232 586, 2023.

[20] N. Wassiliadis *et al.*, “Quantifying the state of the art of electric powertrains in battery electric vehicles: Range, efficiency, and lifetime from component to system level of the volkswagen ID.3,” *eTransportation*, vol. 12, p. 100 167, 2022.

[21] A. König, L. Nicoletti, D. Schröder, S. Wolff, A. Waclaw, and M. Lienkamp, “An overview of parameter and cost for battery electric vehicles,” *World Electric Vehicle Journal*, vol. 12, no. 1, p. 21, 2021.

[22] A. Kampker, D. Vallée, and A. Schnettler, *Elektromobilität*. Berlin, Germany: Springer Vieweg, 2018.

[23] L. Nicoletti, A. Romano, A. König, F. Schockenhoff, and M. Lienkamp, “Parametric modeling of mass and volume effects for battery electric vehicles, with focus on the wheel components,” *World Electric Vehicle Journal*, vol. 11, no. 4, p. 63, 2020.

[24] F. Seyitoglu, K. Eren, F. Luttenberger, and P. Schiffbaenker, “Verteilte Batteriesysteme für vollelektrische schwere Lkw,” *ATZheavy duty*, vol. 13, no. 3, pp. 10–19, 2020.

[25] R. Bisschop, O. Willstrand, and M. Rosengren, "Handling lithium-ion batteries in electric vehicles: Preventing and recovering from hazardous events," *Fire Technology*, vol. 56, no. 6, pp. 2671–2694, 2020.

[26] H. Tschöke, *Die Elektrifizierung des Antriebsstrangs*. Wiesbaden, Germany: Springer Vieweg, 2015.

[27] G. Pistoia and B. Liaw, *Behaviour of Lithium-Ion Batteries in Electric Vehicles*. Cham, Switzerland: Springer International Publishing, 2018.

[28] M. Fichtner, "Recent research and progress in batteries for electric vehicles," *Batteries & Supercaps*, vol. 5, no. 2, 2022.

[29] S. Link *et al.*, "Development perspectives for lithium-ion battery cell formats," Fraunhofer Institute for Systems and Innovation Research ISI, Tech. Rep., 2022.

[30] M. Houache, C.-H. Yim, Z. Karkar, and Y. Abu-Lebdeh, "On the current and future outlook of battery chemistries for electric vehicles – mini review," *Batteries*, vol. 8, no. 7, p. 70, 2022.

[31] Y. Ding, Z. P. Cano, A. Yu, J. Lu, and Z. Chen, "Automotive Li-ion batteries: Current status and future perspectives," *Electrochemical Energy Reviews*, vol. 2, no. 1, pp. 1–28, 2019.

[32] G. Zubi, R. Dufo-López, M. Carvalho, and G. Pasaoglu, "The lithium-ion battery: State of the art and future perspectives," *Renewable and Sustainable Energy Reviews*, vol. 89, pp. 292–308, 2018.

[33] S. Link, C. Neef, and T. Wicke, "Trends in automotive battery cell design: A statistical analysis of empirical data," *Batteries*, vol. 9, no. 5, p. 261, 2023.

[34] J. Ruhland *et al.*, "Development of a parallel product-production co-design for an agile battery cell production system," in *Towards Sustainable Customization: Bridging Smart Products and Manufacturing Systems*, Cham, Switzerland: Springer International Publishing, 2022, pp. 96–104.

[35] H. Löbberding, S. Wessel, C. Offermanns, M. Kehrer, J. Rother, H. Heimes, and A. Kampker, "From cell to battery system in BEVs: Analysis of system packing efficiency and cell types," *World Electric Vehicle Journal*, vol. 11, no. 4, p. 77, 2020.

[36] N. Wassiliadis, K. A. Gamra, M. Zähringer, F. Schmid, and M. Lienkamp, "Fast charging strategy comparison of battery electric vehicles and the benefit of advanced fast charging algorithms," Poster at the Advanced Automotive Battery Conference Europe (AABC Europe), Mainz, Germany, 2022.

[37] N. Wassiliadis, J. Schneider, A. Frank, L. Wildfeuer, X. Lin, A. Jossen, and M. Lienkamp, "Review of fast charging strategies for lithium-ion battery systems and their applicability for battery electric vehicles," *Journal of Energy Storage*, vol. 44, p. 103 306, 2021.

[38] X.-G. Yang and C.-Y. Wang, “Understanding the trilemma of fast charging, energy density and cycle life of lithium-ion batteries,” *Journal of Power Sources*, vol. 402, pp. 489–498, 2018.

[39] S. Ahmed *et al.*, “Enabling fast charging – a battery technology gap assessment,” *Journal of Power Sources*, vol. 367, pp. 250–262, 2017.

[40] C. Chen, Z. Wei, and A. C. Knoll, “Charging optimization for Li-ion battery in electric vehicles: A review,” *IEEE Transactions on Transportation Electrification*, vol. 8, no. 3, pp. 3068–3089, 2022.

[41] C. Daake, M. Cammerer, and M. Hackmann, “P3 charging index: Comparison of the fast charging capability of electric vehicles,” P3 group GmbH, Tech. Rep., 2022.

[42] T. Hettesheimer *et al.*, “Lithium-ion battery roadmap – industrialization perspectives toward 2030,” Fraunhofer Institute for Systems and Innovation Research ISI, Tech. Rep., 2023.

[43] P. Makeen, H. A. Ghali, and S. Memon, “A review of various fast charging power and thermal protocols for electric vehicles represented by lithium-ion battery systems,” *Future Transportation*, vol. 2, no. 1, pp. 281–299, 2022.

[44] S. Schindler, M. Bauer, H. Cheetamun, and M. A. Danzer, “Fast charging of lithium-ion cells: Identification of aging-minimal current profiles using a design of experiment approach and a mechanistic degradation analysis,” *Journal of Energy Storage*, vol. 19, pp. 364–378, 2018.

[45] P. Keil and A. Jossen, “Charging protocols for lithium-ion batteries and their impact on cycle life – an experimental study with different 18650 high-power cells,” *Journal of Energy Storage*, vol. 6, pp. 125–141, 2016.

[46] M. Keyser *et al.*, “Enabling fast charging – battery thermal considerations,” *Journal of Power Sources*, vol. 367, pp. 228–236, 2017.

[47] T. Soczka-Guth, “Elektrifizierung von leichten und schweren Nutzfahrzeugen,” Presentation at the Conference "Advanced Battery Power", Aachen, Germany, 2023.

[48] P. Keil and A. Jossen, “Aging of lithium-ion batteries in electric vehicles: Impact of regenerative braking,” *World Electric Vehicle Journal*, vol. 7, no. 1, pp. 41–51, 2015.

[49] C. R. Birkl, M. R. Roberts, E. McTurk, P. G. Bruce, and D. A. Howey, “Degradation diagnostics for lithium ion cells,” *Journal of Power Sources*, vol. 341, pp. 373–386, 2017.

[50] Y. Preger, H. M. Barkholtz, A. Fresquez, D. L. Campbell, B. W. Juba, J. Romàn-Kustas, S. R. Ferreira, and B. Chalamala, “Degradation of commercial lithium-ion cells as a function of chemistry and cycling conditions,” *Journal of The Electrochemical Society*, vol. 167, no. 12, p. 120 532, 2020.

[51] A. S. Mussa, M. Klett, M. Behm, G. Lindbergh, and R. W. Lindström, "Fast-charging to a partial state of charge in lithium-ion batteries: A comparative ageing study," *Journal of Energy Storage*, vol. 13, pp. 325–333, 2017.

[52] L. Su, J. Zhang, C. Wang, Y. Zhang, Z. Li, Y. Song, T. Jin, and Z. Ma, "Identifying main factors of capacity fading in lithium ion cells using orthogonal design of experiments," *Applied Energy*, vol. 163, pp. 201–210, 2016.

[53] T. Waldmann, M. Wilka, M. Kasper, M. Fleischhammer, and M. Wohlfahrt-Mehrens, "Temperature dependent ageing mechanisms in lithium-ion batteries – a post-mortem study," *Journal of Power Sources*, vol. 262, pp. 129–135, 2014.

[54] M. Schindler, J. Sturm, S. Ludwig, A. Durdel, and A. Jossen, "Comprehensive analysis of the aging behavior of nickel-rich, silicon-graphite lithium-ion cells subject to varying temperature and charging profiles," *Journal of The Electrochemical Society*, vol. 168, no. 6, p. 060 522, 2021.

[55] S. Paarmann, "How non-uniform temperatures influence the performance and ageing of lithium-ion batteries," Ph.D. dissertation, Karlsruher Institut für Technologie (KIT), 2021.

[56] D. Werner, S. Paarmann, A. Wiebelt, and T. Wetzel, "Inhomogeneous temperature distribution affecting the cyclic aging of Li-ion cells. Part I: Experimental investigation," *Batteries*, vol. 6, no. 1, p. 13, 2020.

[57] D. Werner, S. Paarmann, A. Wiebelt, and T. Wetzel, "Inhomogeneous temperature distribution affecting the cyclic aging of Li-ion cells. Part II: Analysis and correlation," *Batteries*, vol. 6, no. 1, p. 12, 2020.

[58] M. Fleckenstein, O. Bohlen, and B. Bäker, "Aging effect of temperature gradients in Li-ion cells experimental and simulative investigations and the consequences on thermal battery management," *World Electric Vehicle Journal*, vol. 5, no. 2, pp. 322–333, 2012.

[59] K. S. Garud, D. Le Tai, S.-G. Hwang, N.-H. Nguyen, and M.-Y. Lee, "A review of advanced cooling strategies for battery thermal management systems in electric vehicles," *Symmetry*, vol. 15, no. 7, p. 1322, 2023.

[60] T. Nyhues, "Numerical and experimental investigation of immersion cooled battery cells and modules," Poster at the Conference "Advanced Battery Power", Aachen, Germany, 2023.

[61] P. Tirkey, R. K. Pandey, S. Kumar, and J. N. Mahto, "A detailed review on battery cooling systems for electric vehicles," in *2022 1st IEEE International Conference on Industrial Electronics: Developments & Applications (ICIDeA)*, IEEE, 2022, pp. 45–50.

[62] T. I. C. Buidin and F. Mariasiu, "Battery thermal management systems: Current status and design approach of cooling technologies," *Energies*, vol. 14, no. 16, p. 4879, 2021.

[63] D. W. Sundin and S. Sponholtz, "Thermal management of Li-ion batteries with single-phase liquid immersion cooling," *IEEE Open Journal of Vehicular Technology*, vol. 1, pp. 82–92, 2020.

[64] Z. An, L. Jia, Y. Ding, C. Dang, and X. Li, "A review on lithium-ion power battery thermal management technologies and thermal safety," *Journal of Thermal Science*, vol. 26, no. 5, pp. 391–412, 2017.

[65] I. Dincer, H. S. Hamut, and N. Javani, *Thermal Management of Electric Vehicle Battery Systems*. Chichester, West Sussex, United Kingdom: Wiley, 2017.

[66] G. Xia, L. Cao, and G. Bi, "A review on battery thermal management in electric vehicle application," *Journal of Power Sources*, vol. 367, pp. 90–105, 2017.

[67] Q. Wang, B. Jiang, B. Li, and Y. Yan, "A critical review of thermal management models and solutions of lithium-ion batteries for the development of pure electric vehicles," *Renewable and Sustainable Energy Reviews*, vol. 64, pp. 106–128, 2016.

[68] AUDI AG. "Audi e-tron 55 quattro, Liquid cooled lithium-ion battery." (2018), [Online]. Available: https://www.audi-mediacenter.com/en/photos/album/audi-e-tron-1269. Accessed: July 7, 2023.

[69] B. Mayer, M. Schier, and H. E. Friedrich, "Stand-alone battery thermal management for fast charging of electric two wheelers – integrated busbar cooling," *World Electric Vehicle Journal*, vol. 10, no. 2, p. 37, 2019.

[70] H. Heimes, A. Kampker, A. Mohsseni, F. Maltoni, and J. Biederbeck, "Cell tab cooling system for battery life extension," in *2019 18th IEEE Intersociety Conference on Thermal and Thermomechanical Phenomena in Electronic Systems (ITherm)*, IEEE, 2019, pp. 1125–1133.

[71] S. Li *et al.*, "Optimal cell tab design and cooling strategy for cylindrical lithium-ion batteries," *Journal of Power Sources*, vol. 492, p. 229 594, 2021.

[72] F. Brosa Planella *et al.*, "A continuum of physics-based lithium-ion battery models reviewed," *Progress in Energy*, vol. 4, no. 4, p. 042 003, 2022.

[73] D. A. Howey, S. A. Roberts, V. Viswanathan, A. Mistry, M. Beuse, E. Khoo, S. C. DeCaluwe, and V. Sulzer, "Free radicals: Making a case for battery modeling," *The Electrochemical Society Interface*, vol. 29, no. 4, p. 30, 2020.

[74] U. Krewer, F. Röder, E. Harinath, R. D. Braatz, B. Bedürftig, and R. Findeisen, "Review – dynamic models of Li-ion batteries for diagnosis and operation: A review and perspective," *Journal of The Electrochemical Society*, vol. 165, no. 16, A3656–A3673, 2018.

[75] A. Jokar, B. Rajabloo, M. Désilets, and M. Lacroix, "Review of simplified pseudo-two-dimensional models of lithium-ion batteries," *Journal of Power Sources*, vol. 327, pp. 44–55, 2016.

[76] V. Ramadesigan, P. W. C. Northrop, S. De, S. Santhanagopalan, R. D. Braatz, and V. R. Subramanian, "Modeling and simulation of lithium-ion batteries from a systems engineering perspective," *Journal of The Electrochemical Society*, vol. 159, no. 3, R31–R45, 2012.

[77] M. Doyle, T. F. Fuller, and J. Newman, "Modeling of galvanostatic charge and discharge of the lithium/polymer/insertion cell," *Journal of The Electrochemical Society*, vol. 140, no. 6, p. 1526, 1993.

[78] S. G. Marquis, V. Sulzer, R. Timms, C. P. Please, and S. J. Chapman, "An asymptotic derivation of a single particle model with electrolyte," *Journal of The Electrochemical Society*, vol. 166, no. 15, A3693–A3706, 2019.

[79] G.-H. Kim, K. Smith, K.-J. Lee, S. Santhanagopalan, and A. Pesaran, "Multi-domain modeling of lithium-ion batteries encompassing multi-physics in varied length scales," *Journal of The Electrochemical Society*, vol. 158, no. 8, A955, 2011.

[80] M.-K. Tran, A. DaCosta, A. Mevawalla, S. Panchal, and M. Fowler, "Comparative study of equivalent circuit models performance in four common lithium-ion batteries: LFP, NMC, LMO, NCA," *Batteries*, vol. 7, no. 3, p. 51, 2021.

[81] P. Kollmeyer, A. Hackl, and A. Emadi, "Li-ion battery model performance for automotive drive cycles with current pulse and EIS parameterization," in *2017 IEEE Transportation Electrification Conference and Expo (ITEC)*, IEEE, 2017, pp. 486–492.

[82] L. Zhang, H. Peng, Z. Ning, Z. Mu, and C. Sun, "Comparative research on RC equivalent circuit models for lithium-ion batteries of electric vehicles," *Applied Sciences*, vol. 7, no. 10, p. 1002, 2017.

[83] H. He, R. Xiong, H. Guo, and S. Li, "Comparison study on the battery models used for the energy management of batteries in electric vehicles," *Energy Conversion and Management*, vol. 64, pp. 113–121, 2012.

[84] X. Hu, S. Li, and H. Peng, "A comparative study of equivalent circuit models for Li-ion batteries," *Journal of Power Sources*, vol. 198, pp. 359–367, 2012.

[85] A. Melcher, C. Ziebert, M. Rohde, B. Lei, and H. J. Seifert, "ECM models for Li-ion batteries – a short mathematical survey and simulations," in *Jahrestagung KIT-Zentrum Energie 2016*, 2016.

[86] M. Chen and G. A. Rincon-Mora, "Accurate electrical battery model capable of predicting runtime and I–V performance," *IEEE Transactions on Energy Conversion*, vol. 21, no. 2, pp. 504–511, 2006.

[87] G. Richardson and I. Korotkin, "Heat generation and a conservation law for chemical energy in Li-ion batteries," *Electrochimica Acta*, vol. 392, p. 138 909, 2021.

[88] D. Bernardi, E. Pawlikowski, and J. Newman, "A general energy balance for battery systems," *Journal of The Electrochemical Society*, vol. 132, no. 1, pp. 5–12, 1985.

[89] R. Zhao, J. Gu, and J. Liu, "An investigation on the significance of reversible heat to the thermal behavior of lithium ion battery through simulations," *Journal of Power Sources*, vol. 266, pp. 422–432, 2014.

[90] F. Moukalled, L. Mangani, and M. Darwish, *The Finite Volume Method in Computational Fluid Dynamics*, 1st ed. Cham, Switzerland: Springer International Publishing, 2016.

[91] H. K. Versteeg and W. Malalasekera, *An Introduction to Computational Fluid Dynamics: The Finite Volume Method*, 2nd ed. Harlow, England: Pearson/Prentice Hall, 2007.

[92] J. H. Ferziger and M. Perić, *Computational Methods for Fluid Dynamics*, 3rd ed. Berlin, Germany: Springer, 2002.

[93] J. Wang, S. Lu, Y. Wang, C. Li, and K. Wang, "Effect analysis on thermal behavior enhancement of lithium–ion battery pack with different cooling structures," *Journal of Energy Storage*, vol. 32, p. 101 800, 2020.

[94] Y. Chung and M. S. Kim, "Thermal analysis and pack level design of battery thermal management system with liquid cooling for electric vehicles," *Energy Conversion and Management*, vol. 196, pp. 105–116, 2019.

[95] A. Epp, S. Rai, F. van Ginneken, A. Varchmin, J. Köhler, and D. U. Sauer, "Simulative investigation of optimal multiparameterized cooling plate topologies for different battery system configurations," *Energy Technology*, vol. 11, no. 9, 2023.

[96] A. Epp and D. U. Sauer, "Multiperspective optimization of cell and module dimensioning for different lithium–ion cell formats on geometric and generic assumptions," *Energy Technology*, vol. 10, no. 3, p. 2 100 874, 2022.

[97] A. Epp, R. Wendland, J. Behrendt, R. Gerlach, and D. U. Sauer, "Holistic battery system design optimization for electric vehicles using a multiphysically coupled lithium-ion battery design tool," *Journal of Energy Storage*, vol. 52, p. 104 854, 2022.

[98] T. Tranter *et al.*, "Liionpack: A Python package for simulating packs of batteries with PyBaMM," *Journal of Open Source Software*, vol. 7, no. 70, p. 4051, 2022.

[99] C. Reiter, "Thermische Vorauslegung hochbelasteter Batteriesysteme für Elektrofahrzeuge in der Konzeptphase," Ph.D. dissertation, Technische Universität München, 2020.

[100] C. Reiter, J. Dirnecker, and M. Lienkamp, "Efficient simulation of thermal management systems for BEV," in *2019 Fourteenth International Conference on Ecological Vehicles and Renewable Energies (EVER)*, IEEE, 2019, pp. 1–8.

[101] C. Reiter, L. Wildfeuer, N. Wassiliadis, T. Krahl, J. Dirnecker, and M. Lienkamp, "A holistic approach for simulation and evaluation of electrical and thermal loads in lithium-ion battery systems," in *2019 Fourteenth International Conference on Ecological Vehicles and Renewable Energies (EVER)*, IEEE, 2019, pp. 1–17.

[102] G. G. Wang and S. Shan, "Review of metamodeling techniques in support of engineering design optimization," *Journal of Mechanical Design*, vol. 129, no. 4, pp. 370–380, 2007.

[103] T. Ebbs-Picken, C. M. Da Silva, and C. H. Amon, "Design optimization methodologies applied to battery thermal management systems: A review," *Journal of Energy Storage*, vol. 67, p. 107 460, 2023.

[104] H. Fayaz, A. Afzal, A. D. M. Samee, M. E. M. Soudagar, N. Akram, M. A. Mujtaba, R. D. Jilte, M. T. Islam, Ü. Ağbulut, and C. A. Saleel, "Optimization of thermal and structural design in lithium-ion batteries to obtain energy efficient battery thermal management system (BTMS): A critical review," *Archives of Computational Methods in Engineering: State of the Art Reviews*, vol. 29, no. 1, pp. 129–194, 2021.

[105] A. Epp, J. C. Hahn, and D. U. Sauer, "Optimization strategy for coupled battery system design models using gaussian process regression and classification," *Journal of Energy Storage*, vol. 52, p. 104 998, 2022.

[106] X. Qian, D. Xuan, X. Zhao, and Z. Shi, "Heat dissipation optimization of lithium-ion battery pack based on neural networks," *Applied Thermal Engineering*, vol. 162, p. 114 289, 2019.

[107] M. R. Kianifar and F. Campean, "Performance evaluation of metamodelling methods for engineering problems: Towards a practitioner guide," *Structural and Multidisciplinary Optimization*, vol. 61, no. 1, pp. 159–186, 2020.

[108] B. P. Adedeji and G. Kabir, "A feedforward deep neural network for predicting the state-of-charge of lithium-ion battery in electric vehicles," *Decision Analytics Journal*, vol. 8, p. 100 255, 2023.

[109] A. Kalk, O. Birkholz, J. Zhang, C. Kupper, and M. Hiller, "Generating realistic data for developing artificial neural network based SOC estimators for electric vehicles," in *2023 IEEE Transportation Electrification Conference & Expo (ITEC)*, IEEE, 2023, pp. 1–7.

[110] S. Sharma, P. D. Achlerkar, P. Shrivastava, A. Garg, and B. K. Panigrahi, "Neural network based state of charge prediction of lithium-ion battery," in *2022 IEEE 2nd International Conference on Sustainable Energy and Future Electric Transportation (SeFeT)*, IEEE, 2022, pp. 1–6.

[111] P. Monteiro, R. E. Araujo, C. Pinto, and S. Matz, "Li-ion battery state-of-charge estimation using computationally efficient neural network models," in *2021 IEEE Vehicle Power and Propulsion Conference (VPPC)*, IEEE, 2021, pp. 1–6.

[112] D. N. T. How, M. A. Hannan, M. S. H. Lipu, K. S. M. Sahari, P. J. Ker, and K. M. Muttaqi, "State-of-charge estimation of Li-ion battery in electric vehicles: A deep neural network approach," *IEEE Transactions on Industry Applications*, vol. 56, no. 5, pp. 5565–5574, 2020.

[113] C. Vidal, P. Malysz, P. Kollmeyer, and A. Emadi, "Machine learning applied to electrified vehicle battery state of charge and state of health estimation: State-of-the-art," *IEEE Access*, vol. 8, pp. 52 796–52 814, 2020.

[114] T. Hofmann, J. Hamar, M. Rogge, C. Zoerr, S. Erhard, and J. Philipp Schmidt, "Physics-informed neural networks for state of health estimation in lithium-ion batteries," *Journal of The Electrochemical Society*, vol. 170, no. 9, p. 090 524, 2023.

[115] G. Lee, D. Kwon, and C. Lee, "A convolutional neural network model for SOH estimation of Li-ion batteries with physical interpretability," *Mechanical Systems and Signal Processing*, vol. 188, p. 110 004, 2023.

[116] D. Yang, Y. Wang, R. Pan, R. Chen, and Z. Chen, "A neural network based state-of-health estimation of lithium-ion battery in electric vehicles," *Energy Procedia*, vol. 105, pp. 2059–2064, 2017.

[117] J. C. Hamar, S. V. Erhard, A. Canesso, J. Kohlschmidt, N. Olivain, and A. Jossen, "State-of-health estimation using a neural network trained on vehicle data," *Journal of Power Sources*, vol. 512, p. 230 493, 2021.

[118] N. Khan, F. U. M. Ullah, Afnan, A. Ullah, M. Y. Lee, and S. W. Baik, "Batteries state of health estimation via efficient neural networks with multiple channel charging profiles," *IEEE Access*, vol. 9, pp. 7797–7813, 2021.

[119] S. Arora, W. Shen, and A. Kapoor, "Neural network based computational model for estimation of heat generation in LiFePO4 pouch cells of different nominal capacities," *Computers & Chemical Engineering*, vol. 101, pp. 81–94, 2017.

[120] L. Lechermann, J. Kleiner, L. Komsiyska, M. Hinterberger, and C. Endisch, "A comparative study of data-driven electro-thermal models for reconfigurable lithium-ion batteries in real-time applications," *Journal of Energy Storage*, vol. 65, p. 107 188, 2023.

[121] J. Kleiner, M. Stuckenberger, L. Komsiyska, and C. Endisch, "Advanced monitoring and prediction of the thermal state of intelligent battery cells in electric vehicles by physics-based and data-driven modeling," *Batteries*, vol. 7, no. 2, p. 31, 2021.

[122] J. Kleiner, M. Stuckenberger, L. Komsiyska, and C. Endisch, "Real-time core temperature prediction of prismatic automotive lithium-ion battery cells based on artificial neural networks," *Journal of Energy Storage*, vol. 39, p. 102 588, 2021.

[123] Y. Jiang, Y. Yu, J. Huang, W. Cai, and J. Marco, "Li-ion battery temperature estimation based on recurrent neural networks," *Science China Technological Sciences*, vol. 64, no. 6, pp. 1335–1344, 2021.

[124] L. W.-J. Juang, X. Yan, M. Sikaria, R. Zhao, P. J. Weicker, and A. Paryani, "Electric vehicle battery monitoring system," U.S. Patent 10 183 590, 2019.

[125] S. Panchal, M. Mathew, I. Dincer, M. Agelin-Chaab, R. Fraser, and M. Fowler, "Thermal and electrical performance assessments of lithium-ion battery modules for an electric vehicle under actual drive cycles," *Electric Power Systems Research*, vol. 163, pp. 18–27, 2018.

[126] K. Fang, D. Mu, S. Chen, B. Wu, and F. Wu, "A prediction model based on artificial neural network for surface temperature simulation of nickel–metal hydride battery during charging," *Journal of Power Sources*, vol. 208, pp. 378–382, 2012.

[127] U. Lämmel, *Künstliche Intelligenz: Wissensverarbeitung - Neuronale Netze*. München, Germany: Carl Hanser Verlag, 2020.

[128] I. Goodfellow, Y. Bengio, and A. Courville, *Deep Learning*. MIT Press, 2016, http://www.deeplearningbook.org.

[129] K. Murphy, *Machine Learning - A Probabilistic Perspective*. Cambridge, USA: MIT Press, 2014.

[130] S. J. Russell and P. Norvig, *Artificial Intelligence: A Modern Approach*, 3rd ed. Upper Saddle River, USA: Pearson/Prentice Hall, 2010.

[131] S. S. Haykin, *Neural Networks and Learning Machines*, 3rd ed. New York, USA: Pearson/Prentice Hall, 2009.

[132] T. M. Mitchell, *Machine Learning*. New York, USA: McGraw-Hill, 1997.

[133] B. D. Ripley, *Pattern Recognition and Neural Networks*, 1st ed. Cambridge, United Kingdom: Cambridge University Press, 1996.

[134] R. Rojas, *Neural Networks*. Berlin, Germany: Springer, 1996.

[135] C. M. Bishop, *Neural Networks for Pattern Recognition*. Oxford, United Kingdom: Oxford University Press, 1995.

[136] R. H. Myers, D. C. Montgomery, and C. M. Anderson-Cook, *Response Surface Methodology: Process and Product Optimization Using Designed Experiments*, 3rd ed. Hoboken, USA: Wiley, 2009.

[137] R. Peck, C. Olsen, and J. L. Devore, *Introduction to Statistics and Data Analysis*, 3rd ed. Belmont, USA: Thomson Brooks/Cole, 2008.

[138] E. Cramer and U. Kamps, *Grundlagen der Wahrscheinlichkeitsrechnung und Statistik*, 2nd ed. Berlin, Germany: Springer, 2008.

[139] *Datenblatt KIT_20 Lithiumionenzelle*, Battery Technology Center, Institute for Applied Materials - Energy Storage Systems, Karlsruhe Institute of Technology (KIT), 2020.

[140] A. Loges, S. Herberger, P. Seegert, and T. Wetzel, "A study on specific heat capacities of Li-ion cell components and their influence on thermal management," *Journal of Power Sources*, vol. 336, pp. 341–350, 2016.

[141] D. Werner, A. Loges, D. J. Becker, and T. Wetzel, "Thermal conductivity of Li-ion batteries and their electrode configurations – a novel combination of modelling and experimental approach," *Journal of Power Sources*, vol. 364, pp. 72–83, 2017.

[142] COMSOL AB, Stockholm, Sweden, *COMSOL Multiphysics®*, www.comsol.com.

[143] ANSYS, Inc., Canonsburg, USA, *Ansys® Fluent, Release 2023 R1*, www.ansys.com.

[144] Gamma Technologies LLC, *GT-AutoLion*, www.gtisoft.com/gt-autolion.

[145] J. Newman, "FORTRAN Programs for the Simulation of Electrochemical Systems." [Online]. Available: www.cchem.berkeley.edu/jsngrp/fortran.html, Accessed: December 4, 2023.

[146] M. Torchio, L. Magni, R. B. Gopaluni, R. D. Braatz, and D. M. Raimondo, "LIONSIMBA: A Matlab framework based on a finite volume model suitable for Li-ion battery design, simulation, and control," *Journal of The Electrochemical Society*, vol. 163, no. 7, A1192–A1205, 2016, https://github.com/lionsimbatoolbox/LIONSIMBA.

[147] R. B. Smith and M. Z. Bazant, "Multiphase porous electrode theory," *Journal of The Electrochemical Society*, vol. 164, no. 11, E3291–E3310, 2017, https://github.com/TRI-AMDD/mpet.

[148] S. Moura, "Fast Doyle-Fuller-Newman (DFN) Electrochemical-Thermal Battery Model Simulator." [Online]. Available: https://github.com/scott-moura/fastDFN, Accessed: December 4, 2023.

[149] V. Sulzer, S. G. Marquis, R. Timms, M. Robinson, and S. J. Chapman, "Python battery mathematical modelling (PyBaMM)," *Journal of Open Research Software*, vol. 9, no. 1, p. 14, 2021.

[150] R. Timms, S. G. Marquis, V. Sulzer, C. P. Please, and S. J. Chapman, "Asymptotic reduction of a lithium-ion pouch cell model," *SIAM Journal on Applied Mathematics*, vol. 81, no. 3, pp. 765–788, 2021.

[151] C.-H. Chen, F. Brosa Planella, K. O'Regan, D. Gastol, W. D. Widanage, and E. Kendrick, "Development of experimental techniques for parameterization of multi-scale lithium-ion battery models," *Journal of The Electrochemical Society*, vol. 167, no. 8, p. 080 534, 2020.

[152] P. Mohtat, S. Lee, V. Sulzer, J. B. Siegel, and A. G. Stefanopoulou, "Differential expansion and voltage model for Li-ion batteries at practical charging rates," *Journal of The Electrochemical Society*, vol. 167, no. 11, p. 110 561, 2020.

[153] K. O'Regan, F. Brosa Planella, W. D. Widanage, and E. Kendrick, "Thermal-electrochemical parameters of a high energy lithium-ion cylindrical battery," *Electrochimica Acta*, vol. 425, p. 140 700, 2022.

[154] J. Liebertseder, A. Dollinger, T. Sorg, L.-F. Berg, and J. Tübke, "Battery tab cooling in traction battery modules using thermally conductive plastics," in *2022 IEEE Vehicle Power and Propulsion Conference (VPPC)*, IEEE, 2022, pp. 1–5.

[155] *DuPont™ Kapton® MT: Polyimide Film (data sheet)*, DuPont de Nemours, Inc., 2020.

[156] *Datenblatt CMC TYP 70791*, CMC Klebetechnik GmbH, 2018.

[157] Springer-Verlag GmbH, *VDI-Wärmeatlas*, 11th ed. Berlin, Germany: Springer Vieweg, 2013.

[158] Gamma Technologies LLC, *GT-SUITE Version 2023*, www.gtisoft.com/gt-suite.

[159] F. Larsson, P. Andersson, and B.-E. Mellander, "Lithium-ion battery aspects on fires in electrified vehicles on the basis of experimental abuse tests," *Batteries*, vol. 2, no. 2, p. 9, 2016.

[160] W. Du, R. E. Owen, A. Jnawali, T. P. Neville, F. Iacoviello, Z. Zhang, S. Liatard, D. J. Brett, and P. R. Shearing, "In-situ X-ray tomographic imaging study of gas and structural evolution in a commercial Li-ion pouch cell," *Journal of Power Sources*, vol. 520, p. 230 818, 2022.

[161] H. Michael, R. E. Owen, J. B. Robinson, T. Heenan, C. Tan, A. J. Wade, R. Jervis, D. Brett, and P. R. Shearing, "Correlative electrochemical acoustic time-of-flight spectroscopy and X-ray imaging to monitor the performance of single-crystal and polycrystalline NMC811/Gr lithium-ion batteries," *Journal of Power Sources*, vol. 542, p. 231 775, 2022.

[162] G. Berckmans *et al.*, "Electrical characterization and micro X-ray computed tomography analysis of next-generation silicon alloy lithium-ion cells," *World Electric Vehicle Journal*, vol. 9, no. 3, p. 43, 2018.

[163] Martín Abadi *et al.* "TensorFlow: Large-Scale Machine Learning on Heterogeneous Systems." (2015), [Online]. Available: www.tensorflow.org. Accessed: December 4, 2023.

[164] F. Pedregosa *et al.*, "Scikit-learn: Machine learning in Python," *Journal of Machine Learning Research*, vol. 12, pp. 2825–2830, 2011.

[165] P. Virtanen *et al.*, "SciPy 1.0: Fundamental Algorithms for Scientific Computing in Python," *Nature Methods*, vol. 17, pp. 261–272, 2020.

[166] M. D. McKay, R. J. Beckman, and W. J. Conover, "A comparison of three methods for selecting values of input variables in the analysis of output from a computer code," *Technometrics*, vol. 21, no. 2, pp. 239–245, 1979.

[167] D. Hadka. "MOEA Framework - Version 2.6: A Free and Open Source Java Framework for Multiobjective Optimization." (2015), [Online]. Available: https://github.com/MOEAFramework/MOEAFramework. Accessed: December 4, 2023.

[168] K. Deb and H. Jain, “An evolutionary many-objective optimization algorithm using reference-point-based nondominated sorting approach, part I: Solving problems with box constraints,” *IEEE Transactions on Evolutionary Computation*, vol. 18, no. 4, pp. 577–601, 2014.

[169] Batemo GmbH. “LG Chem E66A.” (2023), [Online]. Available: https://www.batemo.com/products/batemo-cell-explorer/lg-chem-e66a/. Accessed: December 4, 2023.

[170] J. Liebertseder, S. Wunsch, C. Sonner, L.-F. Berg, M. Doppelbauer, and J. Tübke, “Temperature prediction of automotive battery systems under realistic driving conditions using artificial neural networks,” in *2022 IEEE 1st International Conference on Cognitive Mobility (CogMob)*, IEEE, 2022, pp. 167–172.

List of own and co-authored publications

Publications in the subject area of battery systems

Journal articles

- L.-F. Berg, **J. Liebertseder**, A. Menrath and P. Rosenberg, "Leichtbau für Schwergewichte," *Kunststoffe*, no. 5, pp. 40–43, 2022.

- C.-C. Höhne, V. Gettwert, A. Menrath, F. Frank, M. Abert and **J. Liebertseder**, "Flamm- und Brandschutz für die Elektromobilität," *AVK Composites Report*, vol. 5, no. 4, pp. 4–5, 2022.

Conference proceedings

- **J. Liebertseder**, A. Dollinger, T. Sorg, L.-F. Berg and J. Tübke, "Battery tab cooling in traction battery modules using thermally conductive plastics," in *2022 IEEE Vehicle Power and Propulsion Conference (VPPC)*, Merced, CA, USA: IEEE, 2022, pp. 1–5.

- **J. Liebertseder**, S. Wunsch, C. Sonner, L. -F. Berg, M. Doppelbauer and J. Tübke, "Temperature prediction of automotive battery systems under realistic driving conditions using artificial neural networks," in *2022 IEEE 1st International Conference on Cognitive Mobility (CogMob)*, Budapest, Hungary: IEEE, 2022, pp. 167–172.

Posters

- C.-C. Höhne, M. Abert, V. Gettwert, C. Cremers, L.-F. Berg, V. Kuchenreuther-Hummel, S. Knapp, A. Keßler, **J. Liebertseder**, A. Menrath, C. Mack, P. Müller, V. Weiser, B. Beck and M. L. Wilhelm, "Beitrag der Forschung zur Sicherheit von Einsatzkräften bei der Brandbekämpfung von Batteriesystemen," *69. Jahresfachtagung der Vereinigung zur Förderung des Deutschen Brandschutzes*, Münster, Germany, 15.–17. Mai 2023.

- **J. Liebertseder**, A. Dollinger, T. Sorg, L.-F. Berg, M. Doppelbauer and J. Tübke, "Investigation of a Battery Tab Cooling System in Traction Battery Modules," *Advanced Battery Power – Kraftwerk Batterie*, Aachen, Germany, 27.–28. April 2023.

Patents

- K. Koizumi, H. Inokuchi, A. Dekeyser, H. De Keyser, **J. Liebertseder**, L. John, "Protection plate for battery cell and resin battery module," patent submitted for filing, application no. JP 2022 212337 | PCT JP2023 045612, 2022/2023.
- K. Koizumi, H. Inokuchi, A. Dekeyser, H. De Keyser, **J. Liebertseder**, L. John, "Connector with temperature control function and resin battery module," patent submitted for filing, application no. JP 2022 212343 | PCT JP2023 045614, 2022/2023.
- K. Koizumi, H. Inokuchi, A. Dekeyser, H. De Keyser, **J. Liebertseder**, L. John, "Resin battery module," patent submitted for filing, application no. JP 2022 212354 | PCT JP2023 045615, 2022/2023.

Other subject areas

Journal articles

- S. Bucherer, **J. Liebertseder**, S. Reuter, S. Heß, L.-F. Berg and A. Zabirov, "Ganzheitliche Entwicklungsmethodik für Leichtbauansätze," *wt Werkstattstechnik online*, no. 5, 2022.
- K. Schindele, T. Sorg, T. Hentschel and **J. Liebertseder**, "Leichtbau-Nockenwellenmodul aus hochfestem faserverstärkten Kunststoff," *MTZ – Motortechnische Zeitschrift*, vol. 81, no. 9, pp. 28–34, 2020.

Conference proceedings

- A. Schröder, **J. Liebertseder** and M. Doppelbauer, "Variable speed drives in electric motors: Quantification of the energy saving potential in the EU," in *2024 13th International Conference on Energy Efficiency in Motor Driven Systems (EEMODS)*, Lucerne, Switzerland, 2024, in submission (abstract accepted).
- A. Langheck, C. Digel, **J. Liebertseder**, S. Reuter and M. Doppelbauer, "Vibration optimization in high power electric machines with lightweight plastic stator housing," in *2022 International Conference on Electrical Machines (ICEM)*, Valencia, Spain, 2022, pp. 2214–2220.
- S. Reuter, A. Langheck, **J. Liebertseder** and M. Doppelbauer, "Influence of lightweight plastic stator housing on the NVH behavior of high-performance electric machines," in *Electromechanical Drive Systems 2021; ETG Symposium*, Online, 2021, pp. 1–7.
- S. Reuter, T. Sorg, **J. Liebertseder** and M. Doppelbauer, "Design and evaluation of a houseless high-performance machine with thermoset molded internal cooling," in *2021 11th International Electric Drives Production Conference (EDPC)*, Erlangen, Germany, 2021, pp. 1–6.

Patents

- C. Laemmle, **J. Liebertseder**, A. Menrath, F. Schmidt, H. Schroth and M. Watzlawski, "Flachspulenträger," patent no. DE 10 2019 213 598 | US 20210076458 | CN 112466593, 2021.

Supervised student theses

In the subject area of battery systems

- P. Benz, "Concept analysis of a bidirectional, autonomously partitionable battery system for the electromobility and the optimized usage of renewable energies," *Bachelor's Thesis*, 2022
- L. Sollik, "Investigation of the optimal battery cell design for an efficient cell cooling," *Master's Thesis*, 2021
- S. Wunsch, "AI-based simulation models for the efficient modeling of the electrochemical-thermal behavior of battery cells," *Master's Thesis*, 2021
- J. Ulrich, "Development of a model for performant electrothermal simulation of tab cooled lithium-ion battery cells for the evaluation of the thermal management of traction batteries," *Master's Thesis*, 2021
- A. Royet, "Analysis and optimization of a novel cooling system for battery systems by numerical simulation," *Master's Thesis*, 2020
- A. Ardaillou, "Design, layout and optimization of a lightweight battery system based on structural composites," *Master's Thesis*, 2020
- T. H. Cao, "Development of an electric vehicle battery housing and battery module made of fiber-reinforced composites," *Master's Thesis*, 2019

Other subject areas

- A. Schröder, "Vibration investigation and derivation of the bearing loads of the propulsion system of a heavy-duty drone using multibody and structural simulations," *Master's Thesis*, 2022
- M. N. M. Salim, "Validierung von verbrennungsmotorischen CFD-Simulationen am Heißgasprüfstand," *Semester Thesis*, 2019

Fast simulation models that predict the temperature difference in a battery cell depending on the geometric cell design are needed for the evaluation, comparison and thermal optimization of battery modules with tab cooling and other cooling approaches.

Here, a new simulation model based on a neural network is proposed which rapidly predicts the maximum temperature difference in a single battery pouch cell after a charging process. The model considers all relevant geometric and thermal parameters. Using this model, a charging process of a battery module can be computed in less than 18 s. This enables the thermal optimization of pouch cell designs and the comparison of different cooling approaches on module level, which is demonstrated on two exemplary test cases.

Furthermore, a tab-cooled battery module prototype using thermally conductive plastic materials is developed and analyzed. The simulation model is partly validated with the prototype and its cooling performance is evaluated on a test bench.

ISBN 978-3-8396-2025-0

Fraunhofer VERLAG